MODELING AND SIMULATION OF ELECTROCHEMICAL DNA BIOSENSORS IN CMOS TECHNOLOGY

MODELING AND SIMULATION OF ELECTROCHEMICAL DNA BIOSENSORS IN CMOS TECHNOLOGY

By

M. Waleed Shinwari

Bachelor of Science

King Fahd University of Petroleum and Minerals

June 2003

A THESIS

SUBMITTED TO THE SCHOOL OF GRADUATE STUDIES IN PARTIAL FULFILLMENT OF THE REQUIREMENTS FOR THE DEGREE OF

MASTER OF APPLIED SCIENCE

McMaster University

Hamilton, Ontario, Canada

MASTER OF APPLIED SCIENCE (2007) McMaster University
(Electrical and Computer Engineering) Hamilton, Ontario

TITLE: Modeling and Simulation of Electrochemical DNA Biosensors in CMOS Technology

AUTHOR: M. Waleed Shinwari, B. Sc. (King Fahd University of Petroleum and Minerals)

SUPERVISOR: Prof. M. Jamal Deen

NUMBER OF PAGES: xv, 158

Abstract

Early detection of pathogens in food and water samples is essential in containing and preventing the spread of various diseases, such as campylobacter jejuni or E-coli. In the food processing industry, fast and reliable methods for testing products against contamination would mean faster delivery and better food quality. The pairing specificity of complementary DNA strands provides a highly selective means of detecting pathogens based on their genomic content. Recently, a lot of research has been directed towards the use of mainstream semiconductor technology to build highly sensitive and cheap DNA hybridization sensors. Typically, the gate of a metal-oxide-semiconductor (MOS) transistor is removed, and probe single-stranded DNA molecules are added to the exposed insulator. Complementary DNA hybridization from a solution sample can then be sensed electrostatically by the underlying Field-Effect transistor (FET).

The work in this thesis is concerned with the mathematical modeling of FET-based biosensors, named BioFETs. Modeling will enable the assessment of the sensitivity of such devices, as well as the potential for using the BioFETs in creating fully electronic microarrays. The mathematical model presented here captures the effects of ionic charge screening of the DNA charges by counterions in the ambient solution, and the effects of surface adsorption that can also aid in the charge screening process. The effects of varying different parameters on the sensitivity of the BioFET are investigated, and the noise contributed by the FET structure is incorporated into the analysis to quantify the expected signal-to-noise ratio (SNR) of the BioFET.

In order to gain further insight into the operation of the BioFET, linear approximations are applied to the different regions of the BioFET to arrive at an analytic expression that approximates its expected response to DNA hybridization. The approximations are verified by comparing them against the results obtained from the physical model. Finally, different circuit configurations are presented that allow for highly sensitive biosensors to be realized using the BioFET, and a description of a fabricated electronic DNA microarray chip in standard CMOS 0.8 μm is presented.

In the Name of God, Most Merciful, Most Compassionate

Acknowledgments

This section is intended to acknowledge all kinds of support that I have received throughout the process of conducting this research and preparing this thesis. The names are numerous, and a few lines of recognition do not do justice to the amount of help, support and encouragement that I have received, and continue to receive, from these people.

Firstly, I would like to thank my supervisor, Prof. M. Jamal Deen, for trusting me with this work and giving me the opportunity to be involved in such a sophisticated and interesting topic of research. I would like to thank him for proposing many of the ideas presented here, which I was able to study in depth. Prof. Deen has been nothing short of a great mentor to me, offering his guidance throughout the intricacies of this research. The amount of energy and devotion he allocates for his work never ceases to amaze me, and he continues to set an example in organization, professionalism, and scholarly prowess that is very hard to follow.

Next, I would like to thank Dr. Dolf Landheer, for helping me with my research, and clearing up a lot of confusions that I had.

I would also like to thank Prof. Ravi Selvaganapathy and Prof. Xun Li, for taking the time in reading, commenting, and providing feedback on this work. I would like to thank them for taking part in the evaluation of this work and for being in my defense committee.

Many thanks are due to all the members of our microelectronics lab. I start with Mr. Munir El-Desouki, who is a dear friend and an extremely helpful colleague. Without his continued encouragement, this work would not have gotten off the floor. I would also like to thank Dr. Ognian Marinov for his keenness in getting involved with my work and offering valuable help and support. Many thanks are due to all the members of the microelectronics research laboratory. I would especially like to thank: Moussa Kfouri, Hamed Mazhab-Jafari, Ali Abu-el-Magd, Ahmad Fakhr, Samer Rizk, Samar Abdelsayed, and Farseem Mohammedy, for being such a great team to work with.

At this point, I would like to thank all my professors in King Fahd University of Petroleum and Minerals, Dahran, Saudi Arabia. I especially would like to thank Prof. Mohammad Taher AbuelMa'atti, Prof. Alaeddin Amin, Prof. Nawar Tabet, and Prof. Mohammad Musazay, for being such great mentors, offering help and support whenever I needed it. Your guidance is forever remembered.

Next, I would like to thank all my friends for their help, encouragement, and support. Specifically, I would like to thank Ismail Alani, Hisham Al-Rowaihy, Jessica Duckworth, Adib Ternawly, Ismail Ternawly, and Yara Al-Sheikh, for being such amazing friends.

Finally, I would like to thank all the members of my family: My father, Prof. M. Anwar Shinwari, my mother, Kamila, my sisters: Neptune, Mahira, Zakiya, Jameela, Zarghuna, and Tasneem, and my brothers: Daoud, Fareed, Merwaise, and Noor Ahmad. You have always been there for me, and I am forever in your debt.

Table of Contents

List of Figures

List of Tables

Chapter 1

INTRODUCTION

1.1 Microfabricated Biosensors

A biosensor can be broadly defined as a device containing two interacting phases, one which responds to a certain biological substance or process, and another which transduces this response into a measurable physical quantity, often electric [1-5]. This definition communicates different means of classifying such devices. One might therefore categorize biosensors into biochemical and bio-process sensors, or into electrical, mechanical, piezoelectric and optical sensors [9], [11], [12]. The ability of biochemical sensors to detect biologically relevant molecules distinguishes it from chemical sensors, which sense ions, compounds and polymers that need not be linked to any form of life [9]. Examples of such chemical sensors are those used for the detection of pH concentrations in fluids, or of certain free radical contaminants in the air or water. Biological sensors, on the other hand, are sensitive to substances such as DNA, proteins, lipids, or biological disturbances such as neuronal action potentials [11], or characteristic electrokinetic signatures of motion in cells and microorganisms [16].

During the past few decades, a lot of research has targeted the design of biosensors. This rapid progress can be partly attributed to the success of the Human Genome Project (1990-2003), which helped in devising state-of-the-art techniques in microbiology, gene expression analysis and molecular diagnostics [5]. Another factor was the incorporation of the semiconductor industry's technology, which ultimately led to extremely high levels of control over microfabrication techniques and processes, to help design better characterized biosensors. Yet another factor was the evolution of the MEMS (micro-electromechanical systems) industry as a natural result of the success of

the semiconductor microfabrication industry [12]. Since sensors occupied a large market segment for the miniaturization technologies in the past decade [17], it is not surprising that biosensors would adopt the philosophy of miniaturization, just as the microelectronics and MEMS industries have, and rapidly develop and become much more technologically advanced than it has been in the previous years. Figure 1.1 shows the projected market size of microarray biosensors between years 1999 and 2008, as well as a pie chart showing the contributions of different areas of molecular diagnostics [11]. As shown, the biosensors market is expected to rise, with the main areas of development being molecular diagnostics and life science research. In addition, most of the research in molecular diagnostics is directed towards microarray sensor development.

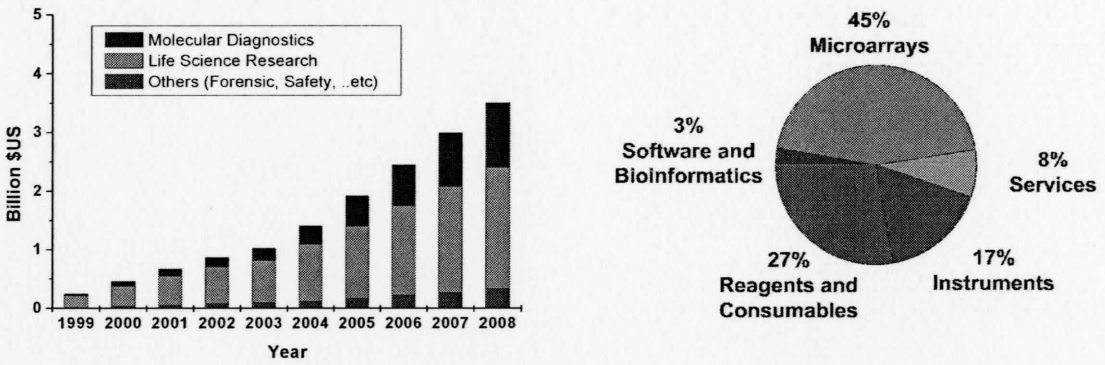

Figure 1.1 Worldwide predicted biosensors market size [11]

The question to be asked here is: why miniaturize? Just as miniaturization helps increase the speed of electronic and MEMS devices, allows more integration and reduced cost of fabrication, and provides means for high-precision device synthesis, biosensors benefit from miniaturization as well. Micro-fabricated biosensors would allow extremely small and dilute analyte samples to be detected, due to the smaller bio-active area that must be stimulated. This might eventually eliminate the need for pre-processing samples before introducing them to the biochemical sensor. Batch fabrication techniques, borrowed from the microelectronics industry, would result in a dramatic reduction in the cost per sensor, facilitating economically feasible access to highly dense biosensor arrays [5]. Power consumption would be low, a trait that lends itself greatly to portability of the

biosensor. The accuracy and repeatability of a biological experiment, which has always posed a hindrance in the development of biosensors [1], [3], [4], [5], [9], [12], [15], would be enhanced. Combined with biocompatible membranes and communication electronics, a microfabricated biosensor would allow for in-vivo sensing and controlled, localized drug delivery [6]. Finally, integration with MEMS and microelectronics would make it possible to realize a miniaturized reaction, processing, and sensing biosystem, also known as a lab-on-a-chip, or a micro-total analysis system (μTAS) [12].

Despite the many advantages of minimization, it is not free of problems. First, since essentially all measured physical signals are in fact statistically averaged quantities of the micro-signals at small scales, miniaturization would limit this averaging functionality and divulge the discreteness and variability in these signals, yielding a higher degree of fluctuation and a lower SNR (signal-to-noise ratio) [12]. Excessive miniaturization would also expose secondary effects that are often hard to model, such as complex geometries of sensed biomolecules, 2D and 3D electromagnetic effects, and non-uniform scaling of forces that might lead to rather peculiar mechanical and thermodynamic behavior at the molecular level. Finally, scaling to the nano-level can expose quantum-mechanical effects that can severely affect the performance of the sensor.

Successful integration of the chemical medium in biosensors with the semiconductor industry has enabled sensing of many different biological processes, including biological cellular activities [2]. Using silicon, as opposed to glass or plastic-based slides, can allow for the seamless integration of biological and semiconductor domains. Since the chemistries of these two phases are rather different, essential understanding of processes that take place when these phases come into contact is of great importance. Proper modeling of a biosensor would allow us to predict sensitivity, detection limits, and scaling effects of the biosensor. Using physics-based model equations to describe the operation of the biosensor can also allow for optimization techniques to maximize certain aspects of the biosensor, such as SNR.

1.2 Early Detection of Pathogens

Biosensors can be used very efficiently to detect the presence of pathogens in biological samples [18], [19]. Pathogens account for around 40% of the world's annual mortality count, which isestimated at 50 million [19]. They are also responsible for most of the world's major outbreaks. Table 1.1 summarizes some of the different pathogens and their corresponding diseases [19]. Pathogens differ in their nature and can be bacterial, viral, protozoa, or even proteins. Using biosensors to detect the presence of such pathogens requires a specific trait of the pathogen to be identified. The biosensor could detect a result of a metabolic reaction of the pathogen sought, or it could detect a specific behavior of the pathogen or one of its specific constituents. An example is the specific reactions of the pathogens' protein structures, or the specific binding of antigens and antibodies, which is the main principle in immunoassay-based biosensors [20].

Table 1.1 Several bacterial pathogens, their corresponding diseases and toxins released [19]

Pathogen	Disease	Toxin secreted
Bacillus anthracis	Anthrax	Edema factor
Brucella melitensis	Brucellosis	-
Campylobacter jejuni	Diarrhea dysentery	-
Clostridium botulinum	Botulism	Neurotoxin
Coxiella burnetti	Pneumonia	-
Corynebacterium diphtheriae	Diphtheria	Diphtheria toxin
Escherichia coli	Gastroenteritis	Enterotoxin
Francisella (Pasteurella) tularensis	Tularemia	-
Mycobacterium tuberculosis	Tuberculosis	-
Rickettsia rickettsi	Rocky Mountain-spotted fever	-
Salmonella paratyphi	Paratyphoid	-
Salmonella typhi	Typhoid fever	-
Shigella dysenteriae	Bacillary dysentery	Neurotoxin
Staphylococcus aureus	Pneumonia	Enterotoxin
Staphylococcus pneumoniae	Pneumococcal pneumoni	Erythrogenic toxin
Treponema pallidum	Syphilis	-
Vibro cholerae	Cholera	Enterotoxin
Yersinia pestis	Bubonic plague	Plague toxin

When pathogens attack a host organism, they manifest in the fluids of the host. The concentrations of the pathogens are generally too low to be detected efficiently [20]. Therefore, an initial step in conventional food monitoring is to prepare a sample solution for detection by pre-enrichment of the raw sample to maintain a healthy bacterial population. This is succeeded by a selective enrichment, in which only the pathogen to be detected is allowed to grow, while other possible measurement contaminants are inhibited [4], [5], [20]. Once a pure, dense sample of the pathogen is available, the metabolism of this culture can be monitored and the disease can be identified with the aid of biochemical identification techniques. Figure 1.2 illustrates the conventional steps of pathogen detection [20]. Unfortunately, this process is time-consuming, requiring days of incubation [19], [20]. Also, professional expertise is required in conducting the experiments and providing results. It would, therefore, be desired to have a method of rapid, early detection of pathogens in food and water such that the initial time consuming periods of enrichment are not needed. Biosensors that are based on the detection of specific characteristics of biological molecules of certain microorganisms provide the means for early and rapid pathogen detection. This would, in turn, allow faster containment of an otherwise spreading epidemic.

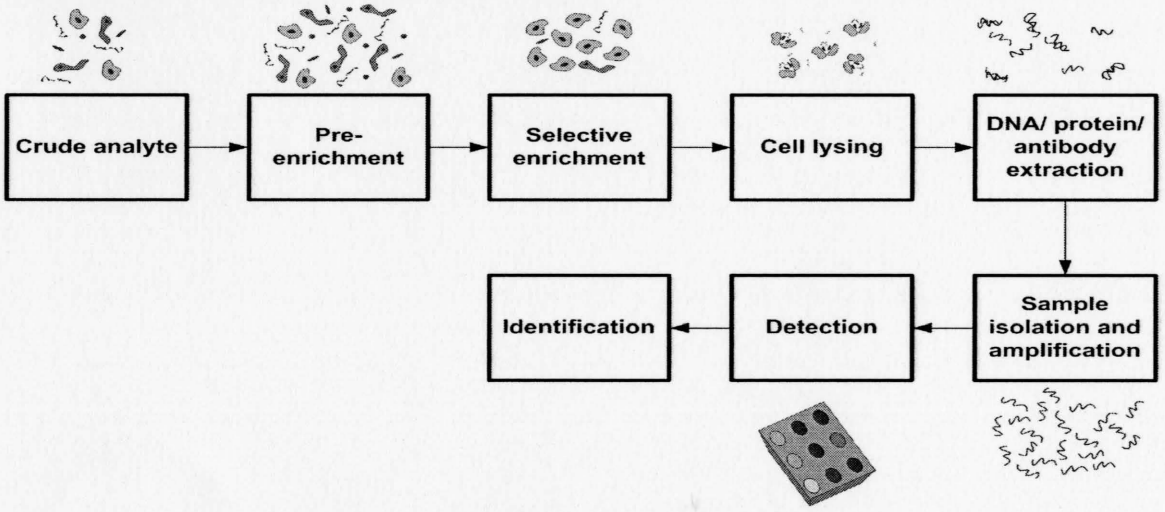

Figure 1.2 Pathogen detection steps [4], [5], [20]

One of the most widely used techniques in pathogen detection and microbiological diagnosis is gene expression analysis using deoxyribonucleic acid (DNA)

hybridization. This technique has been shown to have higher stability than that of immunoassays [19], due to the higher stability of the chemical phenomena leading to the hybridization. In order to fully understand DNA hybridization and hybridization sensors, it is essential that the basic chemical structure of the DNA be understood. Figure 1.3 shows the chemical structure of a segment of a DNA molecule. The DNA molecule is a biopolymer consisting of a double helix backbone, each consisting of alternating deoxyribose sugar and phosphate groups, linked by phosphodiester bonds. In addition, each sugar ring contains a link to a nitrogen base [3]. There are two possible families of nitrogen bases: purines and pyrimidines. In the DNA of almost all organisms, four different types of bases are found, two purines (adenine and guanine), and two pyrimidines (cytosine and thymine). The structures of these four bases are such that adenine and thymine, in their quiescent locations on opposite DNA strands, align so that it is energetically favorable to create two hydrogen bonds between them, as shown in Figure 1.4. Similarly, oppositely placed cytosine and guanine bases will create three hydrogen bonds, reducing the overall energy of the system.

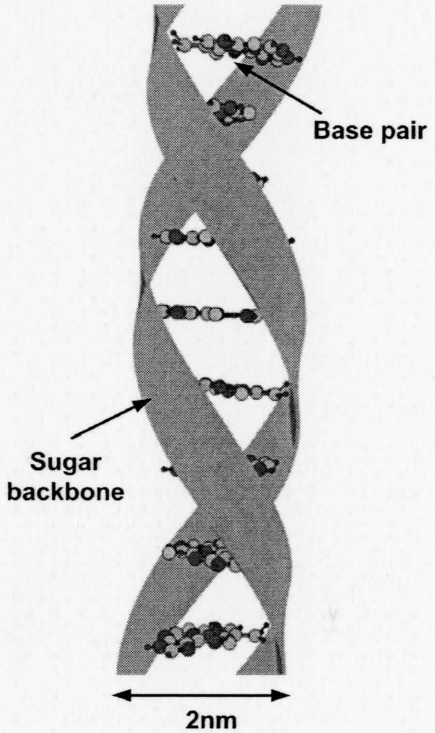

Figure 1.3 Molecular structure of DNA

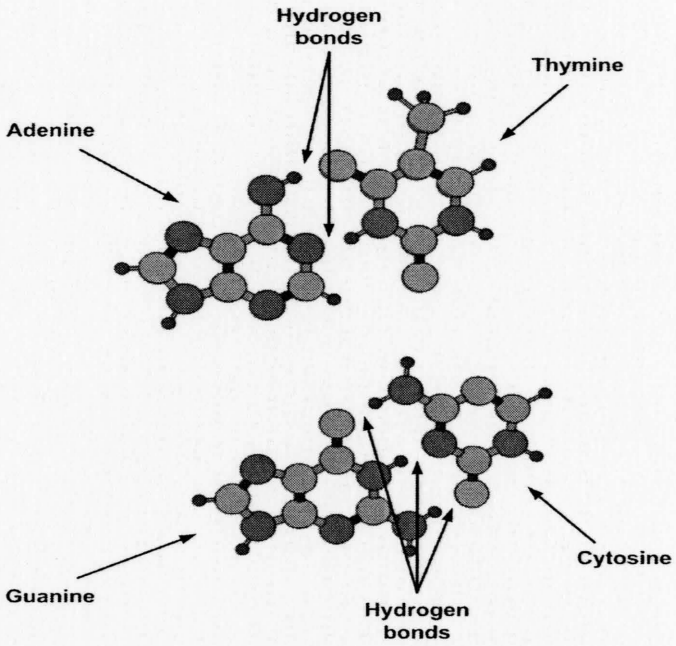

Figure 1.4 Base pairing in DNA

It is important to note that the phosphate groups that link the sugar backbones together are missing a third bond, and therefore have an excess negative charge. This makes the DNA backbone negatively charged. As such, it would be expected that placing any two single strands of DNA polymers in the vicinity of each other will cause them to electrostatically repel each other. While this is true in general, if the two strands contain exactly the complementary sets of base pairs in the exact same locations, such that each base would favorably create hydrogen bonds with the opposite base in the other strand (i.e. A with T, and C with G), then at steady state, the two DNA strands will coalesce, in spite of the repelling electrostatic negative charge. This is an outstanding result that defies the expected behavior of simple ions and shows how chemical reactions can overcome electrostatic interactions. The resulting stable DNA molecule would be 2 nm in diameter, with a 0.34 nm vertical pitch between adjacent base pairs, and around 10 base pairs per full cycle of the double helix [13].

What is important to note is that unless the two strands are completely complementary in base pairs, this process of DNA attachment (hybridization or pairing) would not be thermodynamically favorable. Although this might still happen, particularly

for long DNA strands, shorter hybridized strands that are not fully complementary will not be very stable, and will tend to split (denature). Denaturation can also be induced by applying enough amount of heat to thermally overcome the energy reduction of forming the hydrogen bonds. It has been shown [8] that the higher the G-C content of a DNA molecule, the higher the temperature of denaturation will be, owing to the extra hydrogen bond that must be broken in each base pair. Figure 1.5 shows this dependence for the DNA of several microorganisms [8].

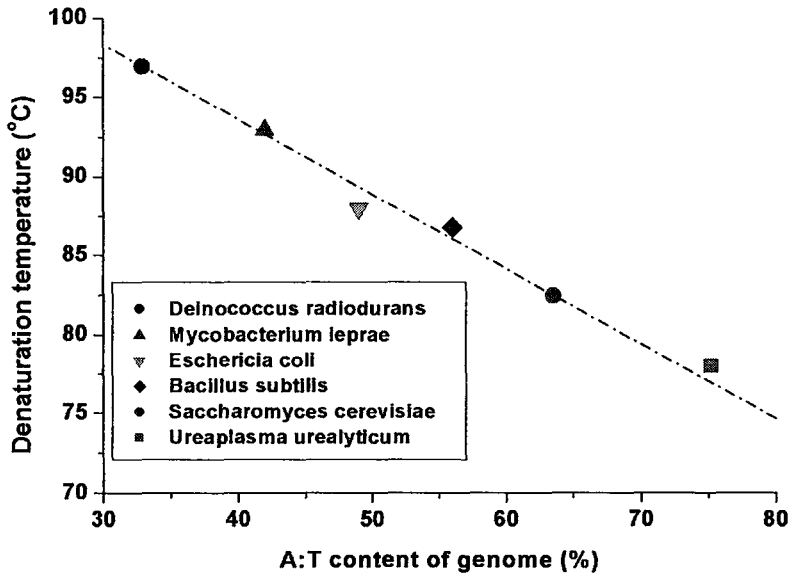

Figure 1.5 Effect of DNA base content on denaturation temperature [8]

The specific pairing of a single-stranded DNA (ssDNA or oligonucleotide) to its complement has been utilized to design very efficient biosensors, based on the specificity of hybridization. Each living organism contains paired DNA molecules bundled into chromosomes in the nuclei of its cells. These DNA strands can be extremely long (about 6 billion base pairs in humans). What is important is the sequence of base pairs within the DNA strands. Certain segments of these sequences define "coding genes" that specify certain traits or characteristics of the organism. These coding genes are responsible for directing the synthesis of proteins during cell division. Thus, the DNA is the means by which hereditary information is maintained and passed on in any living organism. Since

the collection of genes in a particular organism has all the information about the structure and function of that organism, these genes can be used to uniquely identify them, pathogens included. This is the basic idea behind using DNA hybridization biosensors for pathogen identification. If successful hybridization of an unknown ssDNA strand to a known one can be detected, then one can speculate, with an extremely high degree of confidence, that the complementary sequence exists in the first ssDNA. If many such experiments are conducted for different sequences, the collection of which uniquely identify a specific pathogen, then successful hybridization in all these experiments would be enough to conclude the existence of the pathogen in the sample [1], [4], [21].

In order to facilitate rapid and early detection of pathogens, it is important to be able to detect as minimum a concentration of pathogens as possible, thereby eliminating the need for lengthy and time-consuming enrichment and refinement cycles. Thus, a major criteria in the design of biosensors is sensitivity [19], defined for DNA sensors as the minimum detectable concentration of ssDNA molecules in a solution. Other factors include selectivity, which can be defined as the ratio of the sensor's output signal due to intended species to that due to foreign reactions. A highly selective sensor might provide reliable results even with a contaminated sample. This property would eliminate the need for purification and selective enrichment of the sample analyte [3]. In DNA hybridization sensors, selectivity against non-complementary DNA is achieved to a high degree by the thermodynamics of the hybridization reaction, whereas selectivity against binding of malicious proteins or other structures is not guaranteed. Other required performance parameters of biosensors include [2], [3], [19]:

- Reaction settling time: The amount of time the sensor needs to reach steady state.
- Signal-to-noise ratio (SNR): The ratio between the signal power and the noise power.
- Size
- Power consumption
- Portability

- Tolerance: The amount of variation in different parameters that will not affect the operation of the sensor.
- Integrability with mainstream electronics
- Drift: The shift in the reading value for the biosensor with aging.
- Operational expertise.

1.3 Contemporary Methods of DNA Hybridization Detection

This section provides a survey of different methods that have been explored for DNA hybridization detection. Broadly, these can be categorized into labeled and label-free methods, depending on whether a radioactive, chemiluminescent, or fluorescent agent is needed for the sensing mechanism.

1.3.1 Labeled Methods

One of the oldest techniques for sequencing DNA strands and hybridization detection is known as the Southern blot. This method was introduced by E. Southern in 1975 [22] and has been since then used extensively in DNA sequencing and gene expression analysis. Depicted in Figure 1.6, the initial unknown DNA (called the targets) are broken into smaller pieces and separated based on size using gel electrophoresis, which separates the fragments due to their differing mobilities within the gel. After the separation is complete, further treatment using a basic medium causes the DNA to denature. Then, a nylon (or equivalent) sheet is pressed against the gel, causing the DNA to stick to the membrane. Ultraviolet treatment of this sheet causes the DNA to become permanently attached. Now, the known DNA strands (called the probes) are labeled with a radioactive or fluorescent dye and introduced to the targets. If hybridization occurs, the radioactive labels will remain on the sheet after it is washed and will show under an x-ray lamp [22]. Other dyes such as chemiluminescent, fluorescent, or chromogenic would require different methods of detection, including laser absorption and chemical treatment. Radioactive dyes have the advantages of exhibiting higher sensitivities, but they also

prohibit parallel gene analysis, and pose higher health risks for long exposure times [14], [20].

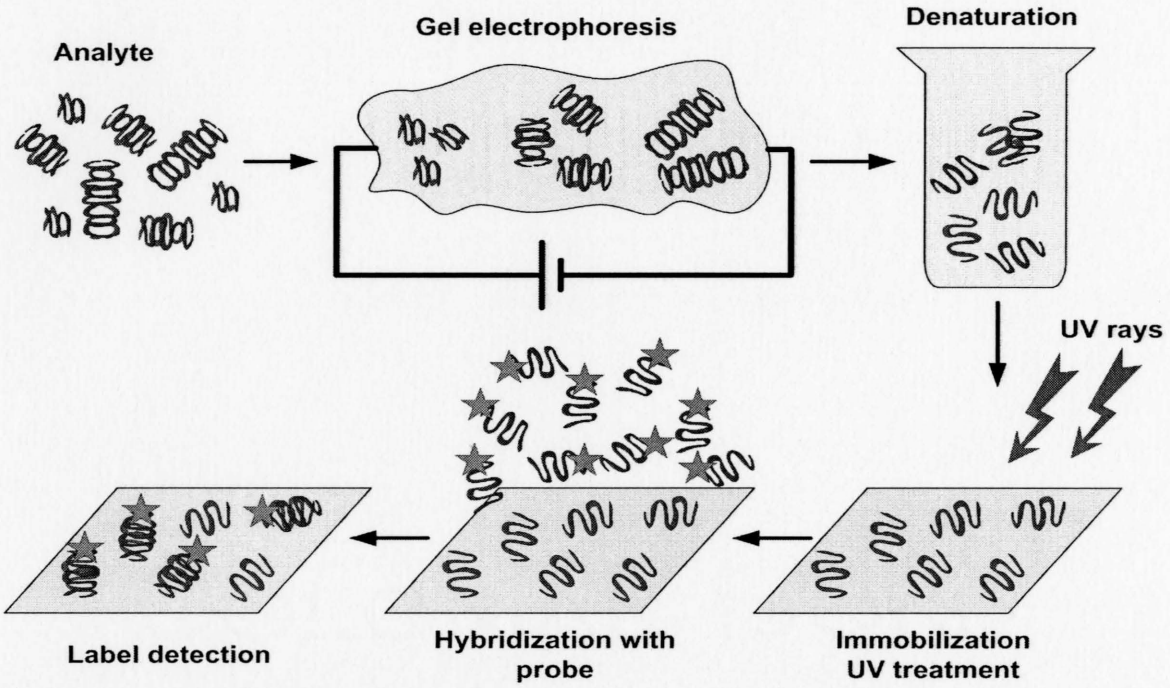

Figure 1.6 Steps for DNA detection using the Southern blot technique

Another labeled method that has been used for DNA detection is the polymerase chain reaction (PCR). This method is illustrated in Figure 1.7 [3]. Initially, a target DNA is heated up to its denaturing temperature (typically 70-95°C, as given in Figure 1.5) [20]. Then, a DNA primer, which is a synthesized molecule that binds to a very short, known segment of the DNA, is introduced into a solution containing an abundance of the needed compounds to create the DNA backbone and the internal base pairs. The primer gets attached to the appropriate part of the target ssDNA, and an enzyme called the DNA polymerase allows the primer to grow, replicating the complementary strand of the ssDNA, using the initial ssDNA as a template [20]. Heating the result causes the newly formed DNA to denature, allowing a second PCR cycle to be initiated. Thus, PCR can cause exponential amplification of the nucleic acid. This can allow for detection limits as low as a single molecule, given enough cycles of PCR. However, after PCR is done, a labeling technique similar to the Southern blot must be incorporated to identify the resulting DNA. Thus, DNA detection using PCR, although highly sensitive, requires a

very long time to execute. In addition, the sample that is introduced to the PCR chamber must be highly purified, since it has been shown that some particular food substances can retard the progress of the chain reaction [20].

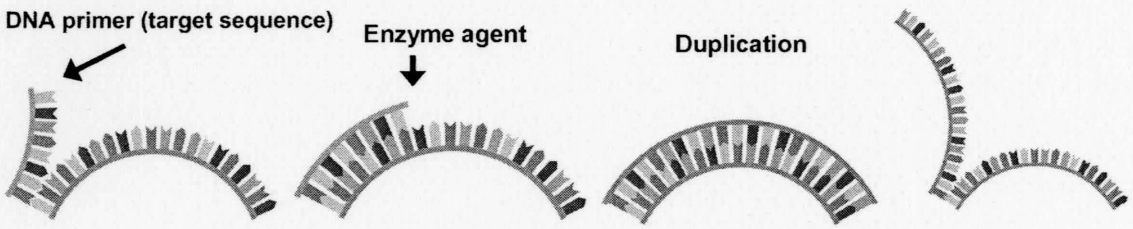

Figure 1.7 Illustration of the PCR replication process [3]

The most recent technique of mainstream DNA hybridization detection is the use of DNA microarrays. DNA microarrays are miniaturized hybridization chambers that can be made of glass, silicon, or plastic. The density of these arrays varies and can reach values of 10^6 chambers in 1 cm^2 of glass or silicon [1]. Each one of these chambers contains ssDNA molecules of known base sequence immobilized on the bottom. The DNA probes do not generally exhaust all the permutations of the base sequences but are carefully chosen based on the known signatures of the pathogens' DNA to be detected [4]. These probe ssDNA fragments can be either spotted on the microarray cells with the aid of precision robot arms, immobilized using surface adsorption or self-assembled monolayers (SAMs), or directly synthesized on the chip while the microarray is being fabricated. This type of in-situ synthesis can be done using photolithographic techniques (such as the one used by Affymetrix), or using ink-jet methods (Agilent Technologies) [4].

Once the microarray has been fabricated and probes immobilized, the sensor is ready for hybridization experiments. The procedure for conducting the experiment is illustrated in Figure 1.8. Typically, target DNA molecules are acquired from samples after passing through many steps of preparation, purification and amplification. These include cell lysing, DNA separation by gel electrophoresis, and amplification by PCR. The next step is to label the target ssDNA with fluorescent labels. The targets are then introduced into the microarray and allowed to hybridize. The entire microarray is then washed to flush away any DNA molecules that have not hybridized to a microarray cell. The microarray

is scanned using a laser scanner and the intensity of light emitted from the cells would be an indication of the density of targets that have successfully hybridized, illustrating the availability of that base sequence in the target DNA. The image signature of the microarray can be read into a computer, and several signal and image processing techniques can be utilized to determine, with a high degree of specificity, the nature of the microorganism to which the target DNA fragments belong [1], [4]. Figure 1.9 shows an example of the image constructed by a microarray experiment [29]. Such an image can contain information pertaining to many different pathogens. As such, microarrays can be used to simultaneously detect many different pathogens, without the need to conduct separate experiments [7].

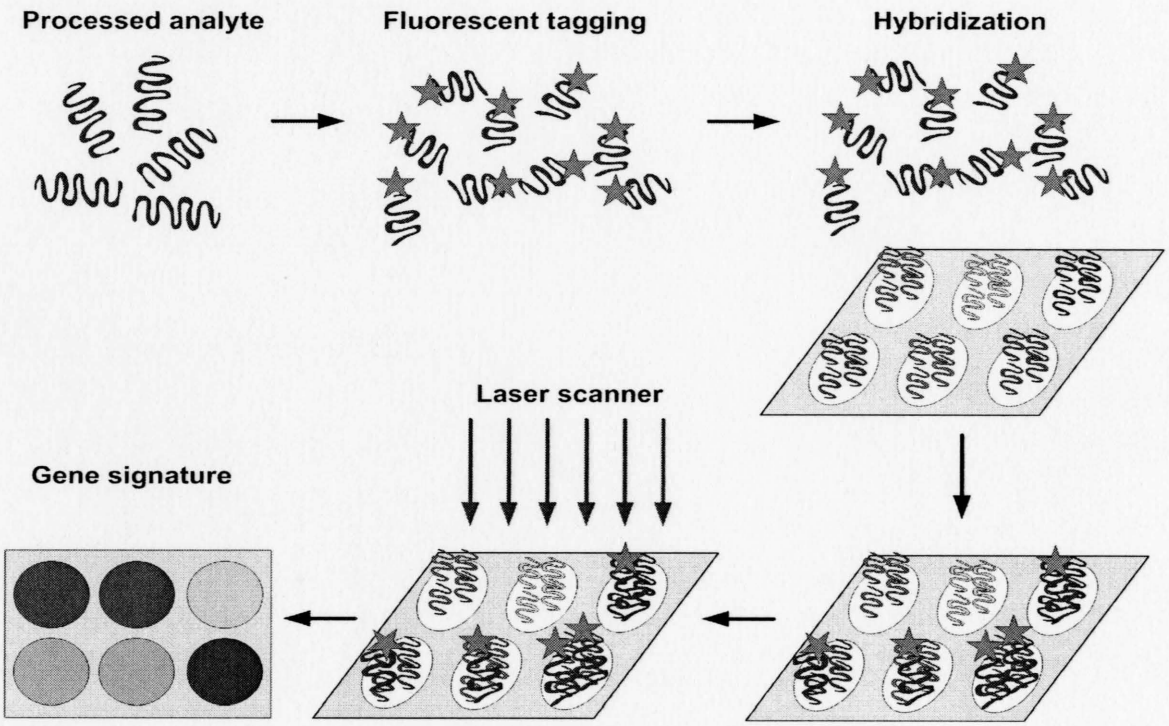

Figure 1.8 DNA microarray technique

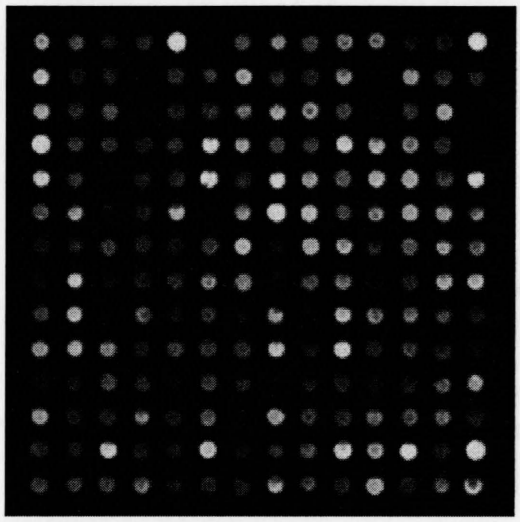

Figure 1.9 Sample DNA microarray image [29]

1.3.2 Label-free Methods

Labeled methods of DNA detection have great advantages in terms of sensitivity and robustness [15]. However, they require the use of labeling agents, which can be quite costly. Also, using fluorescent labels requires a high-precision microarray scanner. These are implemented with laser beams and are very expensive. These requirements limit the technology of DNA microarrays to relatively wealthy laboratories and pose problems in the quest to realize miniature, handheld microarray analyzer devices. As a result, a lot of research has been devoted to develop new techniques that enable sensing DNA hybridization without the need to resort to labeling methods. This section briefly describes some of these techniques.

Most label-free methods are based on electrochemical characteristics that can be modulated by the presence of hybridized DNA. One of these methods is AC impedance spectroscopy [9], [10]. In an electrochemical cell, if the probe DNA is immobilized on an electrode, hybridization of the target would cause impedance changes to this interface. Some reports attribute this change to the conductive properties of the DNA [10], while others relate it to the effects the DNA molecules have on the interfacial capacitance (more on this in chapter 2) [23]. Impedance change, whether resistive, capacitive or inductive, can alter the operation of sensitive frequency-dependent circuits and can be

used for DNA hybridization detection. A variation of this technique uses silicon as the immobilization electrode [24]. Results show that using such sensors can be quite efficient and can achieve highly sensitive label-free detection. Figure 1.10 shows the setup used in [24] for measuring the impedance change of a DNA-modified silicon electrode.

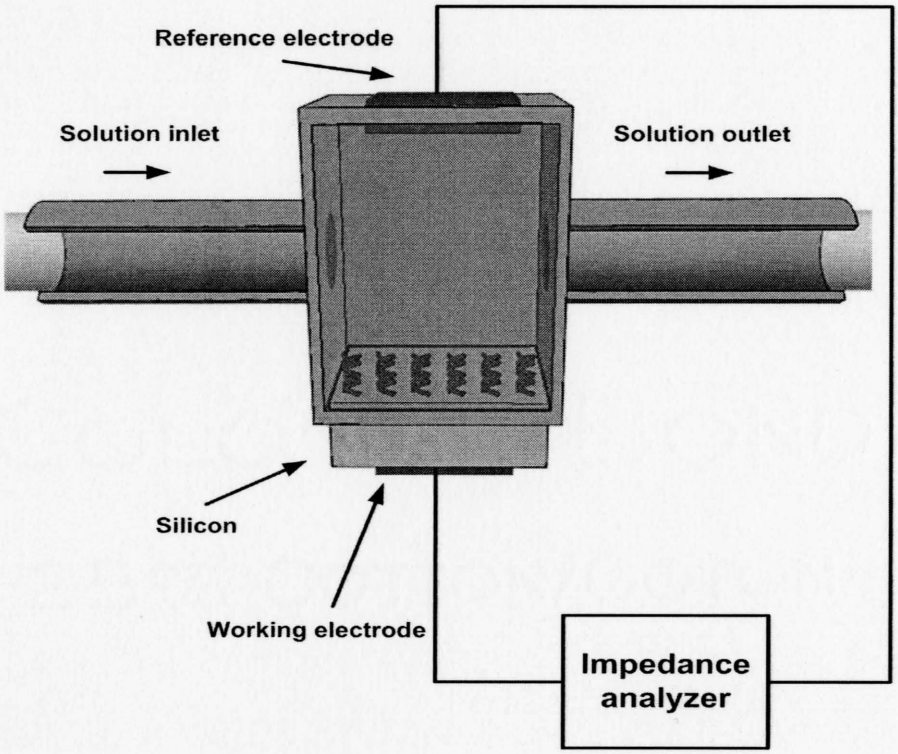

Figure 1.10 Impedance-based DNA sensor [24]

Another label-free technique that can sense DNA hybridization is monitoring its effects on integrated devices, such as the resonance frequency of a radio frequency (RF) inductor [25]. In this sensor, a metallic microstrip is used to construct an inductor on silicon. The shift in resonance frequency is shown to be as high as 8.9 GHz [25]. Such a sensor can be used to efficiently detect DNA hybridization. However, it does require high frequency electronics which means that cheaper microelectronics will not be sufficient for this type of sensor. In addition, we would require RF means of translating this change in frequency to a proportional voltage. This can increase the cost of such sensor cells.

Several techniques for DNA hybridization detection are not electrochemical in principle. One of these techniques involves the use of micro-electromechanical systems

(MEMS). Figure 1.11 shows a system consisting of two suspended micro-cantilever beams, on which DNA probes are immobilized [12]. Hybridization of target DNA molecules on one of the two cantilever beams causes a slight bending in the beam, due to a combined effect of gravity and change in surface tension due to hybridization. This bend offset between the two beams can be detected using a piezo-electric resistor, which can translate the mechanical offset to an electrical potential difference. Alternatively, monitoring laser reflection off the beams can provide information about the bending offset between the two beams [12].

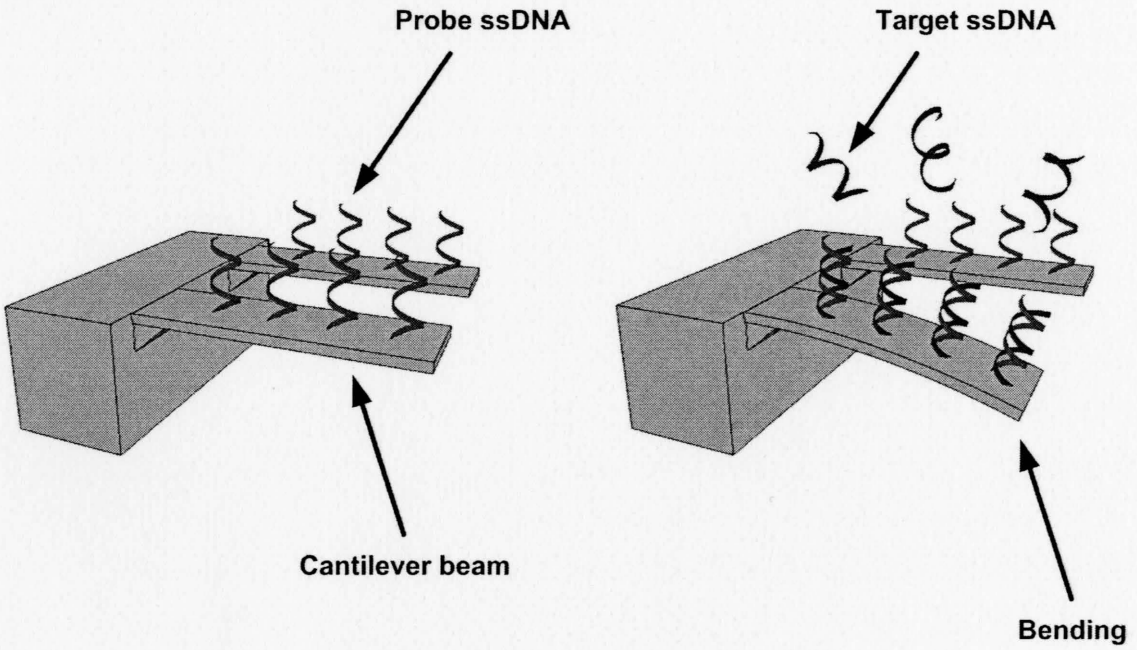

Figure 1.11 MEMS-based DNA sensor [12]

Biosensors for DNA hybridization detection can be designed using mass measurement techniques as well. In [25], a technique was shown using quartz crystal microbalance (QCM) for hybridization detection. The DNA probes were essentially immobilized on a crystal's surface. The oscillation frequency of the crystal will decrease upon hybridization, due to the increase in the mass of the crystal [21], [25].

Other techniques of label-free detection include detection of the changes in surface acoustic waves (SAW) due to molecular change (e.g. through hybridization) on the surface of a material [5]. The DNA-modified surface is excited at one edge, using a

crystal or electronic stimulus, and a receiver measures the received signal at the opposite edge, as shown in Figure 1.12. The change in the surface properties would determine its impedance to the acoustic wave. This would then be translated to an electric signal [5], [9]. Bulk acoustic wave methods for DNA hybridization detection have also been reported [11], [19]. The principle of operation is the same as the SAW sensor, but the cell generally requires a complicated structure, including an acoustic mirror and a piezo-electric crystal [19].

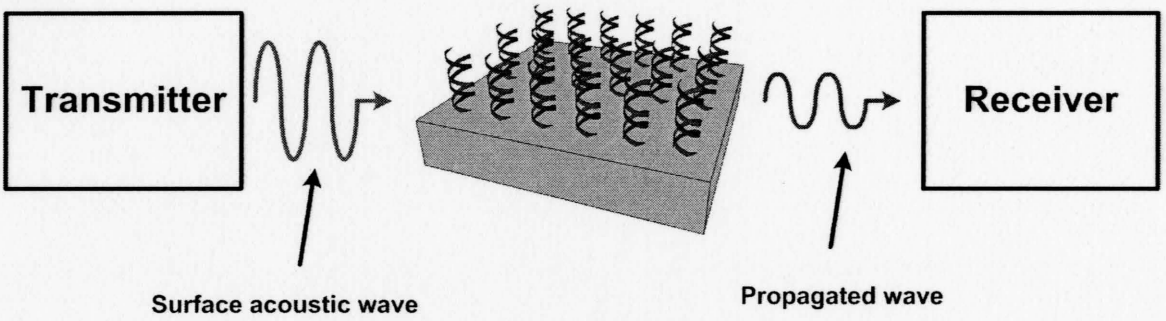

Figure 1.12 DNA hybridization detection by surface acoustic waves

One of the most appealing techniques for DNA hybridization detection is to use mainstream electronics for detection. Specifically, it has been shown [26-28] that metal-oxide-semiconductor field-effect transistors (MOSFETs) can be modified to act as DNA hybridization biosensors. By removing the gate metal and polysilicon off a FET device, and functionalizing the underlying dielectric with a tether molecule, ssDNA probes can be immobilized onto the dielectric surface. If target DNA molecules hybridize to these probes, the underlying FET structure will be affected by this increase of DNA density. This is due to the intrinsic negative charges on the DNA backbone mentioned earlier. The excess charge would induce a counter-charge from the surroundings, including the underlying silicon substrate (Figure 1.13) [3]. Electronically, the result of this action can be seen as a shift in the threshold voltage of the biosensor. Such a modified transistor will be referred to as a biological field-effect transistor (BioFET) in the remainder of this thesis [3].

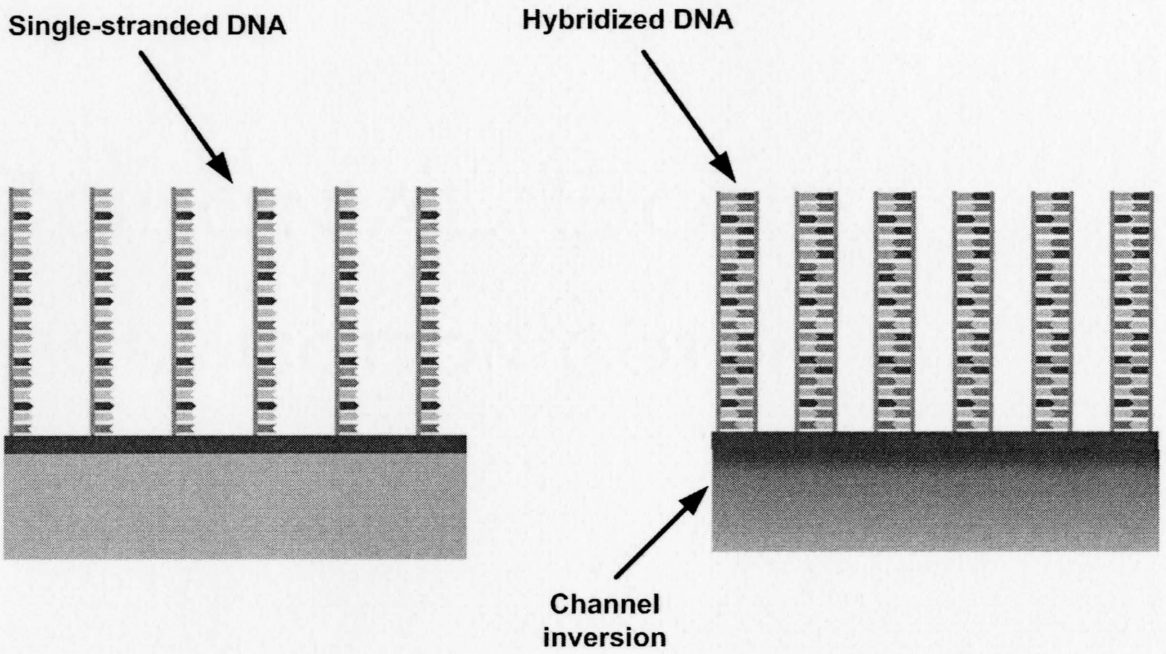

Figure 1.13 Effect of DNA hybridization on the channel of a MOSFET [3]

The advantages of this technique are numerous. Firstly, and most importantly, this provides a direct method of label-free electrical detection of DNA hybridization using cheap, mainstream complementary metal-oxide-semiconductor (CMOS) silicon technology. As such, the entire technology of precise and controlled silicon-based fabrication environments would be easily carried over to the biosensor. The biosensor array would be integrated with the accompanying electronics for signal processing on the same chip. In addition, the continued scaling down of CMOS technology would allow DNA microarrays with higher sensitivity, and higher density, to be realized. CMOS technology can also be used to manufacture low-power components. Combined with dense integration capabilities, DNA microarrays built this way would be ideal candidates for a potentially portable DNA analysis and pathogen detection device.

1.4 Organization of the Thesis

This thesis will address the modeling and interfacing of CMOS-based electronic biosensors to develop highly sensitive label-free DNA microarrays compatible with mainstream silicon-based microelectronics.

Chapter 2 will be devoted to the complete understanding and modeling of the response of the biological field-effect transistor (BioFET), including the electrostatics and chemistries involved. The chapter will start by introducing some of the main concepts of surface chemistry and thermodynamics, and will include a description of the electrostatic equations used to model the response of the BioFET to charged DNA molecules.

In chapter 3, the effects of varying different device parameters on the sensitivity of the BioFET will be addressed in light of the model developed in chapter 2. Several effects, such as DNA probe density, ionic concentration, pH of the solution and temperature, which can potentially affect the accuracy of the model, will be discussed.

Chapter 4 will focus on the noise analysis of the system, including the sources of different noise elements within the BioFET structure, the total expected SNR of the BioFET, and theoretical limits of detection.

Chapter 5 will introduce different interface circuit topologies to enhance the sensitivity and performance of the BioFET. Different methods of sensing will be investigated, including potentiometric, amperometric, and impedance based sensing. In addition, a design of a biochip DNA array in 0.8 μm CMOS technology will be described.

Chapter 6 will summarize the main contributions of this thesis, and will provide possibilities for future work, specifically towards kinetic modeling of the BioFET, 2D and 3D complications, and better noise modeling.

Chapter 2

ELECTROCHEMICAL MODELING OF BIOFETS

2.1 Introduction

The ability of the BioFET to sense the presence of charged molecules such as DNA oligonucleotides, is a result of the same phenomena that cause regular MOSFETs to work, namely, the field-effect. If a suspended charge is permanently placed in any location, it will tend to attract an equal amount of counter-charge from the neighboring media. This is because the charge will create a potential gradient in the surrounding area that is attractive for counter-charges. This is mathematically modeled by Gauss's law, which in its most general form, is given by

$$\nabla \cdot \varepsilon(\boldsymbol{r})\boldsymbol{E}(\boldsymbol{r}) = \rho(\boldsymbol{r}), \qquad 2.1$$

where $\boldsymbol{r}$ is the position vector (cm), $\boldsymbol{E}$ is the electric field vector (V/cm), ρ is the charge density (C/cm^3), and ε is the permittivity of an isotropic medium (F/cm).

The potential gradient created by the charge will attract any mobile counter-charges that exist in the nearby vicinity and repel similar charges. Should the immediate surrounding region be free of mobile charges, the electric field will continue to diverge until it impinges on a counter-charge.

A MOSFET consists of a conductive gate material, generally metal on polysilicon, an insulator, and an underlying semiconductor. Two terminals in the substrate constitute the drain and source terminals of the MOSFET. These are doped oppositely to the doping of the substrate so that a potential barrier does not allow current to flow through the substrate channel [36]. A simplified diagram of a MOSFET is given in Figure 2.1 [3].

Due to the existence of mobile charges in the semiconductor (holes and electrons), any excess charge that appears on the gate terminal will attract counter-charges from the nearest possible reservoir, which in this case happens to be the semiconductor substrate. Due to the dielectric, the charges in the semiconductor are confined to the channel area. If sufficient charge is introduced to the gate, enough charge might accumulate at the channel such that the drain and source terminals are electrically connected. In this case, if a voltage difference is applied between these two terminals, current will flow.

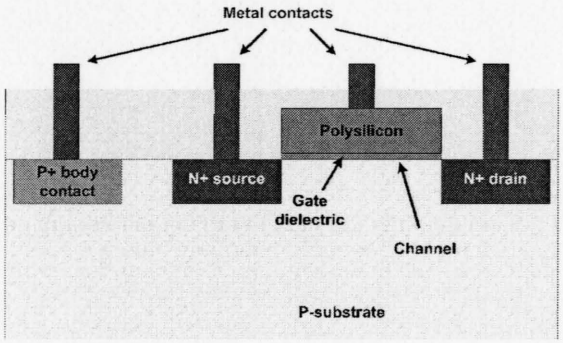

Figure 2.1 Simplified diagram of an N-type MOSFET [3]

In a BioFET, the gate metal and polysilicon are removed, and are replaced with an electrolytic aqueous solution, and a reference electrode, as shown in Figure 2.2 [39]. Now, the charges that can modulate the underlying semiconductor are any charges adjacent to the dielectric from the solution side. For a BioFET, a part of these charges comes from aggregated ions on the surface, just as in the case of the regular MOSFET, while another charge contributor is the charge contained within attached and/or hybridized DNA molecules.

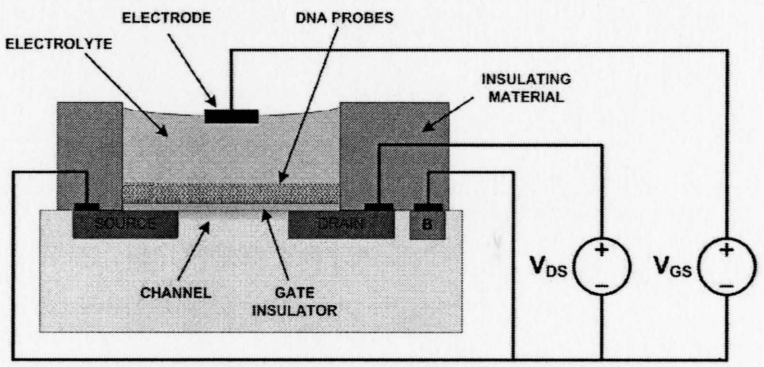

Figure 2.2 Conceptual diagram of a BioFET [39]

The main question that incites a need for mathematical modeling is: By how much does a given density of attached DNA molecules change the underlying semiconductor? Or, put in another form: What is the relationship between the change in the density of DNA molecules at the surface of the dielectric, and the change in the current conducted between the source and drain? After all, it is this change that reflects a successful increase of DNA density, which can be attributed to successful hybridization.

A very rudimentary view of the operation of the BioFET might suggest that the entire DNA charge will attract an equivalent charge from within the semiconductor, and therefore, the change in the channel's conductivity is readily derived from standard MOSFET theory [36]. However, this view is far from accurate, because in this case, the semiconductor is not the only medium that can provide mobile charges to satisfy the electric field of the DNA molecule. The ionic medium itself, in which the DNA resides, can redistribute its ions around the DNA such that an excess of charges will shield the DNA molecule from attracting any other charges. For high enough electrolytic concentrations, the counter-ions in the solution can succeed to shield the electric fields of the DNA molecule over a very short distance, so that the DNA molecule, at far enough distances, can be viewed as a neutral molecule. This "screening" of DNA charge is illustrated in Figure 2.3 [3].

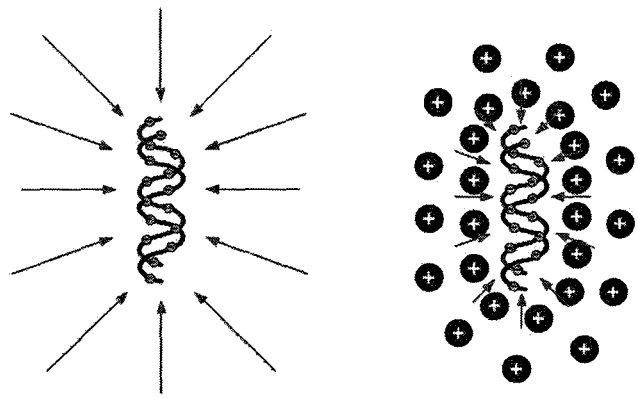

Figure 2.3 Charge screening of DNA in ionic solution [3]

The screening ability of the electrolytic solution is perhaps the most important phenomenon that limits the sensitivity of the BioFET's channel to the charged DNA molecules. It is therefore, essential to develop an electrostatic model that can relate the

amount of DNA molecules to the charge induced in the semiconductor while taking into account the screening capability of the solution. In this chapter, the physical systems of equations that relate the different phases of the BioFET structure will be presented [37], and numerical solutions of the model will be shown. Since the BioFET is a surface-based sensor, some insight into surface electrochemistry phenomena and possible interactions with the solution is required. This will be presented next.

2.2 Surface Electrochemical Phenomena

In the bulk of an electrolytic solution, the anions and cations that make up the dissolved salts are separated from each other by a few shells of water molecules. These ions have some degree of mobility and can be transported to different places within the bulk solution. However, in thermal equilibrium, the average relative locations of these ions with respect to each other will be such that the entire system is at minimum energy [30]. Now, removing one single ion from this grid will change the energy of the system. The average energy for ions of the same species as that removed will decrease, while the energies of the counter-ions will increase. Similarly, re-orienting the ions would also cause the energy to redistribute between the ions. We can conclude, with the aid of classical and statistical thermodynamics that at thermal equilibrium, for an isolated solution, the concentration of each and every species is constant within the solution phase. This is shown in Figure 2.4. A more rigorous proof can be shown with the aid of statistical mechanics and thermodynamics, but it will suffice here to take for granted that any non-uniform distribution of the constituents of the solution phase will not be thermodynamically favorable since it would lead to a state with lower entropy in an "isolated" system.

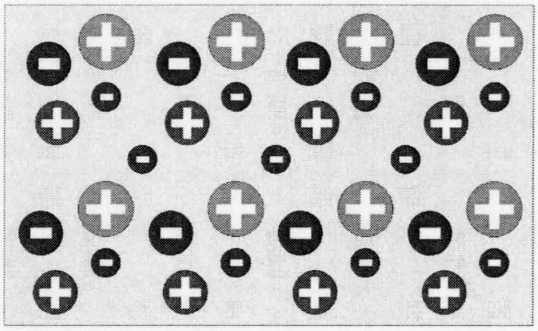

Figure 2.4 Uniform bulk distribution of ions

When a phase is in contact with another phase such that migration of one or more species is possible throughout the interface, then the situation changes drastically for the micro-population in this area [35]. The species will show more structure at the interface, and this can severely affect the chemical, electrical, and even optical properties of this phase. In order to understand what takes place at such an interface, it is important to make some assumptions to simplify the problem:

1. The ensemble is isobaric, i.e. no mechanical work is done on the system.
2. The ensemble is isothermal, so the temperature is constant in the entire ensemble.

With these assumptions, the only possible reason for a species to flow between phases would be to achieve lower energy. Since the temperature is constant, and no mechanical force is driving the species to cross the barrier, the species will cross the barrier if its chemical energy is reduced, meaning that it would move from a region with higher chemical potential to a region with lower chemical potential. In the language of thermodynamics, the chemical potential for a species *i* can be defined as [30]:

$$\mu_i = \frac{\partial G}{\partial n_i}_{\Delta T, \Delta P, \Delta S=0}, \qquad 2.2$$

where:

μ_i is the chemical potential of species *i* (J /mol),

G is the Gibbs free energy, defined as the total internal energy available for producing work under constant temperature and pressure (J),

n_i is the quantity of species *i* (mol), and

ΔT, ΔP, and ΔS are the changes in temperature (K), pressure (N/cm^2), and entropy (J/K), respectively.

It is important to notice that the origin of chemical and electrostatic potential are the same, namely, the electric fields between ions, dipoles, and other chemical forces which are all of electrostatic nature. The distinction is merely that of choice, and the definition chosen here is that the electrostatic potential will be a result of any macroscopically occurring electric field that is not at the individual level of ions and molecules.

The species begin to migrate between the phases towards states of lower chemical potential. If these species are charged, as they enter the second phase they leave behind a counter-charge, whose potential energy increases with each opposite charge that leaves the phase. This separation of charges, which occurs under chemical potential difference, will cause an electrostatic potential gradient that will tend to inhibit further diffusion of charges, much like what happens on the metallurgical junction of a PN diode [36]. At equilibrium, at each point along the interface, the chemical and electrical potentials vary such that their summation, the electrochemical potential, is constant [30], [34]. The electrochemical potential is equivalent to that of the Fermi level in semiconductors. Thus, under equilibrium, where no net transfer of matter takes place, the gradient of the electrochemical potential (Fermi level) is zero along the entire structure [42].

An example of such an interface is the interface between a metal phase, called an electrode, and an electrolyte solution. The diffusing species is the electron. If the electron leaves the electrode's surface, it will leave behind a positive charge, as shown in Figure 2.5. This charge will attract negative ions from the solution, by Gauss's law, and they will form an aggregate structure at the surface. This will cause an increase in the chemical potential of these negative ions, as they draw closer to each other. However, the increase in the chemical potential will be equal to the decrease in electrostatic potential, such that the electrochemical potential is constant throughout the surface of the electrolyte at thermal equilibrium. Such an electrode-electrolyte system, which allows crossing of electrons with no hindrance, is considered a non-polarized electrode [33]. The potential

drop across the interface at equilibrium is known as the electrode's potential. Large currents can flow in such a system for minor applied potentials [32].

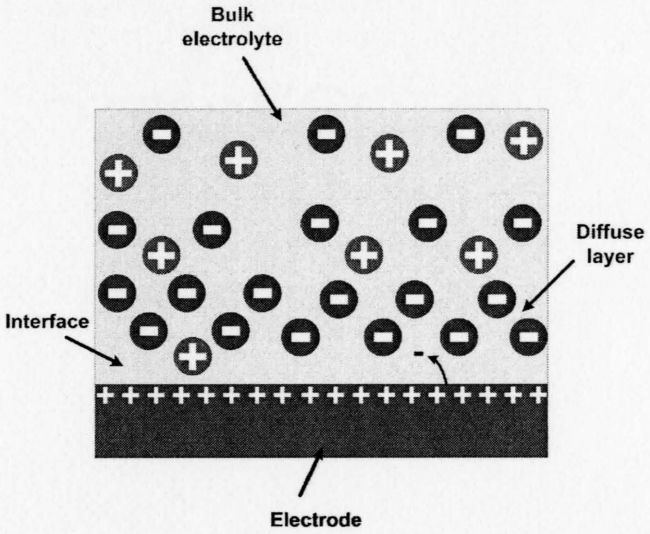

Figure 2.5 Formation of ionic diffuse region in the electrode-electrolyte interface

If the interface does not allow electrons to diffuse into the solution, then electrochemical equilibrium cannot be achieved between the two phases. However, if any excess charges appear on the electrode, this interface will act as a capacitance, drawing counter-ions from the solution to the interface [35]. Such an electrode is known as an ideally-polarized electrode [33]. It will sustain high potential differences without passing any current. In reality, any electrode-electrolyte interface exhibits different degrees of polarization at certain applied potentials. In both cases, however, the treatment of the thermal equilibrium potential profile along the surface of the solution is essentially the same. This profile is essential when describing the BioFET's response to DNA strands, and therefore must be considered when formulating a physical model for the BioFET.

2.2.1 The Gouy-Chapman Theory and the Double Layer

Explaining the profile of charge distribution within the surface of the electrolyte involves knowledge of all the processes that take place at the interface. However, a simplified model for this surface charging is given by the Gouy-Chapman model [32], [33], [35]. The following assumptions are made in this model:

1. Ions are treated as infinitesimally small particles.
2. The charge accumulated by these particles can be seen as a continuous charge distribution, rather than a discrete contribution from each ion.
3. The interface considered is sufficiently far away from any other interface, and 1-D approximations apply.

With these assumptions, Gouy and Chapman independently came up with a model for the spatial variation of the surface charge in the electrolyte. This charge is known as the double layer [35]. From statistical mechanics, we can relate the density of ions at a certain location in the solution phase to that in the bulk using Boltzmann's statistics and knowledge of the electrostatic potential difference between the particular location and the bulk. This is given by the following equations [34], [35]:

$$n^+(\boldsymbol{r}) = n_0^+ e^{-\frac{z^+ q\phi(\boldsymbol{r})}{kT}}$$
$$n^-(\boldsymbol{r}) = n_0^- e^{+\frac{z^- q\phi(\boldsymbol{r})}{kT}}, \qquad 2.3$$

where:

n^+, n^- are the position-dependent ionic concentrations for the positive and negative species, respectively (cm^{-3}),

n_0^+, n_0^- are the bulk ionic densities for the positive and negative species at zero potential, respectively (cm^{-3}),

z^+, z^- are the valences of the positive and negative ionic species, respectively,

q is the electronic charge = $1.602*10^{-19}$ Coulomb,

ϕ is the electrostatic potential with respect to the bulk (V),

k is Boltzmann's constant = $1.38*10^{-23}$ (J/K), and

T is the absolute temperature (K).

Equation 2.3 shows that the aggregation of a charged species at a location in the solution is due to a change in the electrostatic potential at that point from the value in the bulk, where the concentration takes its nominal value. Thus, the density of charges at a location is related to the potential through this statistical model. However, the presence of

charges causes a change in the potential as well, in a manner consistent with Poisson's equation, which is equivalent to Gauss's equation (equation 2.1):

$$\begin{aligned} \boldsymbol{E}(\boldsymbol{r}) &= -\nabla\phi(\boldsymbol{r}) \\ -\nabla\cdot\varepsilon(\boldsymbol{r})\nabla\phi(\boldsymbol{r}) &= \rho(\boldsymbol{r}) \end{aligned} \quad . \qquad 2.4$$

If the medium is isotropic, and the permittivity is constant, then Poisson's equation simplifies to:

$$\nabla^2\phi(\boldsymbol{r}) = \frac{-\rho(\boldsymbol{r})}{\varepsilon} . \qquad 2.5$$

The charge density in the solution phase is given by the summation of the positive and negative charge densities:

$$\rho(\boldsymbol{r}) = q(z^+n^+(\boldsymbol{r}) - z^-n^-(\boldsymbol{r})) . \qquad 2.6$$

Combining equations 2.3, 2.4, and 2.6, we arrive at what is known as the Poisson-Boltzmann (PB) equation, which is given here for the most general three-dimensional case, the isotropic homogeneous case, and a 1-D version of the equation, respectively:

$$\begin{aligned} \nabla\cdot\varepsilon(\boldsymbol{r})\nabla\phi(\boldsymbol{r}) &= -q\left(z^+n_0^+e^{-\frac{z^+q\phi(\boldsymbol{r})}{kT}} - z^-n_0^-e^{\frac{z^-q\phi(\boldsymbol{r})}{kT}}\right) \\ \nabla^2\phi(\boldsymbol{r}) &= -\frac{q}{\varepsilon}\left(z^+n_0^+e^{-\frac{z^+q\phi(\boldsymbol{r})}{kT}} - z^-n_0^-e^{\frac{z^-q\phi(\boldsymbol{r})}{kT}}\right) \\ \frac{d^2\phi(x)}{dx^2} &= -\frac{q}{\varepsilon}\left(z^+n_0^+e^{-\frac{z^+q\phi(x)}{kT}} - z^-n_0^-e^{\frac{z^-q\phi(x)}{kT}}\right) \end{aligned} \quad . \qquad 2.7$$

In a general solution containing different types of anions and cations, a summation of terms should be incorporated into equation 2.7, instead of just two charged contributions. However, in the case of a simple z-z electrolyte (valence of anions and cations are the same), the PB equation reduces to:

$$\frac{d^2\phi(x)}{dx^2} = -\frac{qzn_0}{\varepsilon}\left(e^{-\frac{z^+q\phi(x)}{kT}} - e^{\frac{z^-q\phi(x)}{kT}}\right) = \frac{2qzn_0}{\varepsilon}\sinh\left(\frac{zq\phi(x)}{kT}\right), \qquad 2.8$$

where the bulk density was also taken to be the same for anions and cations to preserve charge neutrality in the bulk of the solution, a trait common to all electrolytes and one

that follows directly from the previous discussion of thermodynamic equilibrium. Equation 2.8 is a nonlinear second order differential equation. For a given set of boundary conditions, we can arrive at a unique solution for this equation. Although an implicit, but nevertheless closed-form, solution for the case of a monovalent salt is obtainable, what is more important is relating the charge stored in the double layer to the potential drop across it, as this will enable us to calculate a value for the capacitance of this structure. To accomplish this, we utilize Figure 2.6 and note that the separation of charges causes an electric field that vanishes in the bulk of the electrolyte. Now, we may use the following identity:

$$\frac{d}{dx}\left(\frac{d\phi(x)}{dx}\right)^2 = 2\frac{d^2\phi(x)}{dx^2}\frac{d\phi(x)}{dx}, \tag{2.9}$$

to reduce the order of the PB equation, arriving at the following equation:

$$\frac{d}{dx}\left(\frac{d\phi(x)}{dx}\right)^2 = \frac{4qzn_0}{\varepsilon}\sinh\left(\frac{zq\phi(x)}{kT}\right)\frac{d\phi(x)}{dx}. \tag{2.10}$$

A simple integration of this equation, while realizing that the electrostatic potential and electric field vanish in the bulk, leads to a reduced-order equation which is given below:

$$\begin{aligned}
&\int_{x'=x}^{\infty}\frac{d}{dx'}\left(\frac{d\phi(x')}{dx'}\right)^2 dx' = \frac{4qzn_0}{\varepsilon}\int_{x'=x}^{\infty}\sinh\left(\frac{zq\phi(x')}{kT}\right)\frac{d\phi(x')}{dx'}dx' \\
&\phi'(\infty) - \left(\frac{d\phi(x)}{dx}\right)^2 = \frac{4kTn_0}{\varepsilon}\left(\cosh\left(\frac{zq\phi(\infty)}{kT}\right) - \cosh\left(\frac{zq\phi(x)}{kT}\right)\right). \\
&\frac{d\phi(x)}{dx} = \pm\left(\frac{4kTn_0}{\varepsilon}\left(\cosh\left(\frac{zq\phi(x)}{kT}\right) - 1\right)\right)^{1/2}
\end{aligned} \tag{2.11}$$

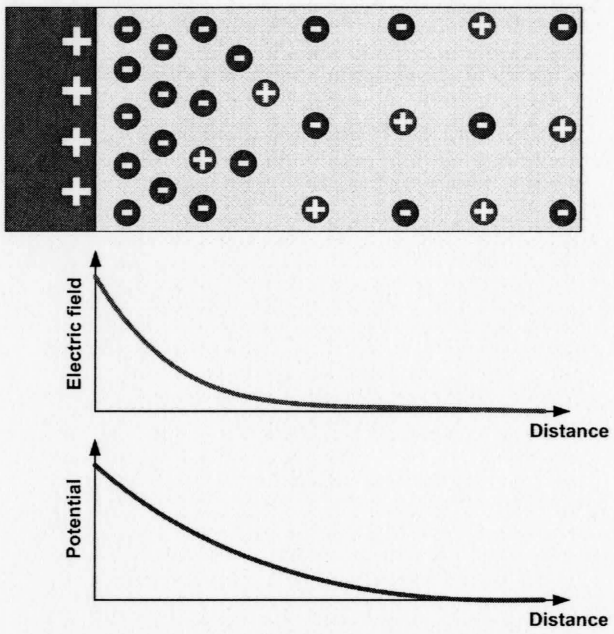

Figure 2.6 Illustration of the boundary conditions for an electrode-electrolyte interface

The proper selection of signs in equation 2.11 will depend on the electrode potential. If the electrode has a positive potential with respect to the bulk, then the negative sign should be selected, otherwise, the positive sign should be chosen. We can use a 1-D version of Gauss's law between the bulk and the surface of the electrolyte to determine the amount of charge stored within the double layer:

$$\varepsilon \oint \boldsymbol{E}.d\boldsymbol{s} = Q_{enclosed}$$

$$\varepsilon\left(E(\infty)-E(0)\right)=Q'$$

$$Q'=-\varepsilon E(0)=-\varepsilon\frac{d\phi(0)}{dx}=\mp\varepsilon\left(\frac{4kTn_0}{\varepsilon}\left(\cosh\left(\frac{zq\phi(x)}{kT}\right)-1\right)\right)^{1/2}, \qquad 2.12$$

$$Q'=-\sqrt{8kT\varepsilon n_0}\sinh\left(\frac{zq\phi(x)}{2kT}\right)$$

where:

Q' is the charge density per unit area (C/cm^2), integrated from the bulk of the electrolyte to the surface, and the identity:

$$\cosh(x)-1=2\sinh^2\left(\frac{x}{2}\right). \qquad 2.13$$

It is instructive to note that the sign for the charge is automatically determined by the odd hyperbolic sine function. We can calculate the differential (small-signal) capacitance of this electrode-electrolyte structure as follows [35]:

$$C = \left|\frac{dQ'}{d\phi(0)}\right| = \sqrt{\frac{2(zq)^2 \varepsilon n_0}{kT}} \cosh\left(\frac{zq\phi(0)}{2kT}\right). \qquad 2.14$$

In order to use equation 2.14, the contact potential $\phi(0)$ for the given interface must be known. Table 2.1 gives values for different contacts, with reference to the standard hydrogen electrode (SHE) [31]. Figure 2.7 shows the profile of the potential distribution, according to the Gouy-Chapman model, for different electrolyte concentrations and an interface potential of 0.5 volts. Figure 2.8 shows the small-signal capacitance at different bias voltages for different electrolytic concentrations.

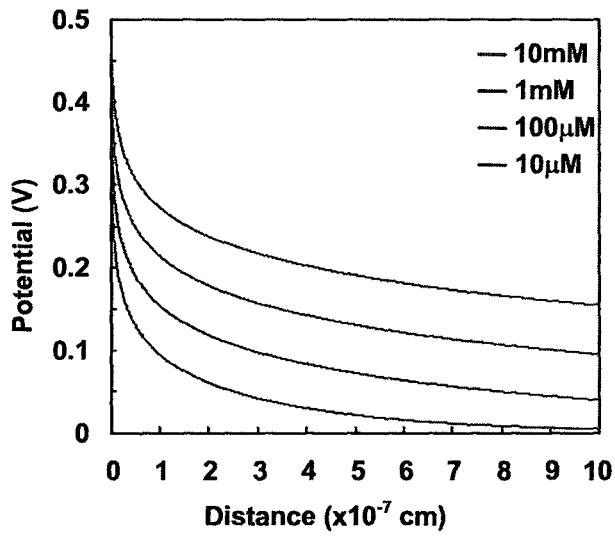

Figure 2.7 Gouy-Chapman potential profiles from electrode-electrolyte surface for a monovalent salt

Table 2.1 Electrode potential for several redox reactions at 298K [31]

Electrode reaction	E^0 vs SHE (V)
$F_2 + 2e^- \leftrightarrow 2F^-$	2.87
$S_2O_8 + 2e^- \leftrightarrow 2SO_4^{2-}$	1.96
$Ag^{2+} + 2e^- \leftrightarrow Ag^+$	1.94
$PbO_2 + 4H^+ + 2e^- \leftrightarrow Pb^{2+} + 2H_2O$	1.47
$Cr_2O_7^{2-} + 14H^+ + 6e^- \leftrightarrow 2Cr^{3+} + 7H_2O$	1.38
$Cl_2 + 2e^- \leftrightarrow 2Cl^-$	1.36
$O_2 + 4H^+ \leftrightarrow 2H_2O$	1.23
$MnO_2 + 4H^+ + 2e^- \leftrightarrow Mn^{2+} + 2H_2O$	1.23
$Ag^+ + e^- \leftrightarrow Ag$	0.8
$Hg_2^{2+} + 2e^- \leftrightarrow 2Hg$	0.8
$Fe^{3+} + e^- \leftrightarrow Fe^{2+}$	0.77
$O_2 + 2H^+ + 2e^- \leftrightarrow H_2O_2$	0.7
$Fe(CN)_6^{3-} + e^- \leftrightarrow Fe(CN)_6^{4-}$	0.36
$Cu^{2+} + 2e^- \leftrightarrow Cu$	0.34
$Hg_2Cl_2 + 2e^- \leftrightarrow 2Hg + 2Cl$	0.27
$AgCl + e^- \leftrightarrow Ag + Cl^-$	0.22
$2H^+ + 2e^- \leftrightarrow H_2$	0
$Pb^{2+} + 2e^- \leftrightarrow Pb$	-0.13
$As + 3H^+ + 3e^- \leftrightarrow AsH_3$	-0.23
$Ni^{2+} + 2e^- \leftrightarrow Ni$	-0.26
$Fe^{2+} + 2e^- \leftrightarrow Fe$	-0.44
$Zn^{2+} + 2e^- \leftrightarrow Zn$	-0.76
$Al^{3+} + 3e^- \leftrightarrow Al$	-1.67
$Mg^{2+} + 2e^- \leftrightarrow Mg$	-2.37
$Na^+ + e^- \leftrightarrow Na$	-2.71
$K^+ + e^- \leftrightarrow K$	-2.93
$Li^+ + e^- \leftrightarrow Li$	-3.04

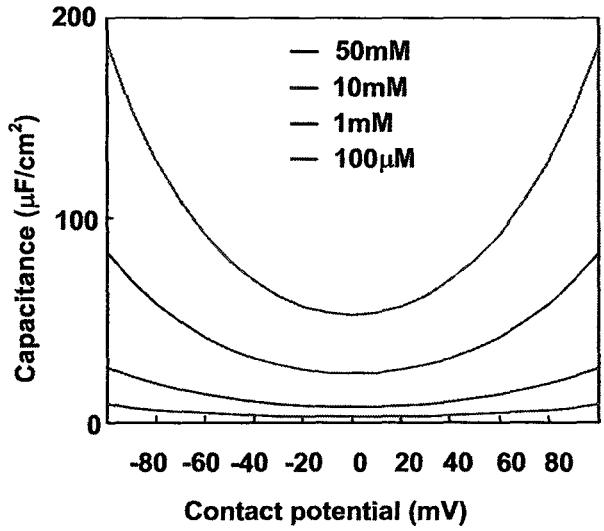

Figure 2.8 Gouy-Chapman C-V curves for different ionic concentrations of a 1-1 electrolyte

Although the Gouy-Chapman model for the double layer can predict accurate results for different electrode-electrolyte systems, it is known to overestimate the charge density at high enough electrode potentials, as can be seen from the exponentially rising capacitance curve of Figure 2.8. The main reason behind this is the theory's neglect of the discreteness of the ions in the solution, leading to continuous equations that can behave erratically at locations where microstructure is important. Stern modified the Gouy-Chapman model by speculating that the PB equations do not apply at regions that are extremely close to the electrode's surface [35]. This is because ions cannot approach the surface, despite its favorable potential, closer than a certain range. This range is equal to the ionic radius of the ion, plus the excess radius formed by the solvation layer of water molecules that coalesce around the ion, prohibiting it from re-uniting with the counter-ion in the solution. This is illustrated in Figure 2.9. In order for the ions to approach the surface, they have to be liberated from their shell, a process that requires energy. Thus, under moderately low electrode potentials, the ions remain within some distance from the surface, separated by a region free of charges, acting like an ideal capacitor. When the hydrated ions are at their closest distance from the surface, their centers form a plane known as the outer Helmholtz plane (OHP). Figure 2.9 shows this plane of closest approach. The Stern capacitance should be added in series to the double layer

capacitance. This will result in more reasonable charge densities for high enough electrode potentials. This modified model is known as the Gouy-Chapman-Stern model. Figure 2.10 shows examples of capacitance curves calculated with the standard and modified double layer models. In this figure, The Stern layer was given a constant capacitance of 100μm/cm^2.

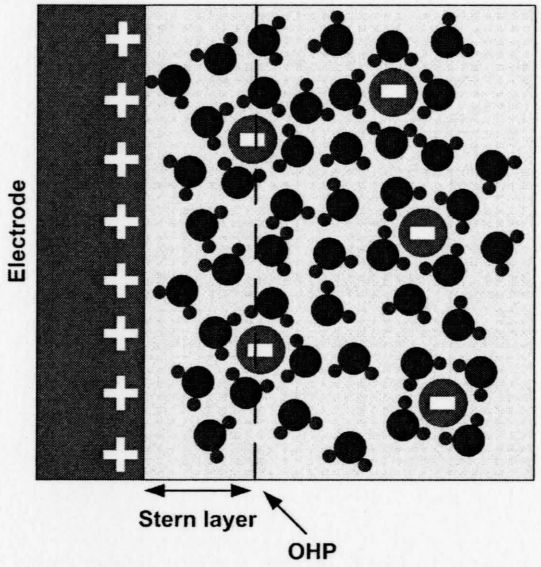

Figure 2.9 Illustration of the Stern layer and the outer Helmholtz plane (OHP)

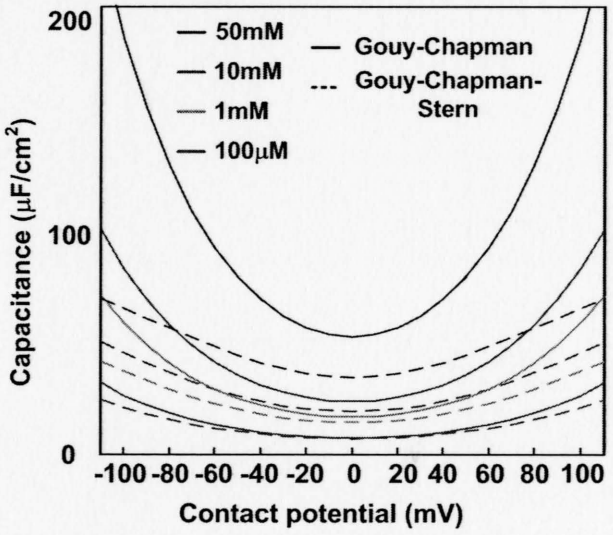

Figure 2.10 C-V curves with (dashed lines) and without (solid lines) the Stern modification

2.2.2 Adsorption Effects

In addition to surface charge aggregation due to the double layer formation, other processes can occur that alter the expected charge density at the surface for a given electrode potential. One of these effects is ionic adsorption on the surface of the electrode [32], [33]. Some ions can be liberated from their hydration shells and adhere to the surface of the electrode. The double layer model presented in section 2.1.1 does not capture this effect. If a strong chemical affinity for the association exists, specific adsorption will occur. However, for this chemical reaction to take place, the ions must be in close proximity to the surface. At lower electrode potentials, the density of charges in the OHP might not be enough for significant adsorption to occur. In addition, if the de-solvation energy is higher than that of chemical adsorption (chemisorption), specific adsorption will not occur. It is therefore important to know whether adsorption can occur or not for a given electrode/electrolyte interface. Adsorption can result in very different capacitance behavior, particularly at potentials that are away from the potential of zero charge, at which the capacitance is minimum.

In addition to the adsorption of hydrated electrolyte ions, aquatic solutions always have a percentage of hydrogen and hydroxyl ions in them [3]. This is due to the following association-dissociation equation:

$$H_2O \overset{K_{eq}}{\leftrightarrow} H^+ + OH^- . \tag{2.15}$$

Equation 2.15 is in equilibrium, and the equilibrium constant is given by:

$$K_{eq} = \frac{[H^+][OH^-]}{[H_2O]}, \tag{2.16}$$

where $[H^+]$, $[OH^-]$, and $[H_2O]$ are the equilibrium molar concentrations of hydrogen ions, hydroxyl ions, and water molecules, respectively.

At room temperature, the equilibrium concentration of liquid water molecules is around 55.56 M. Experimentally; we find that at room temperature,

$$K_{eq}[H_2O] = [H^+][OH^-] = 1 \times 10^{-14}, \tag{2.17}$$

which means that the product of the concentrations of the two ionic species is constant. When no other species contribute to these ions (like acids or bases), then their values are equal, due to the neutrality of the solution. We therefore have:

$$[H^+]=[OH^-]=1\times10^{-7}\mathrm{M}. \qquad 2.18$$

These concentrations, when measured in log scale, correspond to the *pH* and *pOH* values of the solution. Statistically, these ions behave exactly like the salt ions in the solution would, and are therefore expected to obey Boltzmann's statistics. Therefore, in the vicinity of the double layer, where the solution's potential is varying, one would expect that the local population of hydrogen and hydroxyl ions would relate to their values at the solution bulk as follows:

$$\begin{aligned}[H^+]&=[H^+]_0 e^{\frac{-q\phi}{kT}}\\ [OH^+]&=[OH^-]_0 e^{\frac{q\phi}{kT}}\end{aligned}. \qquad 2.19$$

A point worth mentioning is that although we acknowledge the presence of these ions, we did not consider them in the formulation of the Gouy-Chapman model for a monovalent salt dissolved in water. The reason is that at such low H^+ and OH concentrations, these ions will hardly affect the potential resulting by the much more abundant salt ions. Even for the low salt concentrations of 1mM, the concentrations of the water ions are three orders of magnitude less. Nevertheless, if these ions can be specifically adsorbed at the interface, then their accurate density at the interface is needed, and this is obtained using equation 2.19.

In the model of the BioFET that will be shown, the two surface phenomena of the double layer formation and proton adsorption play a crucial role in determining the response of the underlying semiconductor to the charged DNA molecules. It will be shown how the diffuse layer, when permeated by the DNA, can cause screening of the DNA charge, thereby reducing the overall sensitivity. In addition, the presence of negatively charged DNA molecules will allow more hydrogen ions to exist in the vicinity. If the ions belong to the double layer theory, then their shielding capability will be no more than that of the salt ions and can therefore be neglected. However, if their

equilibrium concentration is such that the adsorption will cause a significant amount of charge to appear at the surface, then they might severely screen the DNA charge and cause a reduction in the overall sensitivity.

2.3 Modeling the Response of the BioFET

The BioFET structure was shown in Figure 2.2 [39]. It essentially consists of an ion-sensitive Field-Effect Transistor (ISFET) structure. ISFET structures were introduced by Bergveld [40] in the 1970s and were used as pH sensors. It consists of a regular MOSFET transistor, but with the gate metal and polysilicon removed, generally by post-processing, and the insulator exposed. The gate area is filled with an electrolytic solution and a reference electrode is made in contact with the solution. The reference electrode bias is needed to establish a potential at the electrolyte-insulator surface so as to provide repeatable conditions and avoid having floating points in the BioFET circuit. In addition, the DNA molecules are not generally sufficient to cause a full inversion in the channel. It is therefore important to provide an additional source of charges, which in this case is an external voltage source.

The BioFET can be seen as an electrochemical cell, which for a solution of NaCl, a dielectric made of silicon oxide (SiO_2), and a silicon substrate, would have the following cell diagram description [30]:

$$\mathrm{MI} \mid \mathrm{NaCl} \mid \mathrm{SiO_2} \mid \mathrm{Si} \mid \mathrm{MII}, \qquad 2.20$$

where MI is the reference electrode, and MII is the Ohmic contact to the substrate. Of course, there are also two other contacts, namely, the source and the drain. These two contacts add a second dimension to the complexity of the electrostatic distribution when a bias is applied between them. Therefore, this lateral electrical field will be dealt with using an approximation that is common in standard MOS transistor theory. For now, the main focus will be on solving a one-dimensional structure that extends from the reference electrode MI to the substrate contact MII.

2.3.1 Assumptions Made in Developing BioFET Equations

Several physical assumptions are made to simplify the analysis of the BioFET structure. Some of these assumptions are common with MOS transistor modeling. For completeness, all the assumptions are outlined here:

1. Semiconductor substrate is uniformly doped: non-uniform doping is typically used in modern CMOS processes, but this is not considered here.
2. Full immobility of DNA membrane charges: It is important to assume that the DNA molecules will not compress or re-orient in the presence of electrical bias. Such effects will change the geometry of the model and will cause complexities.
3. DNA membrane cannot dissociate from functionalized surface (strong covalent bonds): This assumption also allows the geometry and concentration of DNA molecules to be independent of the applied bias, simplifying the analysis.
4. Permeability of membrane to electrolyte ions: It is assumed that the DNA molecules are not too densely packed so as not to allow diffusion of ions. The diffusivity of ions within the DNA layer is assumed equal to that in the bulk.
5. Electrostatic 1-D approximations (large, thin device): The DNA charges are considered spread throughout a charged membrane area, rather than being discrete, which would necessitate two-dimensional modeling.
6. Electrostatic potential drop across electrode-electrolyte interface is constant with applied bias (non-polarized electrode): This assumption is equivalent to stating that oxidation-reduction (redox) reactions are possible at this interface and that equilibrium is always maintained.
7. Doping concentration of substrate is higher than minority carriers concentration: This would allow the simplification assumption that the concentration of the majority carriers in the bulk of the silicon is equal to the doping concentration.
8. Non-degenerate semiconductor assumed in all inversion regions: This assumption is needed to qualify Maxwell-Boltzmann statistical equations for the charge carriers rather than Fermi-Dirac statistics, which lead to more complicated formulations.

9. Specific adsorption of salt ions onto the insulator surface is neglected.
10. Charge sheet model is assumed when calculating drain current: This model allows a simplified derivation of the current in the channel of the BioFET.
11. Gradual channel approximation is used when calculating drain current.
12. No source-body, drain-body, or channel-body currents are considered: The potential barriers at these junctions are assumed high enough that leakage currents through these interfaces are negligible.
13. Very low interface trap density: This is required so that the trapped charge density is independent of the applied bias.
14. Tunneling and insulator breakdown effects are neglected. It is assumed that the insulator is perfect with no mobile ions.
15. Ionic presence of hydrogen (pH) and hydroxide (pOH) ions do not affect the diffuse layer's potential drop since they have very low concentrations.

2.3.2 Potential Diagram and Solution of the BioFET

Figure 2.11 shows a potential diagram of the BioFET, where V_{GB} refers to the voltage applied between the reference electrode and the counter electrode connected to the body of the BioFET. It is standard practice in semiconductor theory to take the reference potential as that of an electron in vacuum. However, for electrolytic solutions, the reference is usually taken as that of the standard hydrogen electrode (SHE). Figure 2.12 shows a comparison between different electrode potentials and that of the vacuum scale [44]. The equilibrium potential of an electrode-electrolyte solution is generally given by Nernst equation [30]:

$$E=E^{0}-\frac{kT}{zq}\ln\left(\frac{[red]}{[ox]}\right), \qquad 2.21$$

where:

E is the electrode potential (V),

E^{0} is the standard electrode potential, measured at ambient temperature of 298K, and electrolyte concentration of 1M (V), and

[*red*] and [*ox*] are the activities of the reduced and oxidized species (M), taken as a first approximation to be equal to their molar concentrations.

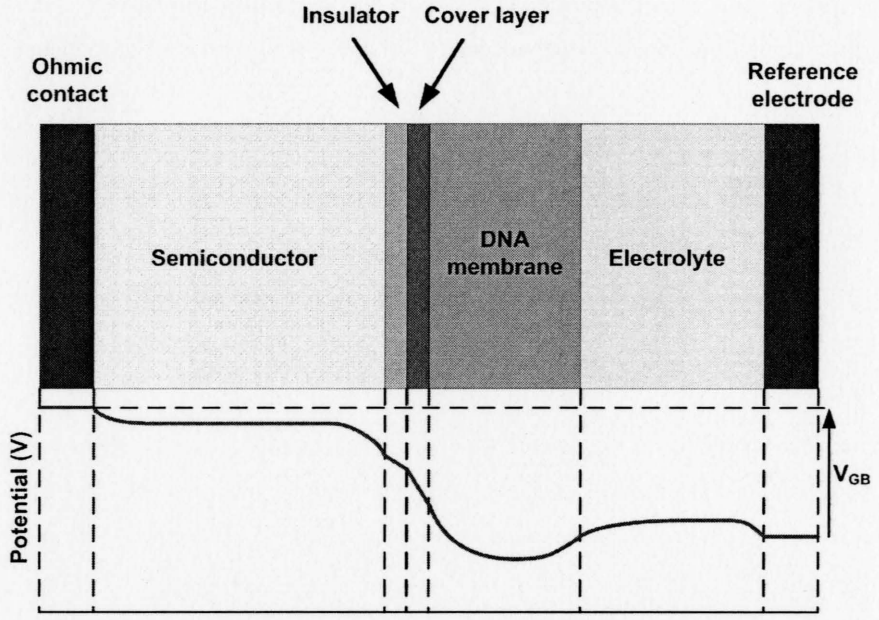

Figure 2.11 Sample potential diagram for a BioFET (not to scale)

The Nernst equation relates the chemical potential of the electron in the electrode to that in the solution. The electrostatic potential drop between the electrode and electrolyte phases is dependent on the chemical potential difference between the electrons in the electrode and in the reduced species of the electrolyte. At equilibrium, no net charge transfer happens, and the redox reaction is in equilibrium at the interface. A constant potential appears across this interface such that the electrochemical potential in both phases is constant. In a BioFET, this equilibrium electrostatic potential drop will remain constant, independent of the applied bias on the reference electrode. This is because the dielectric will not allow any current to flow across the BioFET structure and therefore, the electrode-electrolyte interface is always in equilibrium. As will be shown later, the capacitance of this interface will allow for AC equilibrium disturbances due to charging and discharging of the interface. However, at DC equilibrium, the electrode potential with respect to the bulk solution will always be constant, and equilibrium will be maintained by the redox reaction at the interface.

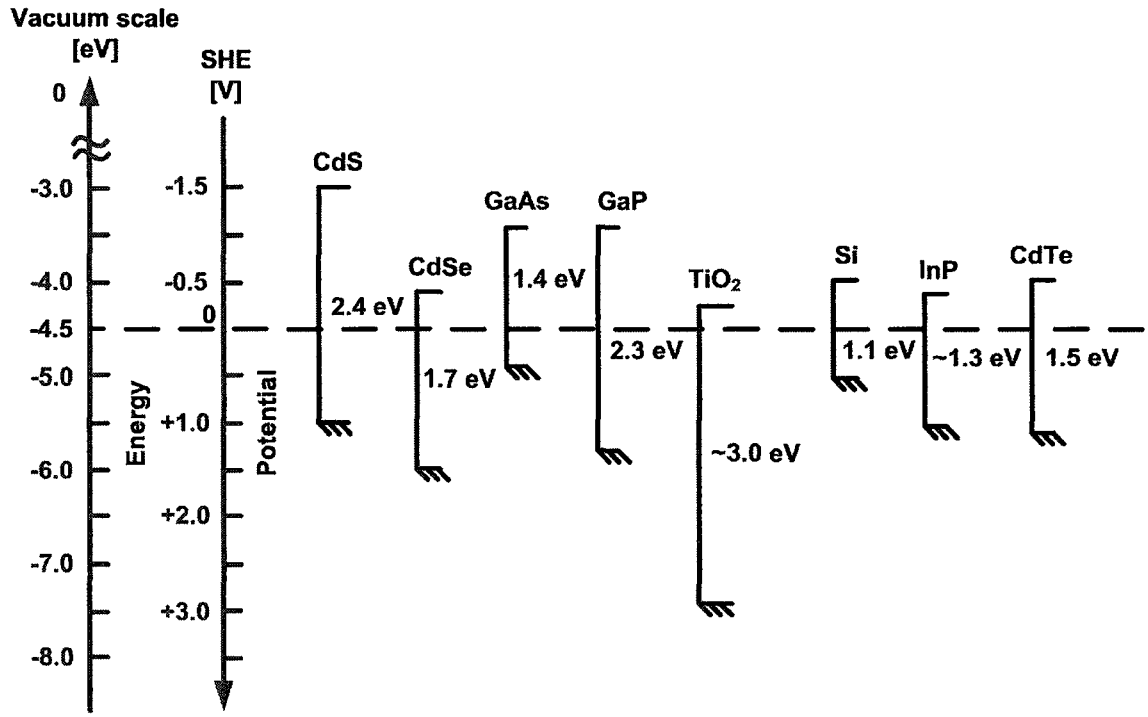

Figure 2.12 Relative band edge positions for several elemental and compound semiconductors, in vacuum scale and SHE scale [44]

Charges on both sides of the dielectric interface will accumulate, causing a bending of the bands in both the semiconductor and electrolyte [34]. Under no applied bias, the amount of bending of the semiconductor band diagram needs to be calculated since this term contributes to the threshold voltage calculation of the BioFET structure. This bending of the semiconductor bands is a result of many different phenomena [36], [37]:

1. Due to the differences in the chemical potentials between the electrolyte and semiconductor, and since they are both in equilibrium, by virtue of the metallic contact connecting them with zero bias, their electrostatic potentials must be different in order to maintain electrochemical equilibrium. Therefore, excess charges will accumulate at both sides of the dielectric interface, just like a parallel plate capacitor. The excess charges will induce potential profiles in the electrolyte, insulator and semiconductor, in a manner consistent with Poisson's equations.

2. The discontinuity of the periodic lattice at the semiconductor-insulator causes an excess of states at the interface. These states can be filled by electrons, causing accumulation of charge at the surface, which increases the bending of the semiconductor. To a first degree approximation, these states can be treated as filled, regardless of the applied potential.
3. Fixed charges can reside within the semiconductor surface, as well as within the insulator itself. These fixed charges contribute to the bending of the semiconductor and result in a change in the threshold voltage.
4. Fixed charges within the electrolyte interface, caused by the immobilization of charged molecules, contribute to the bending of the semiconductor's bands. Although a change in this charge represents the DNA hybridization signal, it is important to relate this value to the threshold voltage. This is important because a change in the charged DNA strands would cause changes in the semiconductor band bending, as well as in the electrolyte's potential profile. It would not be sufficient to treat the DNA charges as fixed charges that only affect the semiconductor's band bending.

Figure 2.13 shows a BioFET electron energy band diagram before and after thermal equilibrium [37]. An additional insulating layer, which is generally used to tether the DNA molecules to the insulator, is added and named the cover layer. The Fermi level, corresponding to the electrochemical potential, is constant along the structure. The different electrostatic potential drops are denoted as follows [37]:

ψ_0: The electrostatic potential with respect to the bulk electrolyte due to charge accumulation on the electrolyte-insulator interface.

ψ_s: The electrostatic potential drop due to charge accumulation on the insulator-semiconductor interface.

ψ_{ins}: The electrostatic potential drop in the insulator.

ψ_{cl}: The electrostatic potential drop in the cover layer.

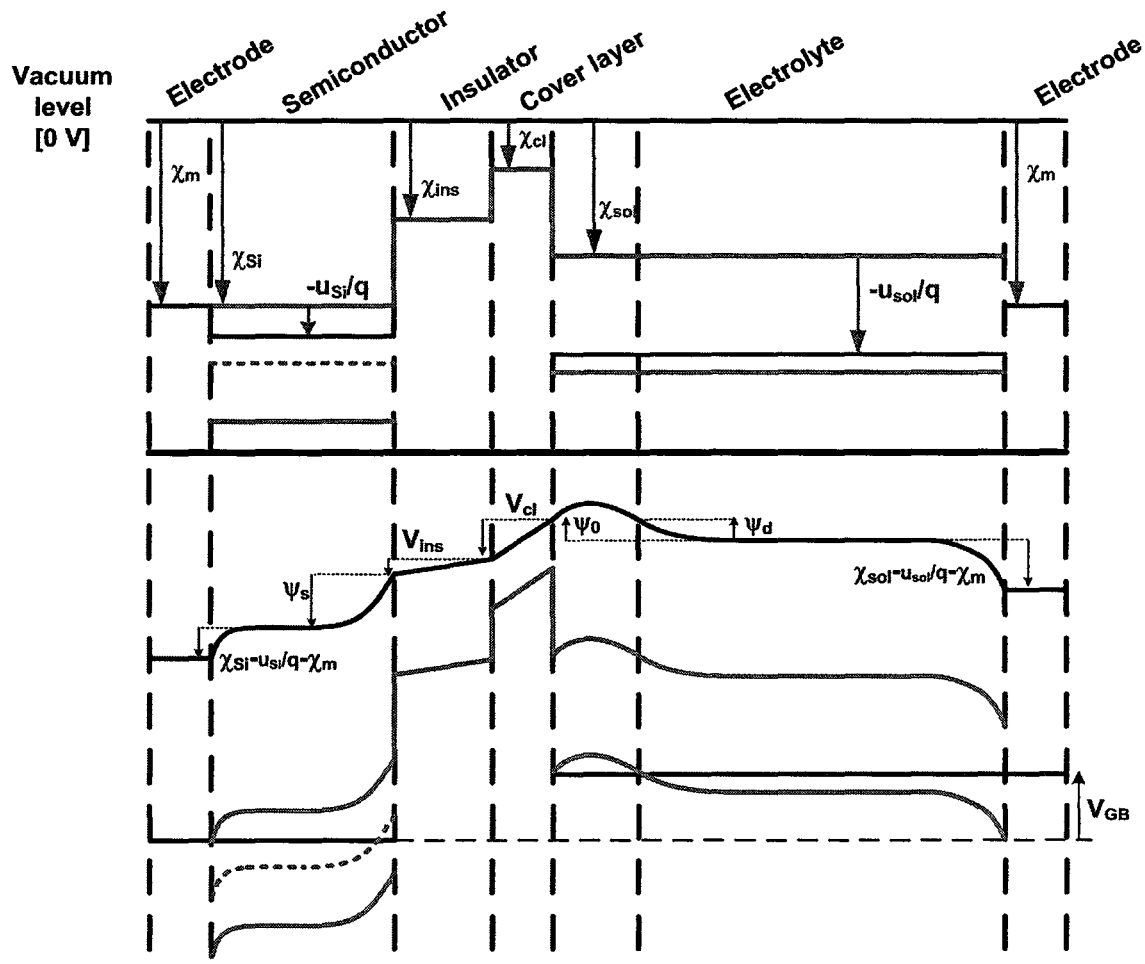

Figure 2.13 BioFET's energy band diagram a) before equilibrium, b) at thermal equilibrium [37]

These are the potential drops that are expected to vary with the application of a bias potential. Other potential drops in the system are constant with applied bias, and these include the following:

χ_m, χ_{sol}, χ_s: electron affinities of the metal electrode, electrolyte and semiconductor, respectively (V).

u_s, u_{sol}: the chemical potential energies of electrons in the semiconductor and in the electrolyte, respectively (eV).

The chemical potential energy of the semiconductor is related to the Fermi potential by the following equation [36], [42]:

$$u_{Si} = -\left(\frac{E_g}{2} + q\phi_F\right), \tag{2.22}$$

where E_g is the band gap energy for the semiconductor (J), and ϕ_F is the Fermi potential (V). If the energies are given in electron volts rather than Joules, then the Fermi potential should not be multiplied by the electronic charge in equation 2.22. The Fermi potential, for a semiconductor in which the doping density is significantly higher than the thermally generated carriers, is approximated by:

$$\phi_F = \pm\frac{kT}{q}\ln\left(\frac{N}{n_i}\right), \tag{2.23}$$

where N, n_i are the dopant and intrinsic carrier densities, respectively (cm^{-3}). The positive sign is used when the semiconductor is P-type, and the negative when it is N-type. The solution's chemical potential energy generally follows a similar formula, which is the Nernst equation:

$$u_{sol} = u_{sol,0} + \frac{kT}{z}\ln\left(\frac{[red]}{[ox]}\right), \tag{2.24}$$

where $u_{sol,0}$ is the standard chemical potential energy for the electrode-electrolyte system (J). By invoking a potential balance around the BioFET structure in Figure 2.13, we have [37]:

$$\begin{aligned} -qV_{GB} &= (q\chi_m - q\chi_{sol}) + (q\chi_m + u_{sol} - q\chi_{sol}) + q\psi_0 + (q\chi_{sol} - q\chi_{cl}) \\ &-q\psi_{cl} + (q\chi_{cl} - q\chi_{ins}) - q\psi_{ins} + (q\chi_{ins} - q\chi_s) - q\psi_s + q\chi_s - u_s - q\chi_m \\ V_{GB} &= \chi_{sol} - \chi_s - \frac{u_{sol}}{q} + \frac{u_s}{q} - \psi_0 + \psi_{cl} + \psi_{ins} + \psi_s \end{aligned} \tag{2.25}$$

Now, the potential drop across the insulator is related to the charge on either side of the insulator divided by the capacitance. If we denote the charge density per unit area for the semiconductor and electrolyte by σ_s and σ_e, respectively (C/cm^2), and the capacitances of the insulator and the cover layer per unit area as C_{ins}, C_{cl}, respectively (F/cm^2), then we have:

$$\psi_{ins} = \frac{\sigma_e}{C_{ins}} = \frac{-\sigma_s}{C_{ins}}$$
$$\psi_{cl} = \frac{\sigma_e}{C_{cl}} = \frac{-\sigma_s}{C_{cl}} \quad . \qquad 2.26$$

If excess fixed charges exist at the insulator/semiconductor surface, within the insulator, or within the cover layer, they will affect the potential drop across the cover layer, insulator, electrolyte surface, and semiconductor surface. As long as these charges are fixed and not potential-dependent, even if they are distributed within the insulator and cover layer, they can be reduced to an equivalent charge density at the semiconductor surface σ_f. Of course, this will alter the actual potential profile within the insulator, which is not needed, but will not affect the calculated charge density at the semiconductor surface or the electrolyte. The only effect is that we will notice a non-smooth transition in the potential profile as we enter the insulator, due to the sudden charge aggregate at the surface. This is illustrated in Figure 2.14. Of course, this corner would exist even if we do not reflect the charges to the surface, due to the variations in the permittivities of both phases. With these charges, equation 2.26 is modified to:

$$\psi_{ins} = \frac{\sigma_e}{C_{ins}} = \frac{-(\sigma_s + \sigma_f)}{C_{ins}}$$
$$\psi_{cl} = \frac{\sigma_e}{C_{cl}} = \frac{-(\sigma_s + \sigma_f)}{C_{cl}} \quad . \qquad 2.27$$

The final potential equation is given by:

$$V_{GB} = \chi_{sol} - \chi_{Si} - \frac{u_{sol}}{q} + \frac{u_s}{q} - \psi_0 - \frac{(\sigma_s + \sigma_f)}{C_{eff}} + \psi_s \,, \qquad 2.28$$

where C_{eff} is the equivalent series combination of C_{cl} and C_{ins}, and σ_f is the equivalent fixed charge density at the semiconductor surface (C/cm^2). Equation 2.28 has three unknown variables for a given bias, and therefore, two more equations are needed. The semiconductor's potential drop is related to the charge density by Poisson's equation, which, when applied with the semiconductor's charged population in mind (electrons, holes, and ionized dopants), yields the following equation:

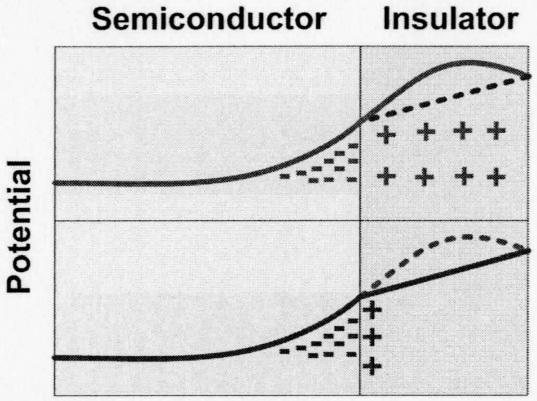

Figure 2.14 Referring fixed charges in the insulator to the semiconductor surface

$$\frac{d^2\psi_s}{dx^2} = -\frac{q}{\varepsilon_s}\left(p(x) - n(x) \mp N\right), \tag{2.29}$$

where p and n are the densities of electrons and holes (cm^{-3}), and ε_s is the permittivity of the semiconductor (F/cm). The negative sign (-N) is taken for a P-type semiconductor, and the positive for N-type. The electron and hole densities are related to the intrinsic densities p_0, n_0, and the potential from the bulk by the approximate equations:

$$\begin{aligned} p &= p_0 e^{-\beta\psi} \\ n &= n_0 e^{\beta\psi} \end{aligned}, \tag{2.30}$$

where:

$$\beta = \frac{q}{kT}. \tag{2.31}$$

In addition, the equilibrium values of the electrons and holes are related to the intrinsic concentration n_i through the Fermi potential:

$$\begin{aligned} p_0 &= n_i e^{\beta\phi_F} \\ n_0 &= n_i e^{-\beta\phi_F} \end{aligned}. \tag{2.32}$$

Although equation 2.29 cannot be solved explicitly for the potential, it can give us a closed form expression for the potential-charge relationship. In a manner very similar to the way equation 2.8 was solved, we can arrive at the following relationship:

$$\sigma_s = \mathrm{sgn}(-\psi_s)\sqrt{2kT\varepsilon_s n_i}\left(e^{-\beta\phi_F}\left(e^{\beta\psi_s} - \beta\psi_s - 1\right) + e^{\beta\phi_F}\left(e^{-\beta\psi_s} + \beta\psi_s - 1\right)\right)^{1/2}. \tag{2.33}$$

With this equation known, we now need a third equation that somehow relates ψ_0 and ψ_s. Although there exists indeed a one-to-one correspondence between these two quantities, leading to a unique solution to the system, it cannot be expressed analytically. What we will do instead is to relate these two quantities through another set of equations that stem from physical phenomena.

The main link that connects the semiconductor variables to those of the electrolyte is charge neutrality around the entire structure [37]. Local charge neutralities are maintained at the electrode-electrolyte and the semiconductor-electrode interface. Therefore, the charges accumulated at those interfaces will not interfere with the expected charge neutrality between the bulk electrolyte and bulk semiconductor. As a result, for charge neutrality, we require that

$$\sigma_s + \sigma_f + \sigma_e = 0. \qquad 2.34$$

With this link equation established, what remains is to link the total charge accumulated in the electrolyte to the electrolyte surface potential. Once this is done, then we will have a complete set of equations that can be solved together to get the response of the BioFET. Three different electrolyte charge contributions are considered in this model [37]:

1. The presence of the DNA charges.
2. The ionic presence (Gouy-Chapman-Stern model).
3. Adsorbed hydrogen and hydroxyl charges at the surface of the insulator.

2.3.2.1 Modeling the Fixed DNA Charges

The DNA charges are assumed to be a continuous distribution of charge in the region occupied by the molecules. This facilitates the 1-D modeling discussed here. Figure 2.15 illustrates this assumption in the model. However, a main distinction between this charged region and the possible charge distribution in the insulator (mentioned earlier), is that the DNA region is assumed to be perfectly permeable to ions, allowing them to approach the insulator surface. Poisson's equation can be used to relate the potential profile with the charges due to the presence of ions and fixed DNA charges. If we incorporate both of these contributions into Poisson's equation, we get the following:

$$\frac{d^2\psi(x)}{dx^2} = \frac{2qzn_0}{\varepsilon_m}\sinh\left(z\beta\psi(x)\right) - \frac{qN_m}{\varepsilon_m}, \qquad 2.35$$

where:

N_m is the charge density of the DNA membrane (cm^{-3}), and

ε_m is the permittivity of the DNA-permeated solution (F/cm).

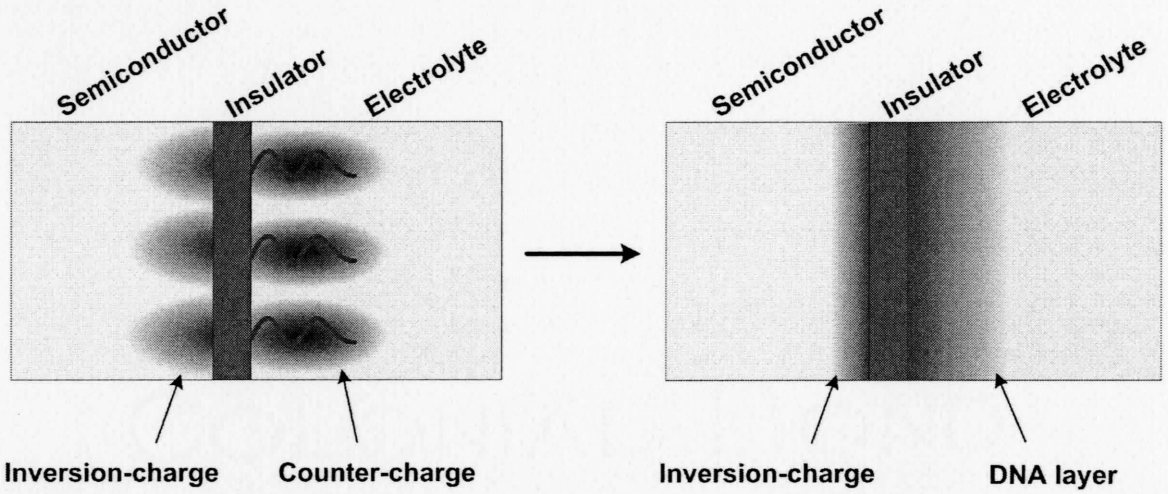

Figure 2.15 Comparison between the 2-D (left) and 1-D (right) versions of the electrostatic modeling of the BioFET

Inspecting equation 2.35, we can realize why it is not easily possible to isolate the contribution of the DNA charge as we did with the insulator charges, and reflect them to some equivalent charge at a reference location (such as the electrolyte-insulator interface). Equation 2.35 is a nonlinear second-order differential equation, and as such, the principle of superposition does not apply. We must therefore solve this equation numerically, given sufficient boundary conditions, to obtain the total charge and potential profile within this area. Figure 2.16 shows the positioning of all the different charge contributions in the BioFET.

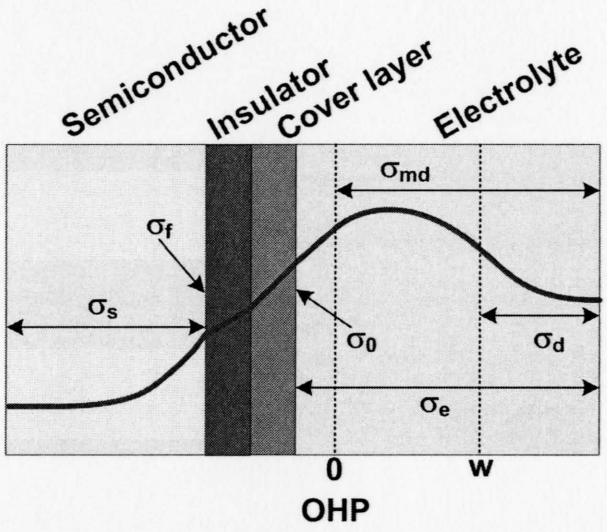

Figure 2.16 Illustration of different charge contributions in the BioFET

2.3.2.2 Modeling the Ionic Presence in the Solution

Although the ionic presence in the DNA membrane area was accounted for by equation 2.35, one cannot arbitrarily assume that no ions exist outside this region. In fact, the entire DNA membrane might be inside the Gouy-Chapman-Stern diffuse region, leaving a "tail" of the diffuse charge outside the DNA membrane region, as shown in Figure 2.16. Thus, it is important to include this charge contribution as part of the total charge on the electrolyte side. Moreover, it will provide a more realistic boundary condition to solve equation 2.35, as opposed to arbitrarily setting the boundary conditions to zero.

The potential equation for this DNA-free area of the BioFET is the PB equation:

$$\frac{d^2\psi(x)}{dx^2} = \frac{2qzn_0}{\varepsilon_e}\sinh\left(z\beta\psi(x)\right), \qquad 2.36$$

where ε_e is the electrolyte's permittivity in absence of DNA molecules. This region has a vanishing electric field and potential as we go deeper into the electrolyte, while its potential at the DNA membrane region is the unknown variable ψ_d. Given the expression for the stored charge in the Gouy-Chapman model (equation 2.12), we can conclude:

$$\sigma_d = -\sqrt{8kT\varepsilon_e n_0}\sinh\left(\frac{z\beta\psi_d}{2}\right), \tag{2.37}$$

where σ_d and ψ_d are the total integrated charge density per unit area, and the potential with respect to the bulk, for this region of the electrolyte, respectively. Equation 2.37 gives boundary conditions that enable the integration of equation 2.35. These boundary conditions come about as a result of the physical requirements of continuity of the electric flux density, and potential. Translating this into mathematics, we have at this interface (Figure 2.16) [37]:

$$\begin{aligned} &\psi(w) = \psi_d \\ &\varepsilon_m \left.\frac{d\psi}{dx}\right|_{w-} = \varepsilon_e \left.\frac{d\psi}{dx}\right|_{w+} \\ &\left.\frac{d\psi}{dx}\right|_{w-} = \frac{\sigma_d}{\varepsilon_m} \end{aligned} \tag{2.38}$$

Knowing the initial conditions of the potential and its derivative at this interface point, we can integrate equation 2.35 throughout the membrane, arriving at a value for the potential ψ_m and its derivative at the edge of the DNA membrane layer, which is the OHP for the electrolyte-insulator interface. This derivative is related by Gauss's law to the total charge from the bulk electrolyte to the stern layer, including the previously calculated σ_d. In keeping with the convention of [37], this charge will be denoted σ_{md}. Thus:

$$\left.\frac{d\psi}{dx}\right|_{0+} = \frac{\sigma_{md}}{\varepsilon_m}. \tag{2.39}$$

In this way, the entire DNA and double layer charge can be calculated. There remains a final potential drop which occurs across the Stern layer, from the OHP to the electrolyte-insulator surface. Since no ionic charges are assumed to be present in this region, the potential drop is linear and is given by:

$$\psi_{stern} = -\frac{\sigma_{md}}{C_{stern}}, \tag{2.40}$$

where C_{stern} is the capacitance of the Stern layer (F/cm^2), assuming no bias dependence, meaning that no specific adsorption of ions takes place. We now have expressions for

potential drops that add up to the total potential drop in the electrolyte. However, a final charge accumulation at the surface due to surface protonation and deprotonation influences the total charge in the semiconductor and is discussed next.

2.3.2.3 Modeling the Insulator Surface Adsorption

The surface of the insulator contains surface states that can capture and release hydrogen ions, in addition to other ions. Since hydrogen ions (protons) are very small in size, they can approach the surface of the insulator and get adsorbed easily. In this model, only reaction with protons will be considered. In particular, the following protonation-deprotonation reactions will be considered [37], [41]:

$$\begin{aligned} -SiOH_2^+ &\overset{K_a}{\leftrightarrow} -SiOH^+ + H^+ \\ -SiOH &\overset{K_b}{\leftrightarrow} -SiO^- + H^+ \end{aligned} \quad . \qquad 2.41$$

This amphoteric behavior (acidic or basic) is illustrated in Figure 2.17. At equilibrium, the molar concentration of the species involved in the reactions stay constant, and electrochemical equilibrium is established for both equations [38]. If we denote the electrochemical potential of substance X by $\tilde{\mu}_X$, the chemical potential by μ_X, and the standard chemical potential by μ_X^o, we have at equilibrium [30]:

$$\begin{aligned} \tilde{\mu}_{-SiOH_2^+} &= \tilde{\mu}_{-SiOH} + \tilde{\mu}_{H^+} \\ \tilde{\mu}_{-SiOH} &= \tilde{\mu}_{-SiO^-} + \tilde{\mu}_{H^+} \end{aligned} \quad . \qquad 2.42$$

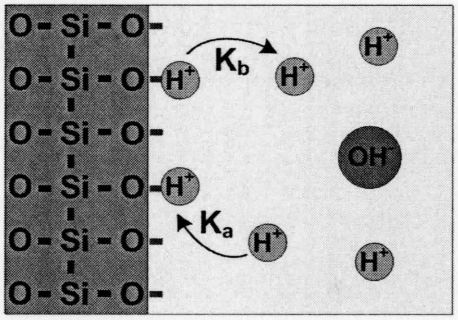

Figure 2.17 Amphoteric behaviors of insulator-electrolyte surfaces

Now, splitting the electrochemical values into electrostatic and chemical contributions, and using the Nernst equation (equation 2.24), we have [38]:

$$\begin{aligned}\mu^{o}_{-SiOH_2^+} + kT\ln\left(\frac{[-SiOH_2^+]}{[-SiOH]}\right) + q\psi_0 &= \mu^{o}_{-SiOH} + \mu^{o}_{-H^+} + kT\ln\left([H^+]\right) + q\psi_0 \\ \mu^{o}_{-SiOH} + kT\ln\left(\frac{[-SiOH]}{[-SiO^-]}\right) &= \mu^{o}_{-SiO^-} - q\psi_0 + \mu^{o}_{-H^+} + kT\ln\left([H^+]\right) + q\psi_0\end{aligned}, \qquad 2.43$$

where the activities of the ions were taken to be their local concentration at the interface. Now, by definition,

$$\begin{aligned}K_a &= e^{\frac{\mu^{o}_{-SiOH_2^+} - \mu^{o}_{-SiOH} - \mu^{o}_{-H^+}}{kT}} \\ K_b &= e^{\frac{\mu^{o}_{-SiOH} - \mu^{o}_{-SiO^-} - \mu^{o}_{-H^+}}{kT}}\end{aligned}. \qquad 2.44$$

Equation 2.43 can now be re-written as:

$$\begin{aligned}K_a &= \frac{[-SiOH][H^+]}{[-SiOH_2^+]} \\ K_b &= \frac{[-SiO^-][H^+]}{[-SiOH]}\end{aligned}. \qquad 2.45$$

Substituting the surface concentration of hydrogen ions with its potential-dependent equation given by equation 2.19, we get:

$$\begin{aligned}\frac{K_a}{[H^+]_0}e^{\beta\psi_0} &= \frac{[-SiOH]}{[-SiOH_2^+]} \\ \frac{K_b}{[H^+]_0}e^{\beta\psi_0} &= \frac{[-SiO^-]}{[-SiOH]}\end{aligned}. \qquad 2.46$$

The total count of reaction sites is constant per surface:

$$[-SiO^-] + [-SiOH] + [-SiOH_2^+] = N_s, \qquad 2.47$$

where N_s is the concentration of the reaction sites on the surface (cm^{-2}). The final equation defines the charge density on the insulator surface:

$$\sigma_0 = q\left([-SiOH_2^+] - [-SiO^-]\right), \qquad 2.48$$

where σ_0 is the surface charge density (C/cm^2). Equations 2.46 and 2.47 constitute a system of linear equations in variables [*-SiOH*], [*-SiO$^-$*] and [$SiOH_2^+$]. These can be simultaneously solved for the charged variables. The results, plugged into equation 2.48, would result in the following expression [37]:

$$\sigma_0 = qN_s\left(\frac{A-B}{1+A+B}\right), \tag{2.49}$$

where:

$$A = \frac{[H^+]_0}{K_a}e^{-\beta\psi_0}$$
$$B = \frac{K_b}{[H^+]_0}e^{\beta\psi_0} \tag{2.50}$$

Equation 2.49 relates the total adsorbed charge density on the insulator surface to the surface potential drop accumulated within the electrolyte. This is the final equation needed to completely characterize the BioFET structure. It shows how the proton concentration (solution pH) can affect the charge density. Figure 2.18 shows sample charge-potential curves for several different pH values, calculated using equations 2.49 and 2.50.

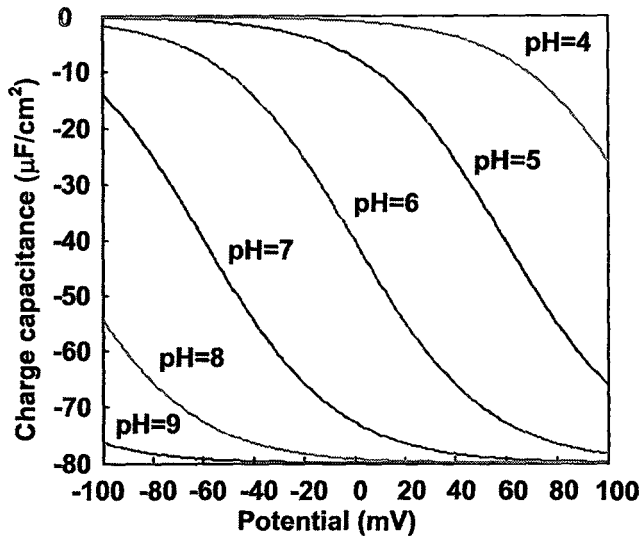

Figure 2.18 Charge-potential curves for proton adsorption on SiO_2

2.3.2.4 Solution Method

The equations that need to be solved are equations 2.28, 2.33, and 2.34. For a given bias and device parameters of electrolyte concentration, pH, DNA probe density, equivalent insulator thickness, substrate doping density and different material work functions and permittivities, these equations provide a system of equations in four unknowns: σ_s, σ_e, ψ_s, and ψ_0 One more equation is required that relates σ_e to ψ_0. However, this equation cannot be given as a single closed form expression. Instead, we have to start with a Gouy-Chapman diffuse potential ψ_d, and then we calculate σ_d using equation 2.49. We find the gradient of this potential at the DNA membrane edge using equation 2.38, and we use the potential and its derivative as initial conditions to solve equation 2.35. The solution will give the total diffuse charge σ_{md} and potential ψ_m. These two values can be used to calculate the potential drop across the Stern layer, using equation 2.40. Then, using the following equation:

$$\psi_0 = \psi_m + \psi_{Stern}, \tag{2.51}$$

we can arrive at the electrolyte surface potential. We finally use equation 2.49 to calculate the surface charge of the adsorption, which is related to the total electrolyte charge by the following charge balance equation:

$$\sigma_e = \sigma_0 + \sigma_{md}. \tag{2.52}$$

The procedure shown above can be seen as a single continuous equation that relates ψ_0 to σ_e. The only difference is that we cannot explicitly start from one of these variables and reach the other. These equations can be seen as parametric equations that relate these two variables together through the parameter ψ_d. We shall represent this process by the following expression, treated hereinafter as an equation:

$$\psi_d \rightarrow \psi_0, \sigma_e. \tag{2.53}$$

To solve the BioFET structure, we need to solve the four nonlinear coupled equations self-consistently. These are equations 2.28, 2.33, 2.34, and 2.53. We can exploit the apparent continuity of these equations and speculate that the variation in the dependent

variables σ_e, σ_s, ψ_s, ψ_d, and ψ_0 are continuous in V_{GB}. This continuity allows us to employ a bisection scheme with successive approximation, to achieve the self-consistent solution. Theoretically, one can employ the bisection scheme for any of the dependent variables. However, it is convenient here to use the semiconductor surface potential as the variable of bisection. The bisection scheme would proceed as follows:

1. Start with a reasonable value for ψ_d. Values in the interval [-1, 1] volts are typical for solutions with concentrations of a few mM.
2. Using equation 2.53, determine the values of ψ_0 and σ_e.
3. Using the charge balance equation 2.34, calculate the corresponding σ_s.
4. Using the potential balance equation 2.28, calculate the corresponding ψ_s.
5. Using the calculated ψ_s, determine the expected σ_s from equation 2.33.
6. Compare the value of σ_s calculated in step (5) with that obtained from step (3). The difference is used to refine one edge of the interval in step (1) with the value chosen for ψ_d, such that the solution remains within the smaller interval.
7. The iteration is repeated until the interval is small enough, with the final value of ψ_d taken as the midpoint of this interval.

A MATLAB simulation program was written to perform the iteration procedure shown above. Figure 2.19 shows potential profiles for the DNA membrane obtained by integrating equation 2.35. Figure 2.20 shows a complete simulated potential profile for a BioFET. The modification of the potential profile due to the existence of the charged DNA molecules can be clearly seen. More explanation of these curves will be provided towards the end of this chapter.

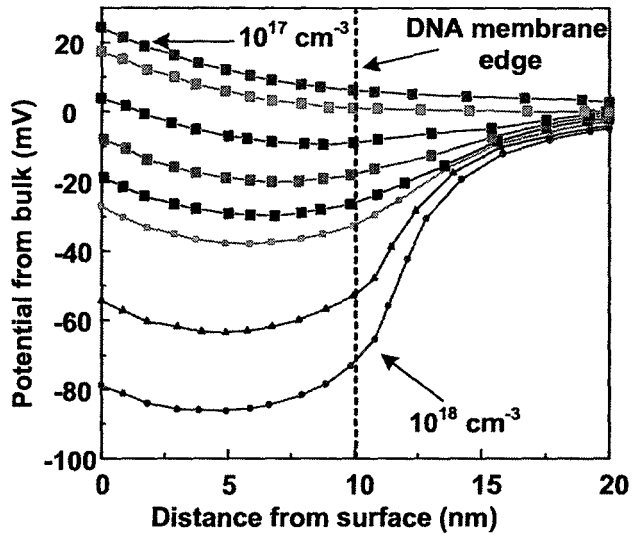

Figure 2.19 Sample solution curves for the charge-perturbed PB equation

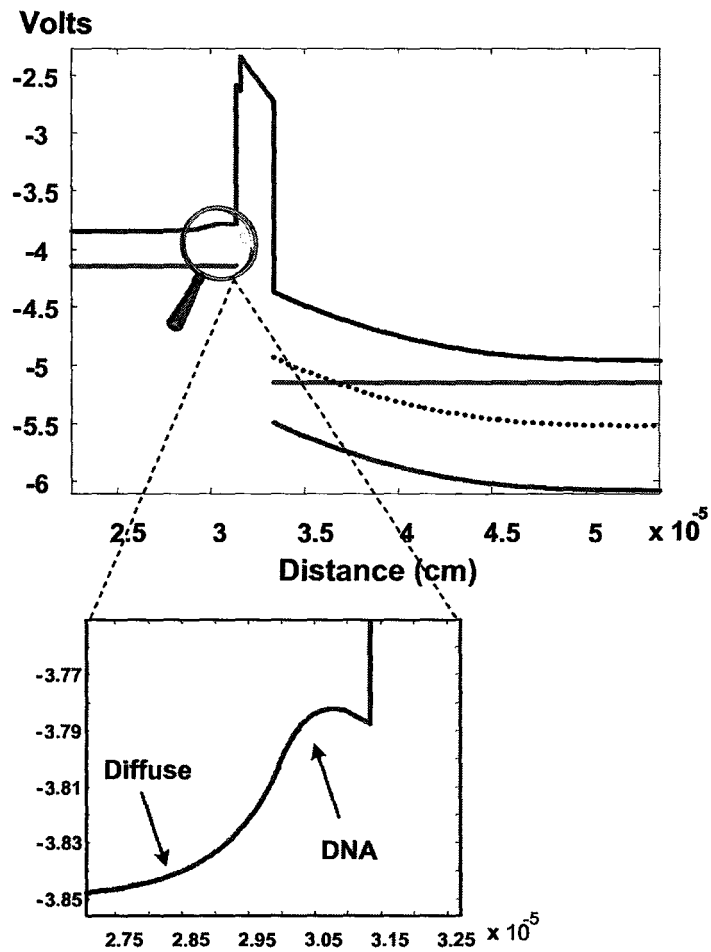

Figure 2.20 Simulated BioFET structure, showing the profile of the DNA layer

2.3.3 Current Equations

The previous treatment of the BioFET only considered the BioFET capacitor structure, without any drain or source contacts. This allows a 1-D approximation to the electrostatic phenomena to be made for accurate results. However, once the drain and source are introduced, the immediate contacts of the drain-channel and source-channel become very hard to describe, particularly as a lateral built-in potential arises from carrier diffusion between the source or drain and channel. However, in areas of the channel that are far away from the effects of introducing the drain and source, such as the midpoint of the channel, the 1-D approximation is still valid.

Once a drain-source bias is introduced, the situation changes dramatically. If the channel has enough surface potential (band bending) such that the potential barriers at the source-channel and drain-channel interface are significantly lowered, current will begin to flow. Depending on whether the FET structure is P-type or N-type, current will flow from the source to drain, or vice versa. The main problem is that in this non-equilibrium case, equations 2.30, 2.32, and 2.33 are not valid. This will change the charge carrier distribution along the channel, affecting the mirrored charge in the electrolyte as well.

In order to stay within the boundaries of a one-dimensional model, an approximation to the exact physical model is often employed in physical studies of MOSFET transistors [36]. This approximation, called the charge-sheet model, is based on the following approximations:

1. The device is in inversion: The surface must have been inverted, meaning that $\psi_s \geq \phi_F$ for a P-type substrate and $\psi_s \leq \phi_F$ for an N-type substrate.
2. Minority carrier contribution within the entire device is neglected: The implications of this assumption are that leakage currents at the body-source and body-drain contacts, when the corresponding junctions are in reverse bias, are neglected and they do not cause non-equilibrium.
3. The conducting current, due to majority carriers, happens only within an infinitesimally thin layer of inversion charge at the surface of the channel: This

approximation allows us to arrive at a closed form expression for the inversion charge in a MOSFET, by assuming that the potential drop within the semiconductor is solely due to ionized impurity atoms.

By applying the previous assumptions, the depletion charge density per unit area in the channel of the semiconductor with no source or drain bias is given by [36]:

$$\sigma_b = \mp\sqrt{2q\varepsilon N}\sqrt{\pm\psi_s}\,. \qquad 2.54$$

In equation 2.54, σ_b is the depletion charge density per unit area (C/cm^2). The upper set of signs is used for P-type semiconductor substrate (NMOS), while the lower set is used for N-type (PMOS). If we denote the inversion charge density by σ_i, then equation 2.28 can be re-written as:

$$V_{GB} = \chi_{sol} - \chi_{Si} - \frac{u_{sol}}{q} + \frac{u_s}{q} - \psi_0 - \frac{\left(\sigma_i + \sigma_b + \sigma_f\right)}{C_{eff}} + \psi_s\,. \qquad 2.55$$

After rearranging the values, we get:

$$\sigma_i = -C_{eff}\left(V_{GB} - \left(\chi_{sol} - \chi_{Si} - \frac{u_{sol}}{q} + \frac{u_s}{q} - \frac{\sigma_f}{C_{eff}} - \psi_0 + \psi_s - \frac{\sigma_b}{C_{eff}}\right)\right). \qquad 2.56$$

The constant contributions in equation 2.56 can be lumped into what used to be known as the flatband voltage, defined as the voltage which would annihilate the depletion and inversion charges, as well as the semiconductor surface potential. In the case of the BioFET, this is not the case [39], as the term ψ_0 also contributes to the flatband potential. What is more interesting is that this potential varies with the bias. Thus, in the case of a BioFET, one cannot assume a constant flatband potential. Subsequently, the threshold voltage of the BioFET would depend on the bias of the reference electrode. Equation 2.56 can be re-written as [39]:

$$\sigma_i = -C_{eff}\left(V_{GB} - V_{FBC} + \psi_0 - \psi_s + \frac{\mp\sqrt{2q\varepsilon N}}{C_{eff}}\sqrt{\pm\psi_s}\right). \qquad 2.57$$

Equation 2.57 relates the inversion charge to the surface potential. The surface potential is expected to vary along the lateral dimension of the charge-sheet area in the FET. Both

diffusion and drift contributions of the current must be considered. These two components are given by the following equation [36]:

$$I_{total} = I_{diff}(x) + I_{drift}(x) = -\frac{\mu(x)W}{\beta}\frac{d\sigma_i(x)}{dx} \pm \mu(x)W\sigma_i(x)\frac{d\psi_s(x)}{dx}. \qquad 2.58$$

In equation 2.58, W is the width of the BioFET's channel (cm), and μ is the mobility of the inversion charge carriers ($cm^2/V.s$). This equation is general, in the sense that the carrier mobility is taken to be a function of position. Although spatial variation of mobility can be an indication of anisotropy or variation in the structure of the semiconductor crystal, the intent here is to parameterize the mobility's dependence on potential through the potential's spatial variation with the lateral position along the channel, using the position variable x as a parameter. If this dependence is weak, then we can ignore it, to a first degree approximation. Such an approximation will neglect velocity saturation effects. Now, all that is needed is the variation of the inversion density with position, which we don't have. Instead, what can be done is to transfer the differential variable from position to potential by integrating the constant current from source (x=0) to drain (x=L) as follows:

$$\begin{aligned} \mp\int_0^L I_{total}dx &= \mp\mu W\left(-\frac{1}{\beta}\frac{d\sigma_i(x)}{dx} \pm \sigma_i(x)\frac{d\psi_s(x)}{dx}\right)dx \\ I_D &= \frac{\mu W}{L}\left(\pm\frac{1}{\beta}\int_{\sigma_i(\psi_{s0})}^{\sigma_i(\psi_{sL})} d\sigma_i(\psi_s) - \int_{\psi_{s0}}^{\psi_{sL}} \sigma_i(\psi_s)d\psi_s\right) \end{aligned} \qquad 2.59$$

The sign convention in this equation is chosen to maintain a positive current direction for both PMOS and NMOS devices, even though the direction of integration is always from the source to the drain. With equation 2.57 and 2.59, an expression for the semiconductor's current can be derived [39]:

$$I_{total}=\frac{\mu WC_{eff}}{L}\left(\begin{array}{l}\mp\frac{1}{\beta}C_{eff}\left(\psi_{0L}-\psi_{00}-\psi_{sL}+\psi_{s0}\mp\frac{\sqrt{2q\varepsilon N}}{C_{eff}}\left(\sqrt{\pm\psi_{sL}}-\sqrt{\pm\psi_{s0}}\right)\right)\\+\left(V_{GB}-V_{FBC}\right)\left(\psi_{sL}-\psi_{s0}\right)+\int_{\psi_{s0}}^{\psi_{sL}}\psi_0(\psi_s)d\psi_s-\frac{1}{2}\left(\psi_{sL}^2-\psi_{s0}^2\right)\\-\frac{2}{3}\frac{\sqrt{2q\varepsilon N}}{C_{eff}}\left(\left(\pm\psi_{sL}\right)^{3/2}-\left(\pm\psi_{s0}\right)^{3/2}\right)\end{array}\right),\qquad 2.60$$

where, as in the previous equations, the upper signs are taken for an NMOS device (P-substrate), and the lower signs are for PMOS-type BioFETs. Equation 2.60 allows us to calculate the current if we know the semiconductor's surface potential at the source and drain ends. Thus, we need to solve the BioFET structure twice, once at the source and once at the drain [36], [39].

In non-equilibrium conditions, equation 2.33 must be modified before the iterations can be taken to solve for the BioFET's current. If only the surface potential is considered, then a quasi-Fermi level concept can be considered, in which the bias of the source (or drain), is seen to affect the channel surface potential at that end by an amount equal to the bias [36]. A potential diagram illustrating this concept is shown in Figure 2.21, in which it can be clearly seen that the source (drain) potential with respect to the body causes the Fermi level to bend, leading to non-equilibrium. It can be seen how this bias aids the Fermi potential in its effect on the band-bending of the channel. As the non-equilibrium situation manifests, current will have to flow throughout the structure, unless a perfect insulator is blocking the passage of current. The current that is caused by this bending of Fermi levels is the reverse-bias saturation current of the source (drain) to channel junction, which acts like a diode. Figure 2.21 shows that the surface potential now contains a term that comes from the source (drain) to body bias. With this, equation 2.33 can be re-written to be as follows:

$$\sigma_s=\mathrm{sgn}(-\psi_s)\sqrt{2kT\varepsilon_s n_i}\left(e^{\pm\beta\phi_F}\left(e^{\mp\beta\psi_s}\pm\beta\psi_s-1\right)+e^{\mp\beta\phi_F}\left(e^{\pm\beta(\psi_s-V_{CB})}\mp\beta\psi_s-e^{\mp\beta V_{CB}}\right)\right)^{1/2},\qquad 2.61$$

where V_{CB} is the potential at the closest terminal (drain or source). Equation 2.61 must be used instead of equation 2.33 when performing the iterations for the BioFET solution.

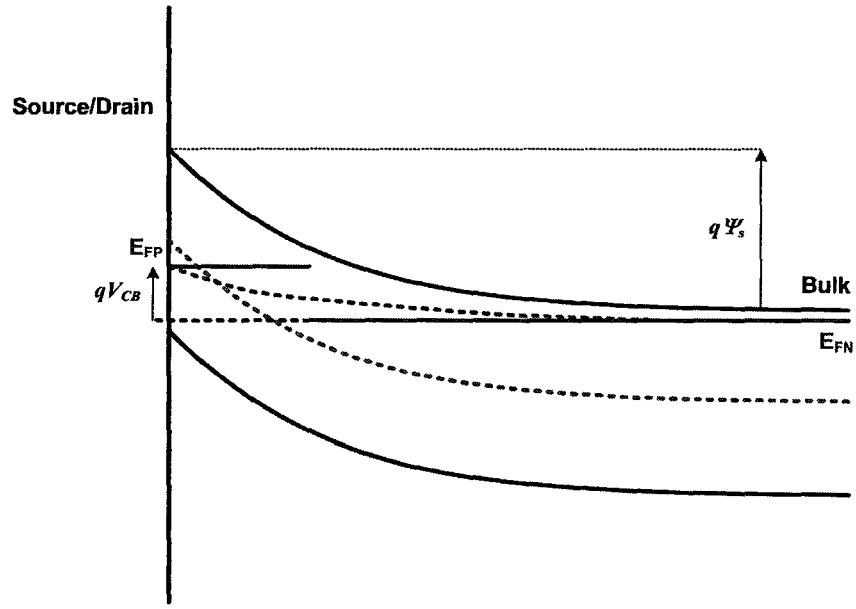

Figure 2.21 Semiconductor potential diagram under source (drain) bias [36]

2.4 Simulator Design

A simulator for the response of the BioFET was written in MATLAB, which conducts the iterative algorithm to arrive at the self-consistent solution of the BioFET's structure. Figure 2.22 shows the flow chart used in carrying out the simulation. Integration of equation 2.35 was done using a Runge-Kutta 4 algorithm. Before this algorithm can be used, the differential equation must be reduced in order. For this, the equation was rewritten as a system of first order equations:

$$\begin{aligned} \frac{d\psi(x)}{dx} &= \psi'(x) = F_1(\psi,\psi') \\ \frac{d\psi'(x)}{dx} &= \frac{2qzn_0}{\varepsilon_m}\sinh\left(z\beta\psi(x)\right) - \frac{qN_m}{\varepsilon_m} = F_2(\psi,\psi') \end{aligned} \qquad 2.62$$

The Runge-Kutta 4 algorithm finds an incremental solution vector from an initial vector using an averaged slope value by successive approximation. The algorithm is given in the following equations, using a step size of h:

$$
\begin{aligned}
&\begin{pmatrix}\psi\\ \psi'\end{pmatrix}' = \begin{pmatrix}F_1(\psi,\psi')\\ F_2(\psi,\psi')\end{pmatrix}\\
&K_1 = h\begin{pmatrix}F_1(\psi_0,\psi_0')\\ F_2(\psi_0,\psi_0')\end{pmatrix}\\
&K_2 = h\begin{pmatrix}F_1(\psi_0+\frac{K_1(1)}{2},\psi_0'+\frac{K_1(2)}{2})\\ F_1(\psi_0+\frac{K_1(1)}{2},\psi_0'+\frac{K_1(2)}{2})\end{pmatrix}\\
&K_3 = h\begin{pmatrix}F_1(\psi_0+\frac{K_2(1)}{2},\psi_0'+\frac{K_2(2)}{2})\\ F_1(\psi_0+\frac{K_2(1)}{2},\psi_0'+\frac{K_2(2)}{2})\end{pmatrix}\\
&K_4 = h\begin{pmatrix}F_1(\psi_0+K_3(1),\psi_0'+K_3(2))\\ F_1(\psi_0+K_3(1),\psi_0'+K_3(2))\end{pmatrix}\\
&\begin{pmatrix}\psi_h\\ \psi_h'\end{pmatrix} = \begin{pmatrix}\psi_0\\ \psi_0'\end{pmatrix} + \frac{1}{6}\left(K_1+2K_2+2K_3+K_4\right).
\end{aligned}
\qquad 2.63
$$

One of the problems with the system that needs to be solved is that it is very stiff, which makes the solution very sensitive to the selected step size. In addition, since this is a serial integration, it will take the most amount of execution time per iteration. Throughout the iteration process, many integrations will be performed in which the potential profile in the membrane will rise without bounds. This is because the initial conditions were incorrect. Throughout the iterations, the initial conditions get more and more refined. However, it would be useless to continue the integration once the potential reaches above a certain extreme value (positive or negative). Therefore, to speed up execution time, it is important that we stop the integration and restart a new iteration of the solver with a modified bisection interval, otherwise significant amount of simulation time will be spent on useless iterations.

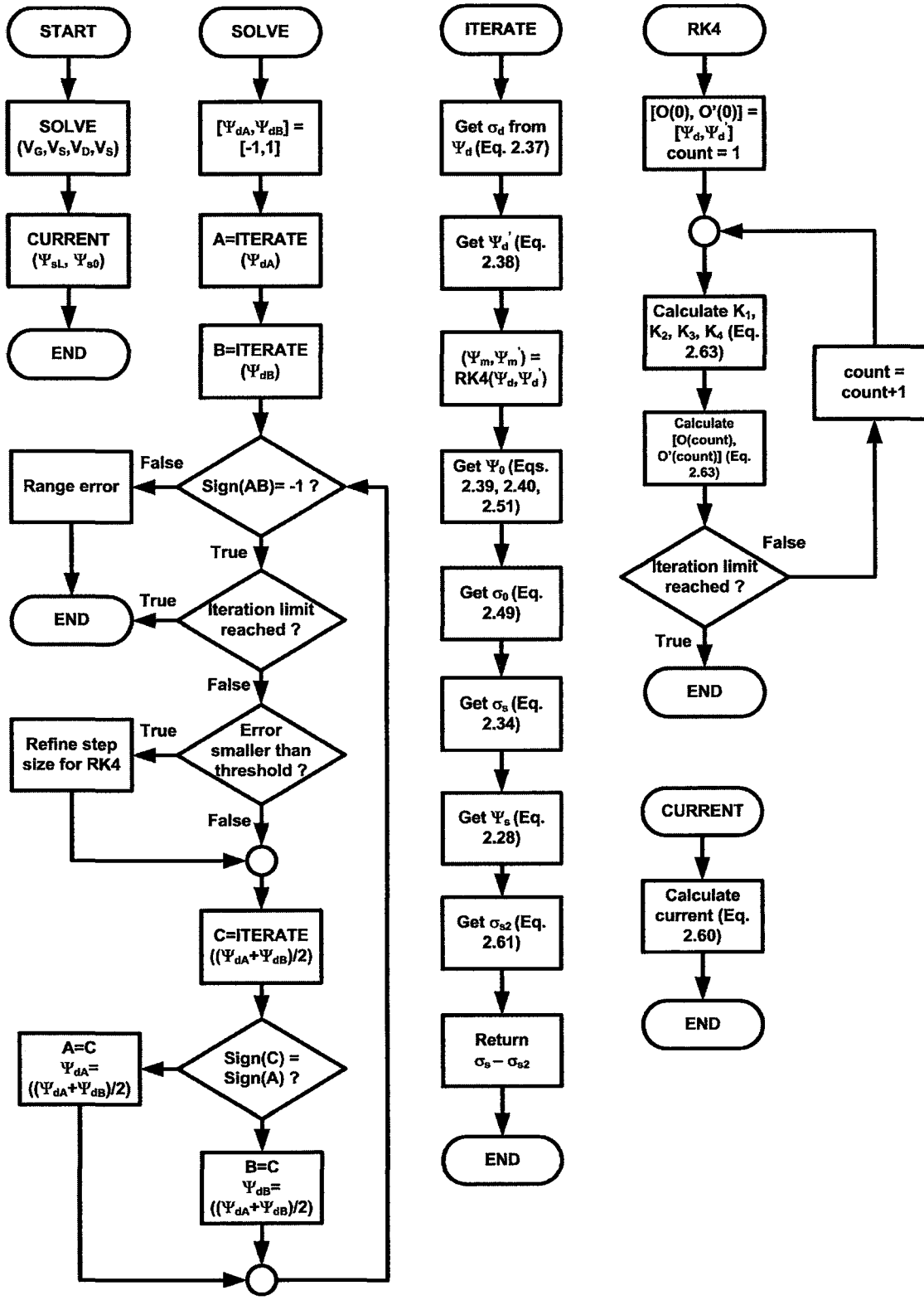

Figure 2.22 Simplified flowchart of the BioFET solver algorithm

Another problem that must be realized is that a self-consistent solution will always be reached for any value of step size. However, if the step size is too large, this solution will not be the correct one. It is therefore important to choose a small step size. However, a small step size at the very first iterations would again cost a lot of wasted simulation time. It is therefore desirable to resort to some "adaptive" method of mesh refinement, wherein the step size is reduced as the self-consistent solution is approached. A three-step adaptive algorithm was included in the simulator to address this inaccuracy. The switch between step sizes was accomplished by comparing the error in each iteration with carefully selected thresholds. It is important to note that if the coarse step size is not refined in time, the inaccurate iteration solutions may cause the newly refined solution interval to lose the solution. After this has happened, step refinement will not help restore the solution-containing interval. The simulation is terminated when the refined interval size is within a pre-defined threshold such that the error is tolerable.

2.5 Conclusion

In this chapter, a basic one-dimensional model of the BioFET was presented. The model is based on electrostatics and statistical mechanics, relating the total charge density in the electrolyte to that in the semiconductor. Effects of ionic charge screening and proton adsorption were taken into account to arrive at a quantitative measure for the sensitivity of the BioFET. This model can be used to investigate the optimum conditions for sensitivity of a BioFET within the limits of the model's validity. The next chapter presents simulation results of this model and attempts to investigate the effects of varying several parameters in the BioFET's structure on its sensitivity.

Chapter 3

SENSITIVITY OF BIOFETS

3.1 Introduction

In chapter two, complete physical modeling of the BioFET was conducted. This model captures the essential sensitivity parameters that affect the performance of the BioFET. In this chapter, the simulator will be used to investigate the effects of varying different device parameters on the sensitivity of the BioFET. In particular, the effects of certain device parameters such as pH concentration, ionic strength and probe densities will be analyzed. Optimum device biasing conditions and temperature effects will be introduced, and some effects that are not addressed within the model described in chapter 2 will be presented.

3.2 Evaluation of the BioFET Current

In the previous chapter, an expression was derived using the charge-sheet model of MOSFETs to relate the semiconductor surface potential and the BioFET's bias potentials to the drain current. Unlike regular MOSFETs, in order to evaluate the expression for the current of the BioFET (equation 2.60), we must evaluate the integral in the equation, which requires an expression that relates the electrolyte's surface potential to that of the semiconductor. Inspecting the model's equations, it seems that we cannot arrive at an exact analytic expression that relates these two together. However, it is still possible to use the MATLAB simulator to investigate the type of dependence between these two variables. Figure 3.1 shows simulated results of the variation of Ψ_0 with Ψ_s as the quasi-Fermi potential is varied (by virtue of V_{CB}), for several different ionic concentrations. It can be noticed that the monotonic, almost linear relationship allows us to evaluate the

integral in equation 2.60 without having an explicit relationship between the two variables. Thus, we can replace the integral with an average value of the numerically calculated electrolyte surface potentials. Therefore, equation 2.60 can be re-written as:

$$I_{total} = \frac{\mu W C_{eff}}{L}\left(\begin{array}{l} \mp\frac{1}{\beta}C_{eff}\left(\psi_{0L}-\psi_{00}-\psi_{sL}+\psi_{s0}\mp\frac{\sqrt{2q\varepsilon N}}{C_{eff}}\left(\sqrt{\pm\psi_{sL}}-\sqrt{\pm\psi_{s0}}\right)\right) \\ +\left(V_{GB}-V_{FBC}\right)\left(\psi_{sL}-\psi_{s0}\right)+\frac{1}{2}\left(\psi_{0L}+\psi_{00}\right)-\frac{1}{2}\left(\psi_{sL}^2-\psi_{s0}^2\right) \\ -\frac{2}{3}\frac{\sqrt{2q\varepsilon N}}{C_{eff}}\left(\left(\pm\psi_{sL}\right)^{3/2}-\left(\pm\psi_{s0}\right)^{3/2}\right) \end{array}\right), \qquad 3.1$$

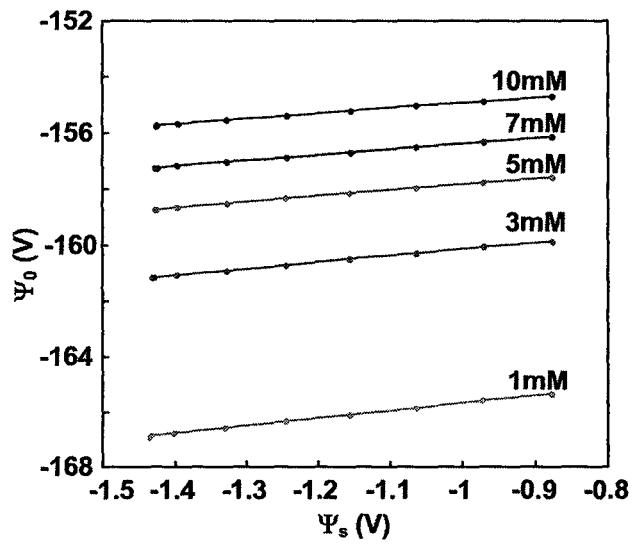

Figure 3.1 Simulated inter-dependence of semiconductor's and electrolyte's surface potentials

With equation 3.1, we can investigate the current-voltage characteristics of the BioFET. The current obtained from the BioFET is calculated as the difference in the value of the current before and after DNA target hybridization to the probe molecules. Figure 3.2 shows the expected signal obtained due to complete DNA hybridization for a P-type BioFET with aspect ratio of 5:1. The parameters used in obtaining this curve are given in Table 3.1.

Table 3.1 Parameters used for the simulation of Figure 3.2

Parameter	Units	Value
Solution pH	-	7.0
Ionic concentration	Mol/Liter (Molar)	0.001
Amphoteric site density	cm^{-2}	5×10^{14}
First deprotonation constant (pKa)	-	-2
Second deprotonation constant (pKb)	-	6
DNA strand length	nm	10
Electrolyte dielectric constant	-	78.4
Equivalent insulator thickness	nm	17.8
Equivalent cover layer thickness	nm	2.5
Channel width	μm	25
Channel length	μm	5
Hole mobility	$cm^2/V.s$	160
Fixed charge density	cm^{-2}	0
Electrode potential ($-u_{sol}/q$)	V	0.3
Stern capacitance	$\mu F/cm^2$	20
Biases (V_G, V_S, V_D, V_B)	V	(3,5,[4.7,4.5,4],5)
Calculated threshold voltage	V	-1.13

Figure 3.2 shows that for relatively sparse-located DNA strands, wherein every two adjacent DNA strands are approximately 54 nm apart, which is enough space to fit 27 more DNA strands, enough incremental inversion charge arises due to hybridization that will allow current changes in the order of microamperes. In all the simulations in this chapter, the BioFET's response is taken as the shift in the drain current due to complete hybridization of target ssDNA molecules to tethered probes, thereby doubling the amount of fixed DNA charge in the membrane. This quantity is referred to as the hybridization current or the BioFET current.

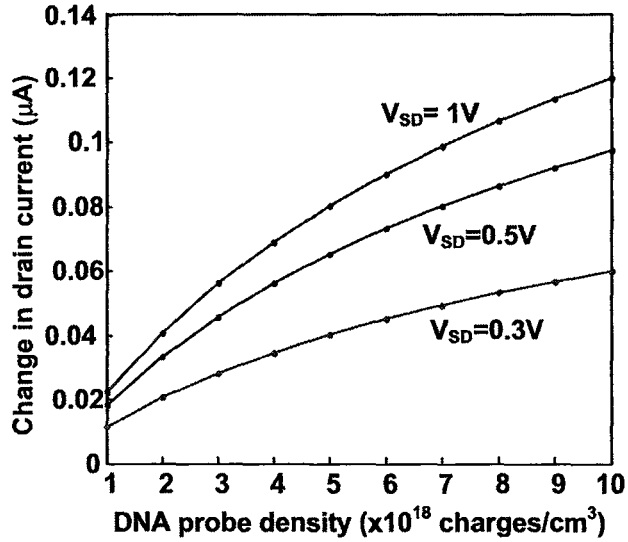

Figure 3.2 Simulated response of the BioFET to DNA hybridization

It is informative to compare the result obtained using this model with what would be obtained using the more naïve approach of reflecting the entire DNA charge to the electrolyte surface, thereby eliminating the counter-ion screening effect. In order to accomplish this, the regular analytic model of the linear mode MOSFET will be used, to correspond with the operating parameters of Table 3.1. If the DNA charge is reflected to the insulator surface, its effect is only to change the threshold voltage. The change in this threshold voltage would be as follows:

$$\Delta V_{TH} = \frac{-\Delta\sigma_{DNA}}{C_{eff}} = \frac{-L_{DNA}\Delta\rho_{DNA}}{C_{eff}}, \qquad 3.2$$

where L_{DNA} is the DNA's strand length (cm). For the values given in Table 3.1, this threshold voltage change for DNA probe density of -1×10^{18}cm^{-3} would be approximately 0.94 volts. The corresponding current change, for the case of V_{SD} = 0.3V, can be calculated from:

$$I_D = K\left((V_{SG}+V_{TH})V_{SD} - \frac{1}{2}V_{SD}^2\right)$$
$$\Delta I_D = KV_{SD}\Delta V_{TH} = \frac{\mu C_{eff} W}{L} V_{SD}\Delta V_{TH} = 9.6\mu A \qquad 3.3$$

The value obtained by equation 3.3 overestimates the shift in the current, compared to that of the simulated model (around 10 nA), by three orders of magnitude. This severe variation illustrates the need to consider the counter-ion charges that screen the DNA charge.

Figure 3.3 compares experimentally obtained I_D-V_{REF} curves of a BioFET transistor [28] with immobilized and hybridized DNA, to those obtained with the simulator for a BioFET with similar parameters. The results show the ability of the model presented to estimate the response of the BioFET to a given immobilized DNA charge concentration. It is important to note that equal amounts of excess charge added to the DNA need not shift the threshold voltage (or equivalently, change the drain current) by similar amounts, as is clearly seen from Figure 3.3. This is due to the severe nonlinearity of the equations that describe the BioFET. Under certain operating conditions, one might be able to approximate the response of the BioFET with simpler equations. This will be discussed in detail later in this chapter.

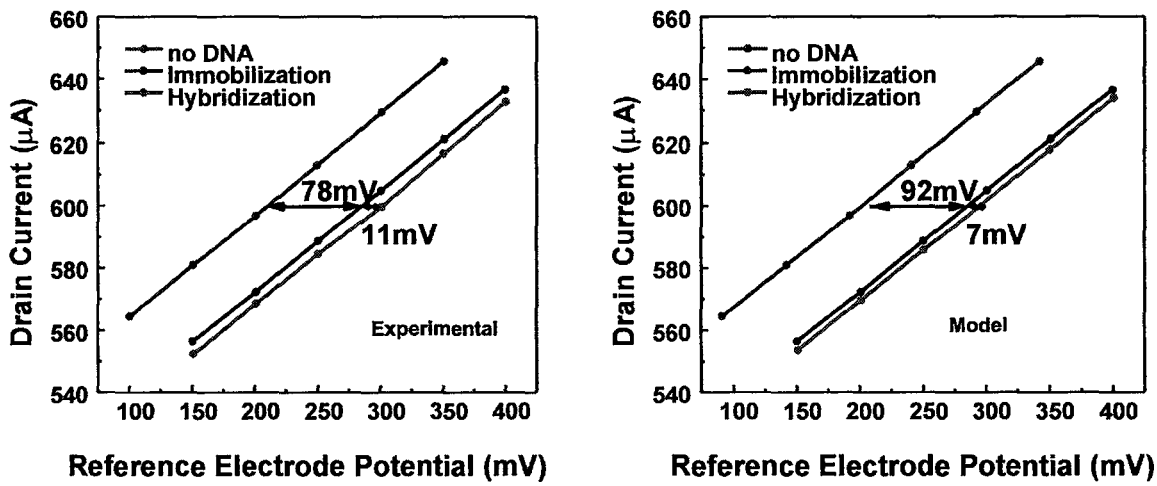

Figure 3.3 Comparison between published results of [28] and model simulations

3.3 The Effect of the Solution's pH Value

The amphoteric behavior of the insulator can severely affect the performance of the BioFET. Adsorbed ions can aid in screening the electric field change due to DNA hybridization. Figure 3.4a shows simulated BioFET response curves for different pH

values of the solution and five different DNA membrane probe densities. From the figure, it can be seen that the strength of the current change (the sensor's signal) is clearly a function of the pH value of the solution. This pH dependence comes about as a result of the adsorption of protons at the electrolyte-insulator surface. An interesting feature to be observed is that there exists a specific pH value for which the observed signal is maximized. At this optimized position, one can speculate that the effect of proton adsorption is minimized and therefore, the pH sensitivity of this device is quite low at this point. It is interesting to note that although this point might be unfavorable for regular ISFET devices operated as pH sensors, the BioFET will provide the best performance at these specific pH concentrations.

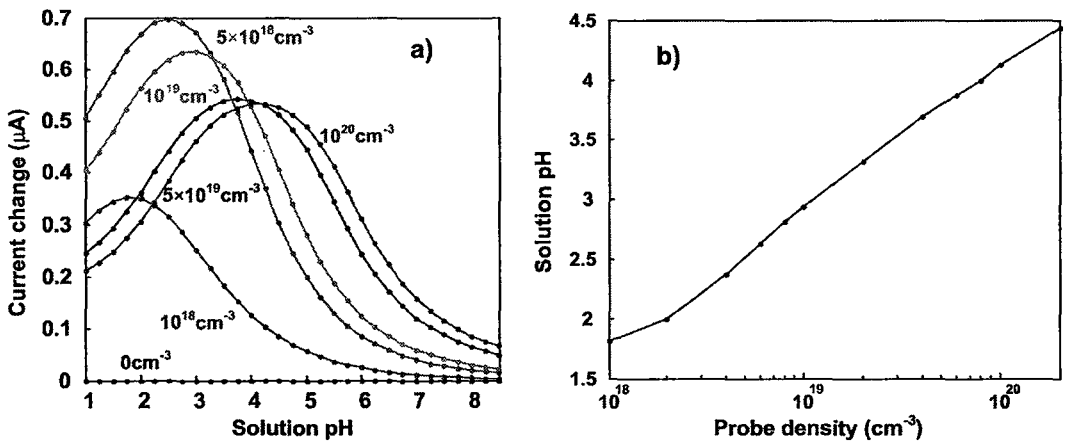

Figure 3.4 a) BioFET response curves as a function of the solution's pH value, and b) dependence of the pH of maximum sensitivity on the probe density

Figure 3.4a shows yet another important characteristic of the BioFET: The optimum sensitivity point changes with the amount of immobilized DNA, shifting to higher pH concentrations as the fixed DNA charge density goes higher. This is more easily seen with Figure 3.4b, which shows the dependence of the pH of maximum BioFET current with the probe density. The shift of the point of maximum sensitivity can be explained by noting that denser DNA membranes will cause the potential to be reduced in the interfacial region, making this region favorable for protons (as per equation 2.19). The higher proton density at the surface restores the pH sensitivity of the BioFET, allowing for more charge screening. This will cause the point of optimum sensitivity to be

shifted to higher pH values. In those regions, even with the strongly negative DNA membrane, surface protons will not be enough to screen the DNA charges, and high sensitivity can be obtained at those points.

Figure 3.5 shows simulation curves that illustrate the effect of the presence of the DNA membrane on the threshold voltage of the BioFET. At high enough pH values, the pH sensitivity curve is very linear, with a characteristic slope in the vicinity of 50mV/pH for SiO_2 [28]. This slope is hardly affected by the DNA membrane's presence, because at such high pH, the change in the local proton concentration at the insulator surface due to the presence of the DNA molecules is very small. However, at lower pH values, the membrane can drastically affect the pH sensitivity of the BioFET. For the values given in Table 3.1, Figure 3.5 allows us to pick the proper pH value such that the DNA sensitivity of the sensor is maximized. This would coincide with the flatter regions of the pH sensitivity curves.

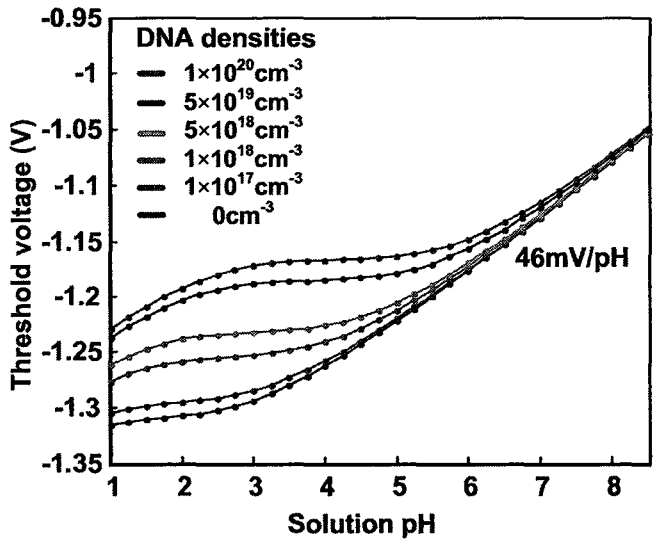

Figure 3.5 Threshold voltage shift as a function of the solution's pH value

A final note on the effect of the solution's pH value on the BioFET response is that at very low, and very high pH values, the effects of these water ions cannot be neglected in the Gouy-Chapman-Stern double layer model. They must therefore be incorporated into equation 2.7. These ions will now affect the BioFET in two different ways: by changing the potential drop in the double layer and by changing the value of the

adsorbed ions on the insulator's interface. However, environmental samples, and many different biological fluids (with the exception of gastric fluids) are usually neither acidic nor basic. Therefore, the effect of the pH on the double layer is neglected.

3.4 Insulator Effects on Sensitivity

The nature of the insulator can affect the sensitivity of the BioFET in many ways. Higher dielectric constants allow for higher electrostatic coupling between the electrolyte and the semiconductor. Figure 3.6 shows simulation results for a range of dielectric constants and different probe densities. Table 3.2 shows examples of different insulator materials and their dielectric constants [45]. It can be seen that the increase in the gate dielectric capacitance due to the insulators with higher dielectric constants causes an increase in the sensitivity of the BioFET. What is more important is that this dependence is nonlinear. This is because of the compounded nonlinearity of the effect of the dielectric capacitance on the total effective series capacitance (with the cover layer), and the involvement of this capacitance in the potential balance (equation 2.28).

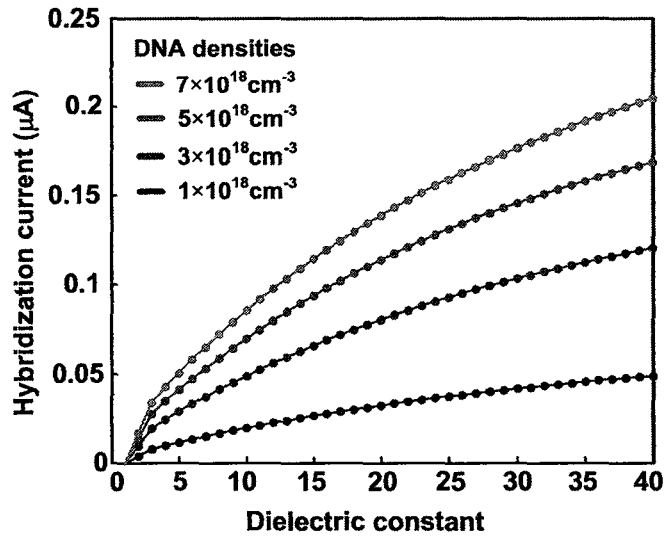

Figure 3.6 The effect of the dielectric constant on the hybridization current

Table 3.2 Dielectric constants for several insulator materials [45]

Insulator	Dielectric constant
SiO_2	3.9
Si_3N_4	7.5
Al_2O_3	10
Ta_2O_5	25
TiO_2	30-80

The thickness of the dielectric will also play an important role in the sensitivity of the BioFET. In fact, the dependence of the sensitivity on thickness is expected to exhibit a more nonlinear behavior than that of the dielectric constant, since the thickness is inversely proportional to the capacitance. Figure 3.7 shows the BioFET's sensitivity as a function of the insulator's thickness. It is indeed seen that the dependence curve is highly nonlinear, with higher sensitivities obtained at lower thicknesses. It is important to note that for very thin insulators, current might be able to flow through the insulator as a result of redox operations between the semiconductor and the electrolyte, assisted by quantum-mechanical tunneling [46]. If this effect is present, the model of the BioFET presented in chapter 2 would not be valid. This is because the semiconductor and electrolyte would both be in nonequilibrium. Significant amount of voltage drops might appear across the electrode-electrolyte interface, or the bulk electrolyte. In addition, the expressions for the statistical distribution of the ions in the double layer, and that of the carriers in the semiconductor channel, will no longer be applicable. In this case, a steady state solution with a given amount of current flow must be found using current continuity equations and incorporating the three mechanisms of current conduction involved here: diffusion, drift and quantum-mechanical tunneling.

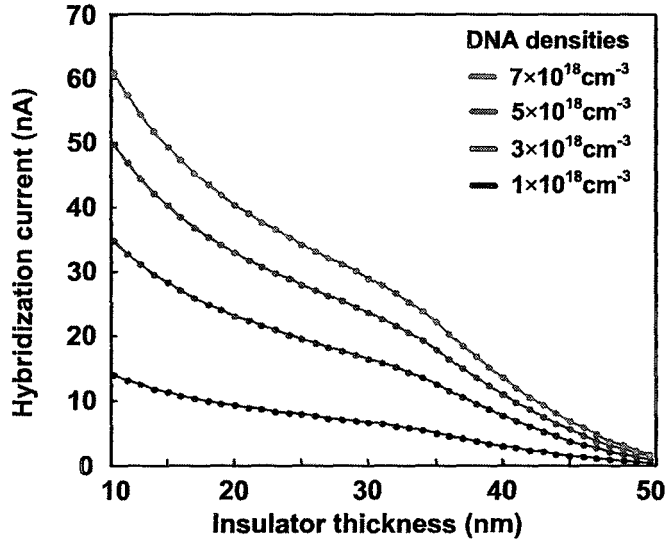

Figure 3.7 The effect of changing the insulator's thickness on the sensitivity of the BioFET

A third parameter by which the insulator affects the response of the BioFET is the density of amphoteric sites. This depends on the nature of the insulator and the orientation of its lattice with respect to the vertical axis of the BioFET. Table 3.3 gives values for the amphoteric site densities of a few surfaces [37]. The larger the number of these sites, the more pH sensitive the device is expected to be, since there will be a higher probability of adsorption. Figure 3.8 shows simulation results of the BioFET's output signal with different adsorption site densities for different DNA densities. As can be seen, there is an almost inverse relationship between the site density and the sensitivity of the BioFET. It is therefore important to have insulators with as few amphoteric sites as possible so that the amount of hydrogen adsorption is negligible, and the sensitivity to DNA charges is maximized.

Table 3.3 Density of amphoteric sites for different surfaces [37]

Surface	Site density (cm^{-3})
SiO_2	5×10^{14}
Al_2O_3	8×10^{14}
Ta_2O_5	10×10^{14}
Gold	1×10^{8}

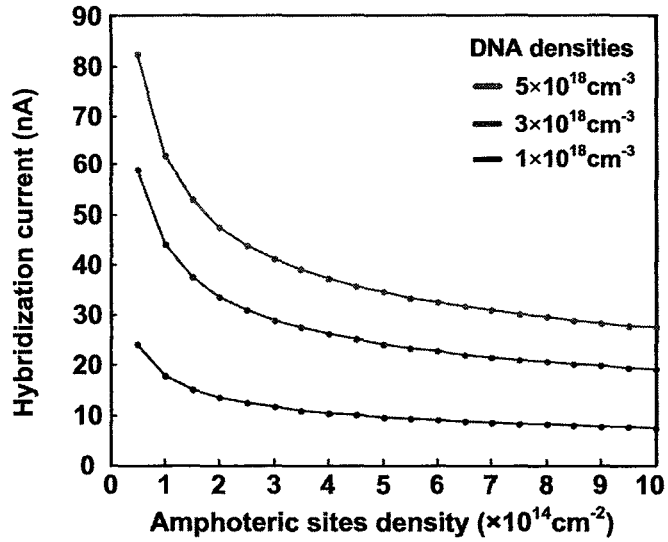

Figure 3.8 The effect of amphoteric sites density on the sensitivity of the BioFET for three values of DNA density

3.5 Solution Effects and Ionic Concentration

The composition of the electrolyte solution can severely affect the sensitivity of the BioFET, as the charge screening is done mainly by the ions in the electrolyte. The potential profile of the double layer and within the DNA membrane can vary with the ionic population in the solution bulk. The types of ions, their valence, and their sizes can give rise to a different charge screening efficiency, or can even be specifically adsorbed onto the surface sites, which can be catastrophic to the sensitivity of the BioFET.

As the electrolytic strength increases, it is expected that the charge screening ability will increase as well, since the screening length is dependent on the ionic concentration. The screening length is given by the Debye-Hückel, or inverse Debye length, parameter:

$$\kappa = \sqrt{\frac{2(zq)^2 n_0}{\varepsilon kT}}, \qquad 3.4$$

where n_0 is the ionic concentration (cm^{-3}). Figure 3.9 shows simulation results of the BioFET's response for different ionic concentrations. It is indeed noticed that higher ionic

concentrations severely inhibit the hybridization signal due to the electrolyte's high capability of screening due to the short Debye length. From Figure 3.9, we can see that this desensitization follows a power law (translated into a linear relationship in log-log scale) for low electrolyte concentrations. Furthermore, the slope of the desensitization curve is independent of the immobilized DNA density. This result shows that changing the DNA probe density does not help reduce the screening effects of the electrolyte.

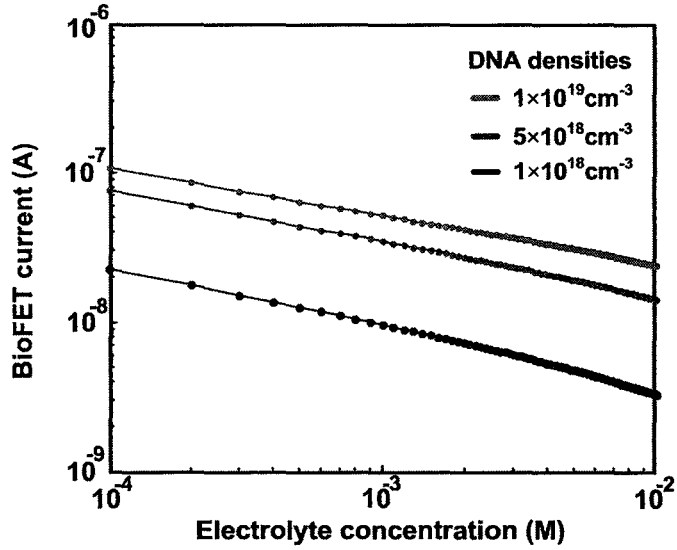

Figure 3.9 Desensitization of the BioFET due to increased ionic concentration

Although it might seem obvious that the BioFET should be operated at quite low electrolytic concentration, so as not to compromise its sensitivity, it is important to note that very low electrolytic concentrations might reduce the hybridization efficiency. This is because the shielding of the ssDNA charges will be less efficient, and therefore the target ssDNA molecule might not be able to diffuse effectively towards the probe, due to electrostatic repulsion. In addition, very low electrolytic concentration increases the resistivity of the solution, and this in turn can add thermal noise to the device, reducing its minimum achievable sensitivity. An optimum electrolytic concentration must therefore be chosen so as to achieve a balance between settling time and sensitivity. The effect of ionic strength on the kinetics of DNA molecules has been studied previously [47] and it was concluded that higher ionic concentrations can indeed speed up the kinetics of DNA interactions.

The effect of ionic shielding becomes more severe at very high electrolyte concentrations. This is shown in Figure 3.10. It can be seen that the sensitivity degrades more rapidly at higher electrolytic concentrations. This behavior can be attributed to the increased screening ability of the electrolyte at higher concentrations.

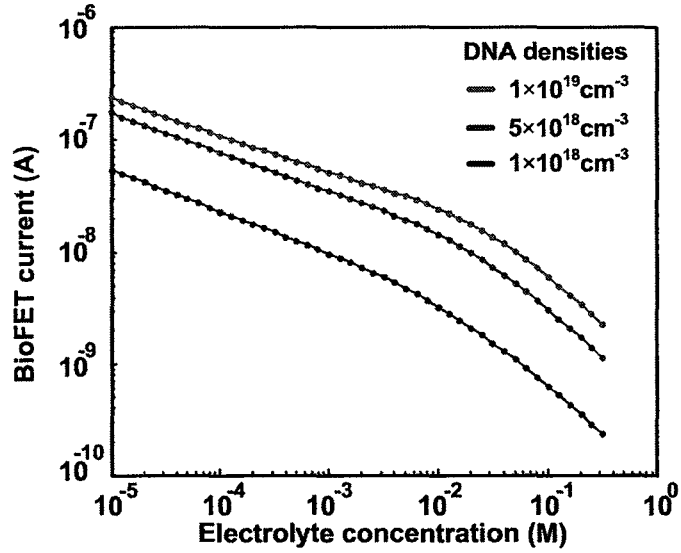

Figure 3.10 BioFET response at high ionic concentrations

Figure 3.11 shows a diagram of a BioFET, showing the width of the charged DNA membrane. As long as the Debye length ($1/\kappa$) is large compared to the DNA membrane width, increasing the ionic concentration will not introduce a large amount of counter-charge into the DNA membrane. However, as the Debye length becomes smaller than the DNA membrane width, changing the ionic strength will allow more charge to screen the DNA molecules. A crude mathematical justification for this effect follows: If we assume that the DNA molecules do not produce too much excessive charge onto the membrane area, then we can speculate that the PB equation will remain somewhat valid without the charge perturbation. In addition, if the potentials involved are not too high, we can even linearize the hyperbolic sine term and use the linear PB equation:

$$\frac{d\psi}{dx} = \kappa^2 \psi . \qquad 3.5$$

With a vanishing potential at the bulk, the solution to this equation is given by:

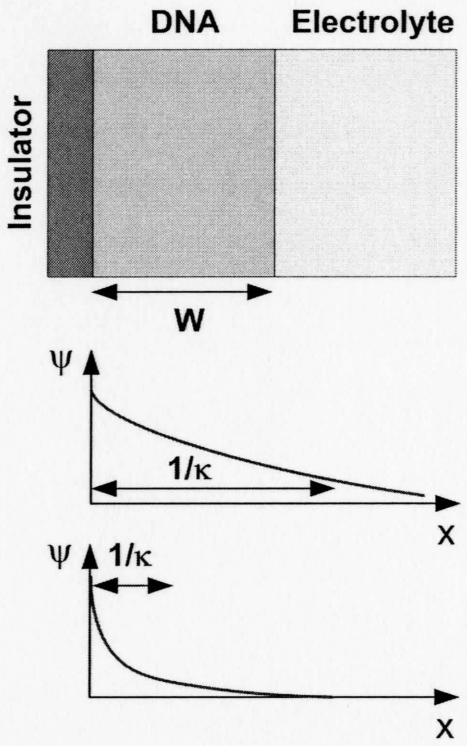

Figure 3.11 Illustration of the screening charge dependence on the Debye length

$$\psi = \psi_0 e^{-\kappa x}. \tag{3.6}$$

If we assume that the charge density is positive within the double layer, the quantity Ψ_0 will be negative. Using Gauss's law, we can find the total charge density within the membrane area:

$$\begin{aligned} Q_{membrane} &= \varepsilon\left(E_w - E_0\right) = \varepsilon\left(\left.\frac{d\psi}{dx}\right|_0 - \left.\frac{d\psi}{dx}\right|_w\right) \\ &= \varepsilon\kappa\psi_0\left(e^{-\kappa w} - 1\right) \\ \frac{dQ_{membrane}}{d\kappa} &= \varepsilon\psi_0\left(\left(1-\kappa w\right)e^{-\kappa w} - 1\right) \end{aligned} \tag{3.7}$$

For a double layer with positive accumulated charge, Figure 3.12 shows the normalized screening charge as a function of the Debye-Hückel parameter for a 10 nm wide DNA membrane. It can be seen that as the value of κ goes higher, so does the amount of screening charge. If an incremental change in the DNA charge appears as a result of hybridization, then the differential change in the screening charge would be

proportional to the amount of charge that initially existed. Thus, the screening effect will be worse for higher values of κ. This is why the screening effect becomes more drastic at higher electrolyte concentration.

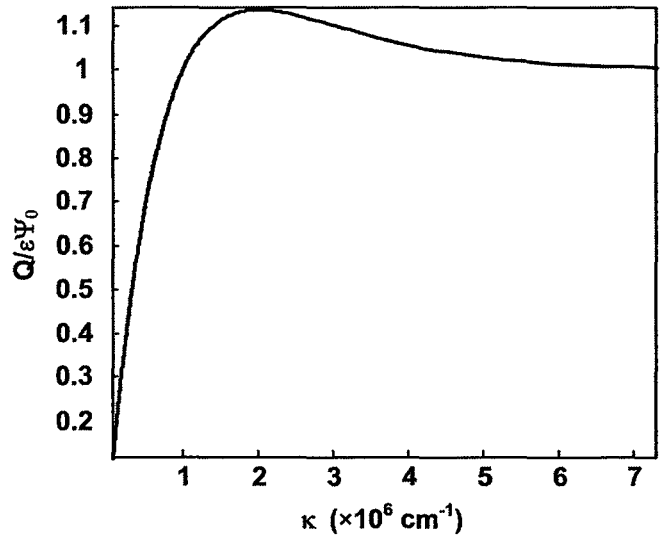

Figure 3.12 Normalized screening charge vs. the inverse Debye length

The valence of the ions that constitute the solute can also affect the screening efficiency, thereby reducing the sensitivity of the BioFET. In Figure 3.13, the plot of the BioFET's current as a function of the valence of a balanced electrolyte is given. Fractional valence values were included in the simulation to allow a smoother curve transition, despite the fact that they have no physical meaning. The figure shows that higher valence ions can better screen the DNA charges and can reduce the sensitivity of the BioFET. It is therefore desirable to use monovalent salt solutions. However, this might not always be an option, especially if the solution is taken directly from a biological sample without processing. Such a solution may contain ions of specific valences. Moreover, different ionic species might exist. This would complicate the formulation of the double layer and can change the corresponding equations. The PB equation for an ionic solution containing m different species would be re-written as follows:

$$\frac{d^2\phi(x)}{dx^2} = -\frac{q}{\varepsilon}\left(\sum_{i=1}^{m} z_i n_{i,0} e^{-\frac{z_i q\phi(x)}{kT}}\right). \qquad 3.8$$

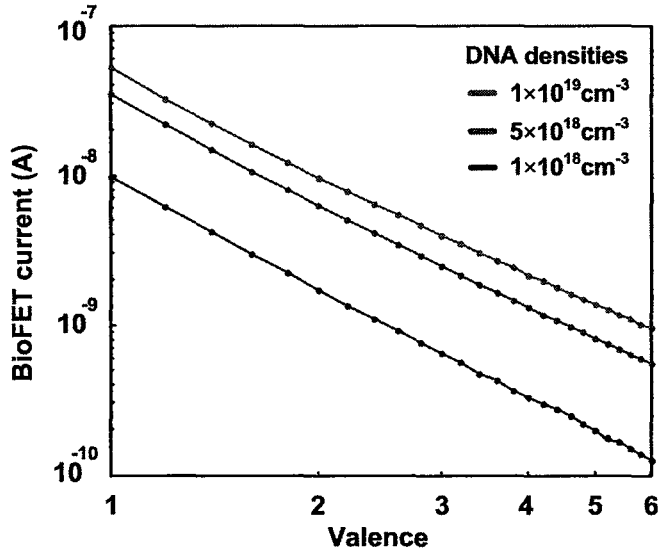

Figure 3.13 The relationship between the equivalent ionic valence and the BioFET's signal

This equation cannot be solved analytically in the general case. However, if the solution is balanced, then for each positive ion of a certain valence, there is a negative ion of equal valence with the same bulk concentration. If this is the case, then equation 3.8 can be solved using an equivalent valence value that is equal to the sum of valences for the positive species. Figure 3.13 illustrates how these added species can aid in the charge screening. Specifically, as the valence increases, the current due to hybridization decreases. The graph once again suggests a power-relationship between the equivalent valence and the sensed signal, which translates to a linear curve in the log-log scale.

Within the DNA region, the solvent's molecules tend to lose their bulk structure due to the DNA permeation. The structure can be highly anisotropic, particularly in regions too close to the DNA molecules. This effect would be particularly true if the density of probes is quite high. The effect of this re-orientation of water molecules is that the reaction to applied electric fields will be different from that of the bulk. To a first order approximation, one might assign a different value for the dielectric constant in the DNA membrane area than that used in the bulk [37]. The dielectric constant of water is taken as 78.4. Figure 3.14 shows the effect of varying the equivalent dielectric constant of the membrane area. It can be seen that polarization of the solvent molecules can reduce the sensitivity of the BioFET. However, the simulation of Figure 3.14 shows that this

effect is generally less than that of other parameters, such as ionic concentration or solution pH. However, for very high DNA concentrations, this variation might be significant enough to cause ambiguity in the determination of the BioFET current.

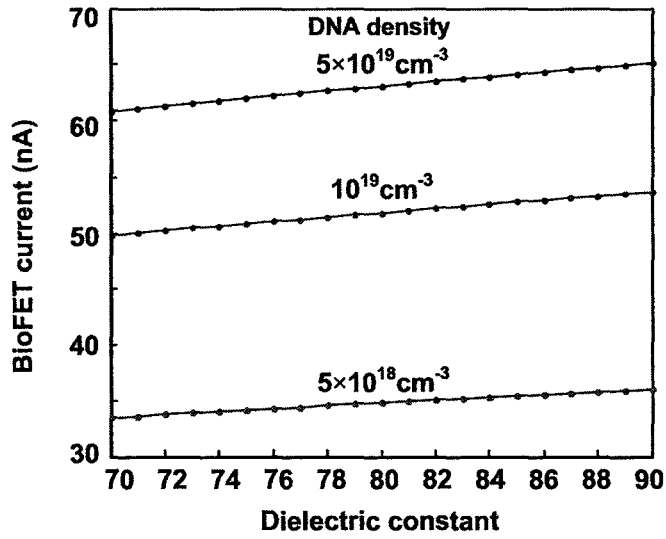

Figure 3.14 The effect of polarization of the solution

3.6 The Effect of the DNA Probes

The main parameter that determines the sensitivity of the BioFET is the amount of DNA probes that attract target molecules and produce an electrical signal. It is intuitively expected that the higher the DNA probe density, the more hybridization current will be given by the BioFET. However, the maximum amount of DNA probes that can be attached is dependent on many factors. First, the dimensionality of the ssDNA strands limits the maximum charge density to around 7.35×10^{20} cm^{-3}. In addition, the number of covalent bonds on the cover layer that allow for ssDNA tethering will be generally less than the maximum possible ssDNA density. Kinetics of immobilization can lead to an equilibrium ssDNA density that is less than that of the covalent bonding sites. Finally, the density of the DNA might be deliberately thinned out to facilitate faster DNA hybridization [47].

The model presented in chapter 2 is able to relate the expected output current to the density of immobilized and hybridized DNA charges. Figure 3.15 shows simulation

results of the BioFET's response to hybridization for different DNA probe densities. It can be seen that the sensitivity is indeed increased as the number of receptors is increased. However, aside from the complications listed above, Figure 3.15 shows that the amount of gained sensitivity is reduced as the DNA density is increased. It is expected, therefore, that there will be some optimum density of immobilized ssDNA strands that will allow maximum sensitivity while not compromising other sensor performance parameters such as hybridization efficiency and time.

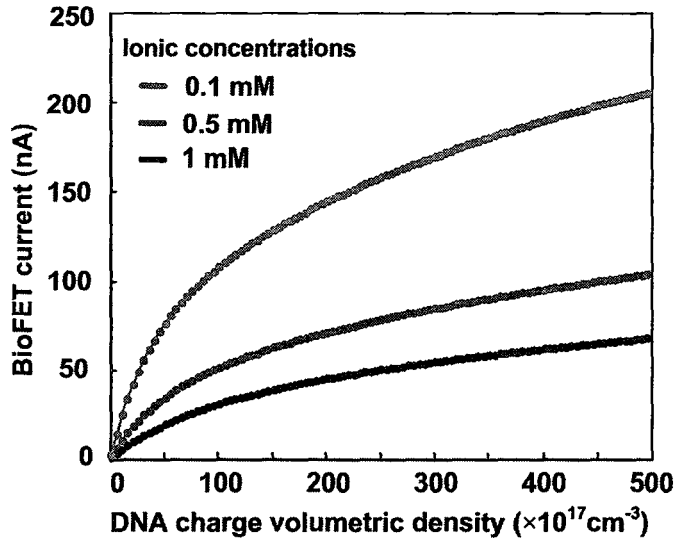

Figure 3.15 The effect of DNA probe density on the BioFET's current

In addition to the density of DNA probes, the length of the DNA strands also affects the solution of the electrostatic model, as this length determines the width of the DNA membrane area over which the charge perturbed PB equation must be solved. Although a higher DNA length would result in higher total DNA charge density, the charge on the DNA membrane edge is mostly shielded by the ionic countercharge within the membrane. The increase in density due to using higher DNA strand lengths should not provide the same degree of sensitivity enhancement as when increasing the probe density. Figure 3.16 shows simulation results obtained by varying the width of the DNA membrane region of the BioFET. It can be seen that above a certain membrane width, the response to the amount of DNA becomes almost independent of the strand length. This would mean that the additional hybridization charge that arises due to the length of the

DNA strands is effectively screened out. Figure 3.17 allows this effect to be investigated more thoroughly. With a narrow membrane, the entire potential profile must be calculated throughout the membrane with sufficient boundary conditions. However, as the membrane becomes thicker, the potential profile variation becomes quite small in the middle of the membrane. This is analogous to having an electrochemical cell consisting of an electrode-electrolyte-electrode structure. If the two electrodes are in close proximity to each other, the double layers at both interfaces overlap, and the entire potential profile can only be found by solving the PB equation over the entire electrolyte. However, if the electrodes are placed sufficiently far from each other, then one can speculate that the points far from the interface will be neutral, and that will allow for calculation of the potential profile using two separate PB equations, each applied to a different edge of the electrochemical cell.

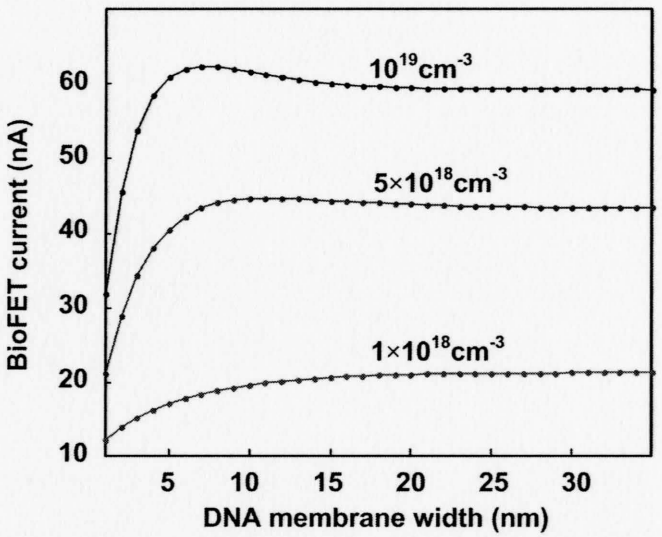

Figure 3.16 The effect of DNA strand length (membrane width) on the BioFET's current

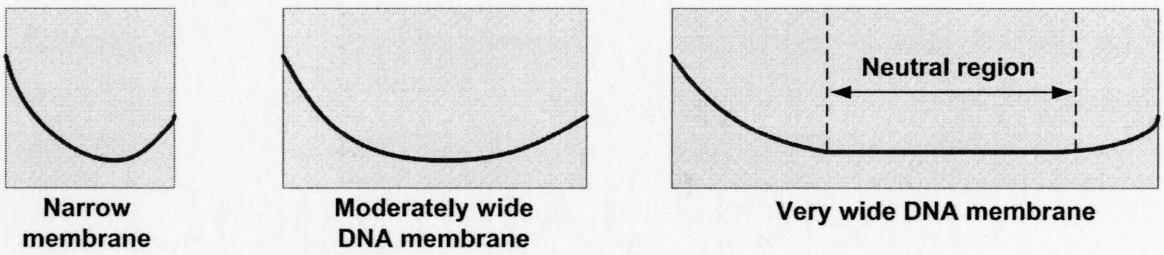

Figure 3.17 Comparison of potential profiles for different DNA widths

In the case of the DNA membranes, once the flat potential is observed in the potential profile, that is a sign of charge neutrality within that region. Thus, all the incremental charges in this region due to hybridization will go unsensed, because an equivalent amount of screening charge will be able to penetrate this area and neutralize this incremental charge to keep the potential profile flat within this region. The thicker the DNA membrane, the wider the flat region will be. This is why the sensitivity of the BioFET is not affected as the DNA strand length is increased beyond a certain point.

What is more important in Figure 3.16 is that for short DNA strand lengths, the sensitivity of the BioFET increases as the width is increased, and at a certain width, maximum sensitivity is reached. After this point, splitting of the potential profile and neutralization of the bulk membrane area will cause the sensitivity to degrade and finally become independent of the DNA strand length. When the width of the DNA is such that the potential profile does not split, there are two opposing phenomena: the increase of the DNA fixed charge density due to hybridization and the increase in the amount of ionic screening charge. At the peak of the BioFET's current curve, DNA charges overpower the ionic charges and that causes maximum device sensitivity. This point of maximum sensitivity is expected to, and indeed does, vary with the charge density and Debye length within the DNA membrane area. The conclusion is that a longer DNA strand does not necessarily mean a higher BioFET sensitivity.

A final remark on the length of the DNA probes is that it is expected that longer strands will require longer times of hybridization. This can be predicted intuitively by noting that complete hybridization requires a specific positioning and alignment between the probe and target ssDNA molecules. The longer the DNA molecules, the more different possibilities of inter-alignments and inter-orientations will exist. This will lead to longer times required for the hybridized molecules to form. On the other hand, extremely short hybridized DNA molecules might not be stable. A very small increase in temperature will cause some hybridized molecules to denature, adding to the uncertainty in the BioFET's signal. Finally, short DNA strands can reduce the selectivity of the

BioFET, as shorter sequences are more likely to be found in the different DNA strands of various microorganisms.

3.7 Device Biasing and Region of Operation

The biasing conditions of the BioFET are very crucial in determining the operational sensitivity of the sensor. Since the structure is essentially that of a MOS transistor, with hybridization charge being equivalent to that of some incremental potential applied to the reference electrode, and since the signal taken here is the DC drain current, it is expected that the best biasing point would be where the device's transconductance is maximum. For the MOSFET, this would imply saturated operation of the transistor. In order to fairly assess the biasing effects, it is important to incorporate the effect of mobility degradation into the expression for the drain current.

Mobility degradation in MOS transistors occurs at operation regions of higher inversion. The effective surface mobility of the carriers degrades as the carrier is subjected to higher vertical electric fields by virtue of the gate (reference electrode) potential. The degradation can be attributed to many different phenomena, including surface state scattering, and overlap of the carrier wave function with the insulator. To account for this effect, a common analytic expression for this dependence is the following inverse relationship:

$$\mu_{eff} = \frac{\mu_0}{1+\theta\left(V_{GS}-V_T\right)}, \tag{3.9}$$

where θ is the mobility degradation factor (V^{-1}) and V_T is the threshold voltage of the BioFET (V). The threshold voltage for the BioFET is given by the following equation:

$$V_T = V_{FBC} - \psi_{0,T} + 2\phi_F - \frac{\sigma_s\left(2\phi_F\right)}{C_{eff}}, \tag{3.10}$$

where $\Psi_{0,T}$ is the electrolyte surface potential at threshold bias. This has to be calculated numerically using the simulator. In addition, equation 3.9 is only valid at reference electrode potentials higher than the threshold voltage, while the nominal surface mobility is used for lower biases. This result causes a non-smooth transition in the current curve

as the mobility regime is changed. To remedy this, a smoothing Gaussian curve was used to join the two pieces of mobility behavior. The parameters for this "joining" function were chosen so as to maintain the continuity and differentiability of the mobility curve throughout this transition region. Figure 3.18 shows simulation results for the BioFET's hybridization current as a function of the applied gate bias. The optimum biasing point for sensitivity can be seen to be the point of maximum transconductance in the BioFET. Higher inversion levels cause a reduction in sensitivity due to mobility degradation.

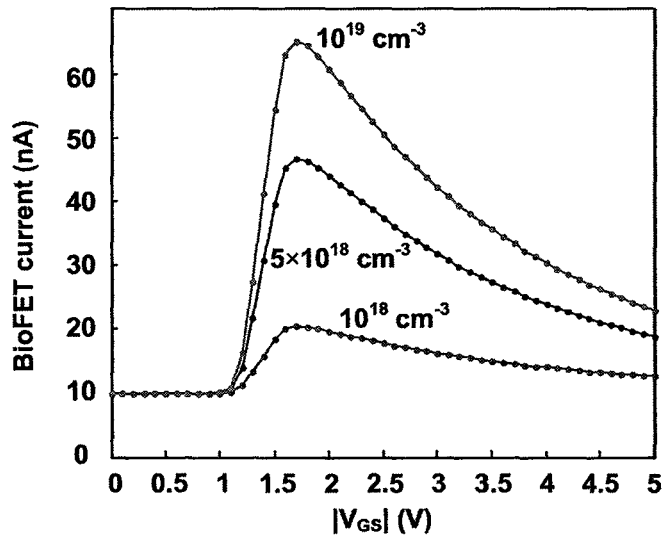

Figure 3.18 Effect of inversion level on the sensitivity of the BioFET

In addition to the gate bias, the region of operation of the FET structure (linear vs. saturation) will affect the amount of hybridization current. Figure 3.19 shows curves obtained by changing the drain-to-source bias with a fixed gate potential. It can be seen that the highest sensitivity values are achieved when the BioFET is saturated. In this simulation, velocity saturation effects have been neglected. The fact that the saturated BioFET offers the highest incremental current lends itself to the design of BioFET-based amplifiers, which require saturated transconductance FET devices.

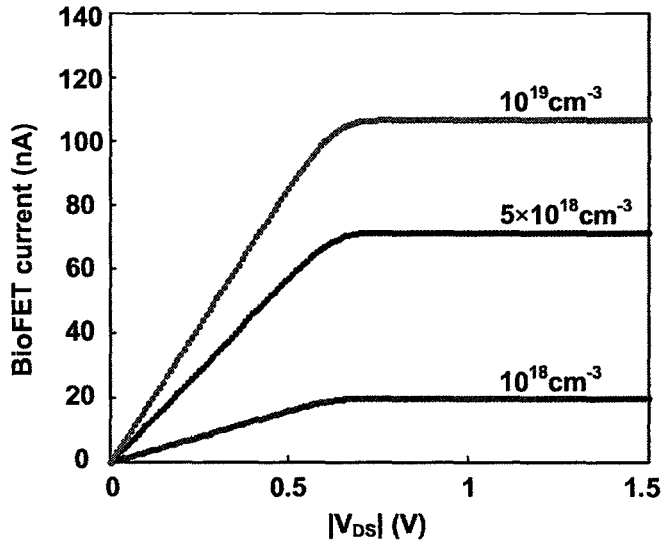

Figure 3.19 BioFET hybridization current vs. drain bias

3.8 Temperature Effects

Of all the parameters that affect the operation of the BioFET, temperature is the one which affects all the different phenomena that occur in the device. A change in the temperature can cause changes to the potential profile in the diffuse layer, the DNA membrane layer, and the proton adsorption and pH sensitivity. On the semiconductor side, changes in temperature can change the Fermi level of the semiconductor, the diffusion current, and to a lower degree the band gap and the mobility. For the parameters that are included in the model, Figure 3.20 shows the results of simulating the BioFET structure at different temperatures. It can be seen that the temperature sensitivity is higher for higher values of immobilized DNA strands.

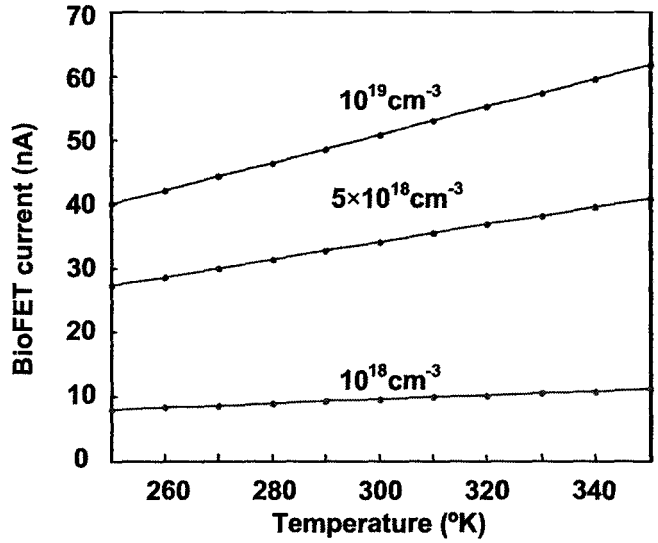

Figure 3.20 Temperature sensitivity of the BioFET

3.9 Other Effects

So far, the sensitivity of the BioFET was quantitatively assessed in light of the model presented. It is important, however, to realize that there are some effects that have not been included in this model. This section attempts to identify some of these effects and establish the mathematical equations that will be used to modify the model to take these effects into account.

One of the assumptions in this model was that the functionalization layer (cover layer) was impermeable to ions. This assumption allowed us to treat this layer as an insulator and adding it in series to the FET insulator. However, this will only be true for a fully dense array of the functionalization molecules. The binding sites of the insulator might not be dense enough to allow such a high density of self-assembled monolayer (SAM) molecules to be realized. In this case, ions will be able to permeate this layer. This can severely reduce the sensitivity of the BioFET because any ions in this region will screen the DNA charges more effectively than those in the double layer. Figure 3.21 shows a potential diagram of the BioFET with an ion-permeable functionalization layer. The effect of allowing ions in this region on the model is twofold: Firstly, the potential profile cannot be assumed linear within the functionalization layer anymore, but must

rather follow that of a solution of the PB equation with appropriate boundary conditions. Secondly, the Stern layer will no longer be at the electrolyte-cover layer interface, but rather at the cover layer-insulator interface. If the total charge density within the cover layer is denoted by σ_{cl}, and the potential at the cover-layer-insulator interface with respect to the bulk electrolyte is denoted by Ψ_{cl}, then the model equations have to be modified. The expression for the total electrolyte charge (equation 2.52) becomes:

$$\sigma_e = \sigma_0 + \sigma_{md} + \sigma_{cl}, \tag{3.11}$$

the expression for potential balance (equation 2.28) becomes:

$$V_{GB} = \chi_{sol} - \chi_{Si} - \frac{u_{sol}}{q} + \frac{u_s}{q} - \psi_0 - \frac{\left(\sigma_s + \sigma_f\right)}{C_{ins}} + \psi_s, \tag{3.12}$$

and the expression for the electrolyte surface potential (equation 2.51) is redefined as follows:

$$\psi_0 = \psi_{cl} - \frac{\left(\sigma_{md} + \sigma_{cl}\right)}{C_{Stern}}. \tag{3.13}$$

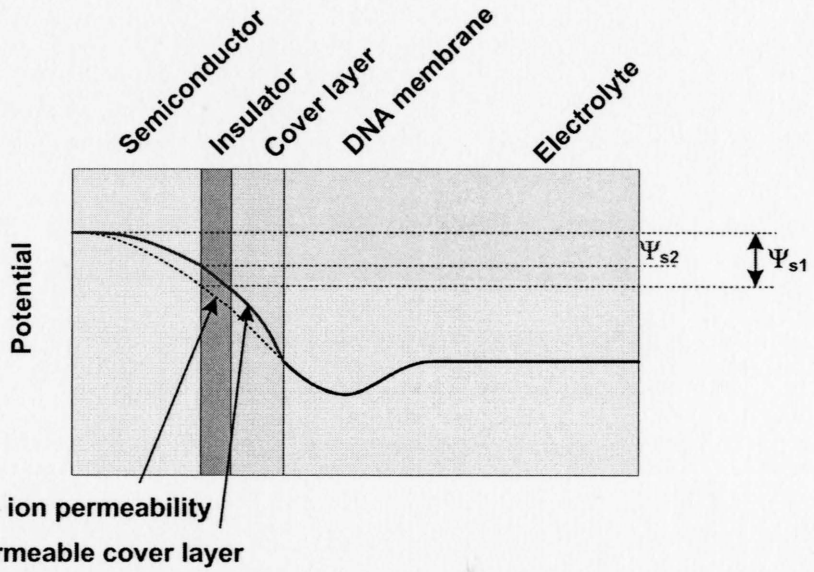

Figure 3.21 Illustration of desensitization due to cover layer permeability to ions

The quantity Ψ_{cl} will no longer be given by equation 2.27. It would have to be found by solving the PB equation:

$$\frac{d^2\psi(x)}{dx^2} = \frac{2qzn_0}{\varepsilon_{cl}}\sinh\left(z\beta\psi(x)\right), \tag{3.14}$$

with boundary conditions:

$$\begin{aligned} \psi(0) &= \psi_m \\ \psi'(0) &= \frac{\sigma_{md}}{\varepsilon_{cl}}. \end{aligned} \tag{3.15}$$

Finally, the procedure that was represented by equation 2.53 would require an additional step, which is the calculation of Ψ_{cl} from Ψ_{md} using equations 3.14 and 3.15. This new system of equations will allow the additional effects of DNA screening due to ions in the cover layer to be incorporated into the model, allowing for a more realistic assessment of the BioFET's sensitivity.

Another approximation that was considered in the model was that the electrode-electrolyte interface was in electrochemical equilibrium. This condition will only hold true in the case of a non-polarizable or partially polarizable electrode. Ideally polarizable electrodes cannot have electron transfer between the electrode and the redox couple in the solution. Electrochemical equilibrium cannot be reached in this case, and the potential drop at this interface will be a function of the applied bias. This will complicate the modeling of the BioFET since it adds another variable term into the equations. The charge accumulated in the electrode-electrolyte interface will consist of the constant term (due to differences in the work functions), and a variable term consistent with the Gouy-Chapman-Stern theory. In a sense, the electrode-electrolyte and electrolyte-insulator-semiconductor interfaces can be seen as two nonlinear capacitors in series, and the equation that couples their respective potential drops is the charge neutrality equation in the insulator, since there is no possible source of charge being inserted into the electrolyte, from the electrode or through the insulator. If the accumulated charge density within the electrode-electrolyte interface is $\sigma_{e\text{-}e}$, then the following equation must be added to the BioFET set of equations:

$$\sigma_{e-e} = \sigma_e. \tag{3.16}$$

The fact that the electrode-electrolyte potential difference is now varying will add another potential variable to equation 3.12. This variable can then relate to the new charge density $\sigma_{e\text{-}e}$ using the double layer theory. Now, the amount of screening charge due to DNA hybridization will change because there will be some change in the electrode-electrolyte interface as well. This will cause the expressions for the sensitivity to become more involved and the sensitivity is likely to be reduced because of this phenomenon.

3.10 Conclusion

In this chapter, quantitative analysis of the performance of the BioFET was conducted. It was shown how different parameters can affect the sensitivity of the BioFET's output signal to DNA hybridization. Most of the parameters of the sensor, such as the ionic concentration and the composition of the solution, affect the sensitivity of the BioFET. Obtaining the maximum sensitivity requires careful selection of all of these parameters. Table 3.4 gives a summary of the effects of different parameters on the BioFET's current. The next chapter presents several approximations that simplify the analysis of the BioFET, and discusses another phenomenon that can limit the sensitivity of the BioFET: device noise.

Table 3.4 Summary of the effects of different parameters on the BioFET's current

Increased parameter	BioFET current	Remarks
pH	Can be increased or decreased	Optimum pH exists
Dielectric constant	Increases	Sublinear
Insulator thickness	Decreases	-
Amphoteric sites	Decreases	Reaches a minimum
Ionic concentration	Decreases	Power law decay
Ionic valence	Decreases	Power law decay
DNA probe density	Increases	Sublinear
Probe length	Can be increased or decreased	Optimum length exists
V_{REF}	Can be increased or decreased	Mobility dependent
V_{DS}	Increases	Reaches a maximum
T	Increases	Scattering effects neglected, high T can impair hybridization

Chapter 4

MODEL APPROXIMATIONS, EQUIVALENT CIRCUIT, AND NOISE

4.1 Introduction

The previous two chapters dealt with physical modeling of the BioFET, including important effects that can influence the sensitivity of the device. The next step would be to integrate the BioFET with interface circuits to establish an entire microarray cell. The sensitivity of the BioFET sensor can be enhanced by incorporating various microelectronic circuit techniques. Unfortunately, the numerical methods involved in solving the BioFET equations are not suitable for circuit simulator programs. It is therefore desirable to make some approximations that will allow easier solution of the equations of the BioFET. In addition, different sources of electronic noise within the BioFET can severely degrade the sensitivity of the device. This becomes very important when trying to achieve very high sensitivity values. In this chapter, some approximations will be carried out to arrive at a more analytic formulation of the BioFET model. The small-signal low-frequency equivalent circuit model for the BioFET will be shown, and the expected noise performance and signal-to-noise ratio of this device will be addressed.

4.2 Approximations to the Poisson-Boltzmann Equations

The first approximation that can be made is linearization of the PB equations. The hyperbolic sine function can be linearized if the potential is to within a few tenths of the thermal voltage. However, as this is not usually valid, we introduce a factor that allows

for a bigger range of the potential, while sacrificing some accuracy in the equations. Figure 4.1 shows the difference between the normal Taylor series linear approximation, and that with a scaling factor. It can be seen that, although the accuracy is lost in the intermediate points, the approximation is valid for a higher range of the potential. Therefore, to get better linear approximations, it is essential to choose the scaling factor so as to include the potential ranges of interest, while minimizing the linearization errors. An optimum value of the scaling factor can be chosen such as to minimize the total error within a range of interest. A technique such as the least squares algorithm might be used in this case.

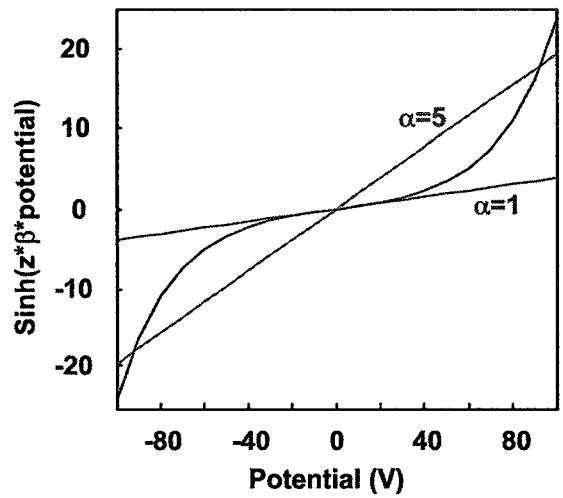

Figure 4.1 Different approximations to the nonlinearity of PB equation

If we use a dimensionless variable $u=z\beta\Psi$ for the potential, the linear approximation results in the following expression for the PB equation:

$$\frac{d^2u(x)}{dx^2} \approx \kappa_w^2 \alpha u(x), \qquad 4.1$$

where κ_w is the Debye-Hückel parameter for the electrolyte solution (cm^{-1}), and α is the scaling factor discussed above. The solution to equation 4.1, given the boundary conditions of vanishing electric field and potential at the bulk of the electrolyte, is:

$$u(x) = u_d e^{-\kappa_w \sqrt{\alpha} x}. \qquad 4.2$$

The charge stored within this region would be given by:

$$\sigma_d = -\sqrt{\alpha}\varepsilon_w \kappa_w \psi_d \,. \tag{4.3}$$

The next step would be to linearize the charge perturbed PB equation in the DNA membrane layer. The original equation can be written as follows [37]:

$$\frac{d^2u}{dx^2} = \kappa_m^2 \left(\sinh(u) - \sinh(u_{DP})\right), \tag{4.4}$$

where u_{DP} is the normalized Donnan potential, defined as:

$$u_{DP} = \sinh^{-1}\left(\frac{N_m}{2zn_0}\right). \tag{4.5}$$

Now, equation 4.4 can be linearized as well. We can also include a scaling factor for maximum potential range. However, in this case, if the potential along the membrane is close enough to the Donnan potential (true for wide enough membranes); we can come up with an expression for the scaling value:

$$\begin{aligned}
&\frac{d^2u}{dz^2} = \kappa_m^2 \left(\sinh u - \sinh u_{DP}\right) \\
&\frac{d^2u}{dz^2} = \kappa_m^2 \left(\left(u - u_{DP}\right) + \frac{\left(u^3 - u_{DP}^3\right)}{3!} + \frac{\left(u^5 - u_{DP}^5\right)}{5!} + \ldots \right) \\
&= \kappa_m^2 \left(u - u_{DP}\right) \left(1 + \frac{\left(u^2 + uu_{DP} + u_{DP}^2\right)}{3!} + \frac{\left(u^4 + u^3u_{DP} + u^2u_{DP}^2 + uu_{DP}^3 + u_{DP}^4\right)}{5!} + \ldots \right) \\
&= \kappa_m^2 \left(u - u_{DP}\right) \left(\sum_{i=0}^{\infty} \frac{\sum_{j=0}^{2i} u^j u_{DP}^{2i-j}}{(2i+1)!} \right)
\end{aligned} \tag{4.6}$$

Now, if $|u-u_{DP}|<1$, we can have any of the following approximations:

$$\begin{aligned}
u^j u_{DP}^{2i-j} &\approx u_{DP}^{2i} \\
u^j u_{DP}^{2i-j} &\approx u^{2i} \\
u^j u_{DP}^{2i-j} &\approx \left(uu_{DP}\right)^i
\end{aligned} \,. \tag{4.7}$$

We choose the first approximation so that we can arrive at an analytic result:

$$\frac{d^2u}{dz^2} \approx \kappa_m^2 (u-u_{DP}) \left(\frac{\sum_{j=0}^{2i} u_{DP}^{2i}}{\sum_{i=0}^{\infty} \frac{}{(2i+1)!}} \right)$$

$$\frac{d^2u}{dz^2} \approx \kappa_m^2 (u-u_{DP}) \left(\sum_{i=0}^{\infty} \frac{u_{DP}^{2i}}{(2i)!} \right) \quad . \qquad 4.8$$

$$\frac{d^2(u-u_{DP})}{dz^2} \approx \delta \kappa_m^2 (u-u_{DP}) \cosh(u_{DP})$$

The parameter δ was added in equation 4.8 and is analogous to the role played by the parameter α in equation 4.1. Equation 4.8 can be solved with given boundary conditions. The general solution is given by:

$$u = u_{DP} + Ae^{-\zeta x} + Be^{\zeta x}$$
$$\zeta = \kappa_m \sqrt{\delta \cosh(u_{DP})} \quad . \qquad 4.9$$

To determine the constants A and B, we invoke the boundary conditions at the DNA membrane edge (x=w). The boundary conditions require that the potential and electric flux density be continuous. Thus:

$$u(w) = u_{DP} + Ae^{-\zeta w} + Be^{\zeta w} = u_d$$
$$\varepsilon_m u'(w^-) = \varepsilon_w u'(w^+) = z\beta\sigma_d \quad . \qquad 4.10$$
$$-\zeta Ae^{-\zeta w} + \zeta Be^{\zeta w} = \frac{z\beta\sigma_d}{\varepsilon_m}$$

Solving for A and B, we get:

$$A = \left(\frac{u_d - u_{DP}}{2} - \frac{z\beta\sigma_d}{2\zeta\varepsilon_m} \right) e^{\zeta w}$$
$$B = \left(\frac{u_d - u_{DP}}{2} + \frac{z\beta\sigma_d}{2\zeta\varepsilon_m} \right) e^{-\zeta w} \quad . \qquad 4.11$$

When these values for A and B are inserted into equation 4.9, and the expression is evaluated for the potential at the edge of the membrane u_m, we get:

$$u_m = u_{DP} + \left(\frac{u_d - u_{DP}}{2} - \frac{z\beta\sigma_d}{2\zeta\varepsilon_m}\right)e^{\zeta w} + \left(\frac{u_d - u_{DP}}{2} + \frac{z\beta\sigma_d}{2\zeta\varepsilon_m}\right)e^{-\zeta w}$$
$$u_m = u_{DP}\left(1-\cosh(\zeta w)\right) + u_d\left(\cosh(\zeta w) + \left(\frac{\sqrt{\alpha}\varepsilon_w\kappa_w}{\zeta\varepsilon_m}\right)\sinh(\zeta w)\right). \quad 4.12$$

Equation 4.12 relates the potentials at the two edges of the DNA membrane without the need to numerically solve the differential equation. Now, the total charge density at the DNA membrane edge is given by:

$$\sigma_{md} = \varepsilon_m \left.\frac{d\psi}{dx}\right|_{0+}$$
$$\sigma_{md} = \frac{1}{z\beta}\left(\zeta\varepsilon_m u_{DP}\sinh(\zeta w) - u_d\left(\sqrt{\alpha}\varepsilon_w\kappa_w\cosh(\zeta w) + \zeta\varepsilon_m\sinh(\zeta w)\right)\right). \quad 4.13$$

Now, the potential in the electrolyte-insulator region can be given as a function of the potential u_d:

$$zu_0 = u_m - \frac{z\beta\sigma_{md}}{C_{Stern}}$$
$$zu_0 = u_{DP}\Pi_{DP} + u_d\Pi_d, \quad 4.14$$
$$\psi_0 = \psi_{DP}\Pi_{DP} + \psi_d\Pi_d$$

where

$$\Pi_{DP} = 1 - \cosh(\zeta w) - \frac{\zeta\varepsilon_m\sinh(\zeta w)}{C_{Stern}}$$
$$\Pi_d = \cosh(\zeta w) + \left(\frac{\sqrt{\alpha}\varepsilon_w\kappa_w}{\zeta\varepsilon_m}\right)\sinh(\zeta w) + \frac{\left(\sqrt{\alpha}\varepsilon_w\kappa_w\cosh(\zeta w) + \zeta\varepsilon_m\sinh(\zeta w)\right)}{C_{Stern}}, \quad 4.15$$

and u_0 has been defined as $\beta\Psi_0$ instead of $z\beta\Psi_0$.

4.3 Approximations to the Charge Adsorption Equations

The relationship between the potential and adsorbed charge density is highly nonlinear, as can be seen from the sample curve given in Figure 4.2. If we would like to linearize this curve, we generally cannot arrive at a single accurate linear model. What we would have to do instead is define a piecewise linear model for this curve. From Figure 4.2, it is clear

that there exist two regions of severe pH sensitivity, and a region where the sensitivity is minimum. We attempt to represent this curve with three linear equations. These lines will be centered on the point of zero charge (pzc), and the points where the charge density is half that of the amphoteric sites. The linear model will look like that of Figure 4.3a. We must also take care of the surface saturation effects at high charge densities so that the linear model does not predict charge densities that are higher than the density of amphoteric sites.

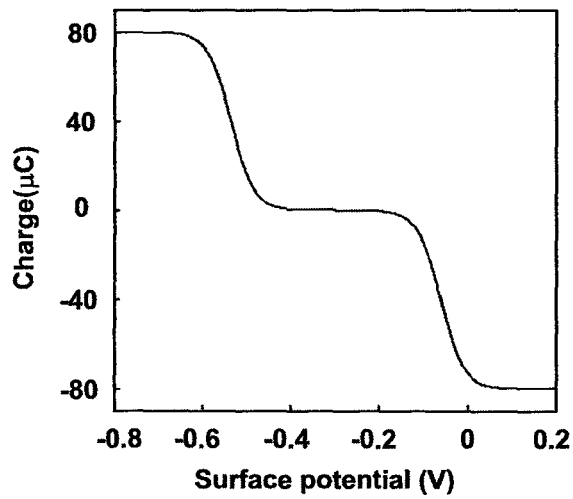

Figure 4.2 Adsorption curve for SiO_2 surface

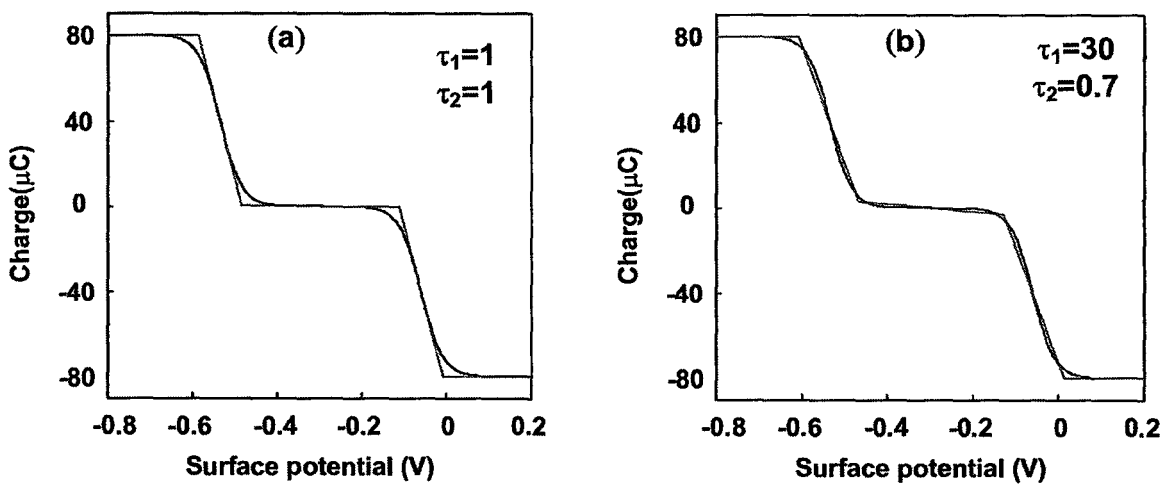

Figure 4.3 Piecewise linear approximation with different slope choices

To identify the center points of the linear curves, we start with the initial equation describing the nonlinear relationship:

$$\sigma_0 = qN_s \left(\frac{\frac{[H^+]_0}{K_a} e^{-u_0} - \frac{K_b}{[H^+]_0} e^{u_0}}{1 + \frac{[H^+]_0}{K_a} e^{-u_0} + \frac{K_b}{[H^+]_0} e^{u_0}} \right). \tag{4.16}$$

The potential of zero charge (u_{00}) can be solved, yielding:

$$u_{00} = \ln\left(\frac{[H^+]_0}{\sqrt{K_a K_b}} \right) = 0.2303\left(pH - \frac{1}{2}\left(pK_a + pK_b \right) \right). \tag{4.17}$$

The potential at which the surface is charged to half its capacity can also be found. The solution steps are omitted but the results are given below:

$$\begin{aligned} u_{0,0.5+} &= \ln\left(\frac{[H^+]_0}{6K_b}\left(\sqrt{1+12K_b/K_a} - 1 \right) \right) \\ u_{0,0.5-} &= \ln\left(\frac{[H^+]_0}{2K_b}\left(\sqrt{1+12K_b/K_a} + 1 \right) \right) \end{aligned}. \tag{4.18}$$

With these center points derived, what remains is to find the slopes of the curves at these points. After some mathematical manipulations, the results follow:

$$\begin{aligned} m_{0,0} &= -q\tau_1 N_s \left(\frac{2\sqrt{K_b/K_a}}{1+2\sqrt{K_b/K_a}} \right) \\ m_{0,0.5+} &= m_{0,0.5-} = q\tau_2 N_s \left(\frac{1}{4} - \frac{1+8K_b/K_a+\sqrt{1+12K_b/K_a}}{2+8K_b/K_a+2\sqrt{1+12K_b/K_a}} \right) \end{aligned}. \tag{4.19}$$

Once again, the parameters τ_1 and τ_2 were added to provide a more accurate estimate of the nonlinear adsorption curve, similar to the reason for introducing parameters α and δ. Changing these two parameters can lead to a higher overall accuracy, as is evident from Figure 4.3b. For many interfaces, $K_a >> K_b$ [37], therefore, the slopes can be approximated as follows:

$$\begin{aligned} m_{0,0} &\approx 0 \\ m_{0,0.5+} &= m_{0,0.5-} \approx -\frac{qN_s}{4} \end{aligned}. \tag{4.20}$$

The three linear equations that describe the pH dependence of the BioFET are summarized below:

$$\begin{aligned}\sigma_0 &= m_{0,0}\left(u_0 - u_{00}\right)\\ \sigma_0 &= \pm\frac{qN_s}{2} + m_{0,0.5\pm}\left(u_0 - u_{0,0.5\pm}\right)\end{aligned}. \qquad 4.21$$

The limits of applying the different linear equations above can be derived by finding the intersection points. This results in the following limits:

$$u_0 = \frac{\pm\frac{qN_s}{2} + m_{00}u_{00} - m_{0,0.5\pm}u_{0,0.5\pm}}{m_{00} - m_{0,0.5\pm}}. \qquad 4.22$$

4.4 Approximate BioFET Model

From the total charge neutrality within the BioFET, the semiconductor charge can be related to the total charge in the electrolyte. Thus, if we re-write the equations in terms of absolute potentials instead of the normalized variables, we get:

$$\begin{aligned}\sigma_e &= \sigma_0 + \sigma_{md}\\ &= \sigma_{0x} + \beta m_{0,x}\left(\psi_0 - \psi_{0,x}\right) + \sigma_{md}\\ &= \sigma_{0x} + \psi_{DP}\Gamma_{DP} + \psi_d\Gamma_d - \beta m_{0,x}\psi_{0,x}\end{aligned}, \qquad 4.23$$

where:

$$\begin{aligned}\Gamma_{DP} &= \beta m_{0,x}\Pi_{DP} + \zeta\varepsilon_m \sinh(\zeta w)\\ \Gamma_d &= \beta m_{0,x}\Pi_d - \sqrt{\alpha\varepsilon_w\kappa_w}\cosh(\zeta w) - \zeta\varepsilon_m \sinh(\zeta w)\end{aligned}. \qquad 4.24$$

The potential balance equation is given by:

$$V_{GB} = V_{FBC} - \frac{f(\psi_s)}{C_{eff}} - \psi_0 + \psi_s, \qquad 4.25$$

where $f(\Psi_s)$ is given by equation 2.61. From the charge balance equation, we can relate the semiconductor charge (surface potential) to the quantity Ψ_d:

$$f(\psi_s) = -\sigma_f - \left(\sigma_{0x} + \psi_{DP}\Gamma_{DP} + \psi_d\Gamma_d - \beta m_{0,x}\psi_{0,x}\right). \qquad 4.26$$

Now, solving equations 4.14, 4.25, and 4.26, we get:

$$V_{GB} = V_{FB} + \left(\frac{\Pi_d}{\Gamma_d} - \frac{1}{C_{eff}} \right) f(\psi_s) + \psi_s , \qquad 4.27$$

where:

$$V_{FB} = V_{FBC} + \frac{\Pi_d}{\Gamma_d}\left(\sigma_f + \sigma_{ox} + \beta m_{0,x} \psi_{0,x} \right) - \left(\Pi_{DP} - \frac{\Pi_d \Gamma_{DP}}{\Gamma_d} \right) \psi_{DP} . \qquad 4.28$$

Equation 4.27 is a single equation involving the semiconductor surface potential Ψs. This equation can be solved numerically by iteration. However, what is more important is that equation 4.27 is identical to the format of the potential balance equation for a regular MOSFET structure, which is given by:

$$V_{GB} = V_{FB} - \frac{f(\psi_s)}{C_{ins}} + \psi_s . \qquad 4.29$$

Thus, one can see that the linear approximation of the BioFET is nothing more than a MOSFET, with the capacitance replaced by a series combination of capacitances, and with the flatband voltage shifted by an amount that depends on the surface parameters and the density of DNA molecules. Thus, all the approximate equations of the MOSFET can be used while maintaining the effect of the DNA probe density on the operation.

4.5 Comparison Between Models

In this section, the results of simulating the linearized model of the BioFET are compared against those obtained from the physical equations. The label "current" in figures 4.4-4.8 , as well as the term "sensitivity" used in this chapter, refer to the hybridization current, defined as in chapter 3 to be the difference in the drain current of a BioFET with and without hybridized DNA. The first curve to be compared is the sensitivity of the BioFET as a function of the density of DNA probes. Figure 4.4 shows simulation results of the sensitivity curves for both the exact and approximate models, for different amphoteric site densities. The main features of the curves are similar. However, for some values of amphoteric site densities, the linear model does not provide a good match with the exact model. This can be attributed to the poor approximation of the linear curves to the exact

adsorption curve, which can underestimate or overestimate the amount of shielding, depending on the scaling value used. This poor approximation can be seen in Figure 4.3a at the corners of the curve. At certain site densities, the errors due to the approximation of the pH adsorption curve are compensated by errors in the double layer calculations, due to the linearization of the hyperbolic sine curve. The compensation results in good agreement between the exact and approximate curves.

One can rectify the problem of poor pH adsorption curve approximation by scaling the slopes of the linear approximations, or by shifting them so that the linear approximation will always overestimate the adsorbed charge, thereby giving a more realistic value for pH sensitivity. Figure 4.5 shows sensitivity curves obtained by changing scaling values (α, δ, τ_1 and τ_2) to fit the exact curve. It is seen that the physical model can be approached by a careful selection of scaling values. However, it is important to note that the optimum selection of scaling values would generally change as the bias voltages are changed. Therefore, the general approach would be to choose constant values for the scaling values and specify a range of validity for these values.

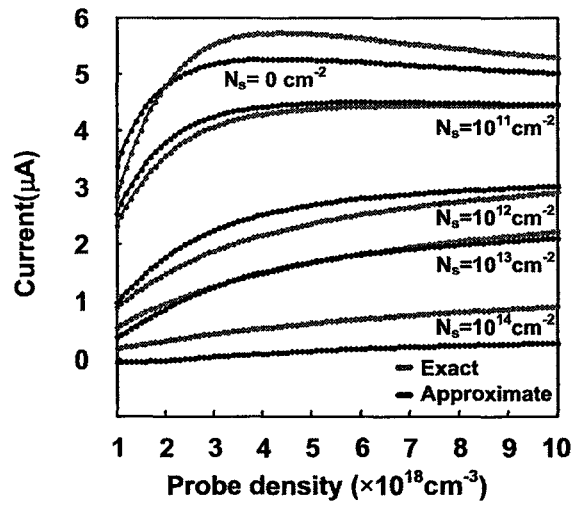

Figure 4.4 Comparison between the exact and approximate BioFET sensitivity curves

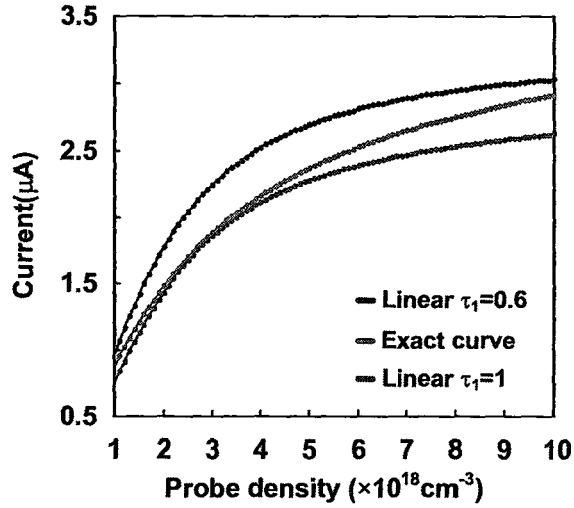

Figure 4.5 The effect of changing scaling values

Figures 4.6, 4.7, and 4.8 show simulation results of the response of the BioFET to DNA hybridization as the reference electrode, solution pH value, and ionic concentrations are changed, respectively. In Figure 4.6, the exact and approximate solution curves are almost identical, illustrating that the semiconductor's charge equation and I-V characteristics dominate the behavior of the BioFET, as no approximations were made to the semiconductor side of the system. The piecewise linear approximation of the adsorption curve in Figure 4.7, although poor, follows the physical curve and crudely represents the pH sensitivity of this simplified model. The ionic dependence curves agree for high enough ionic concentrations. At very low concentrations, different scaling values should be used to accommodate the change in the physical curves. All these figures demonstrate that the approximate model presented in this chapter is adequate to describe the response of the BioFET, without the need to compute integrals numerically.

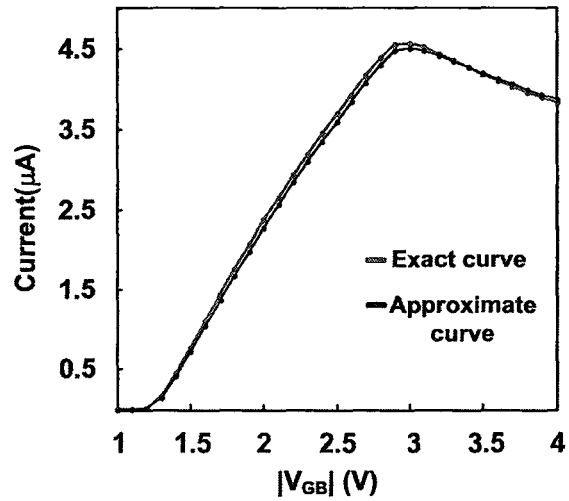

Figure 4.6 BioFET current as a function of the reference electrode potential

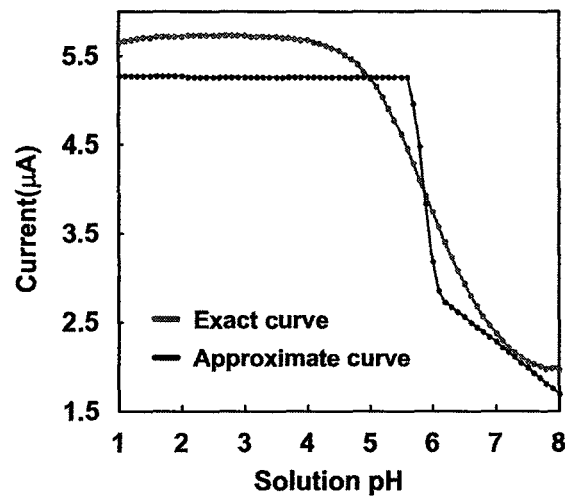

Figure 4.7 Exact vs. approximate pH sensitivity curves for the BioFET

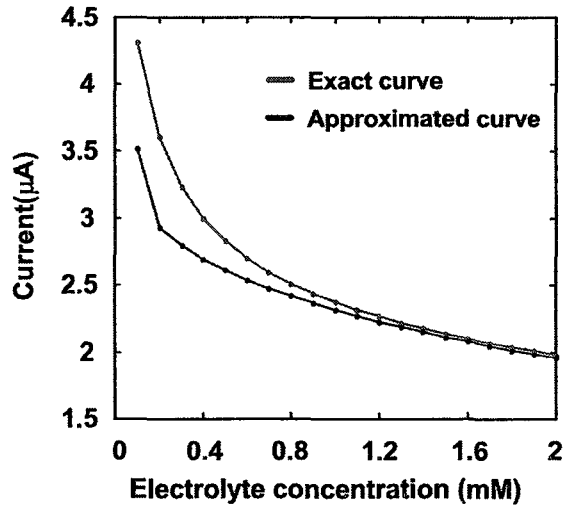

Figure 4.8 Exact vs. approximate effects of ionic concentration on sensitivity

4.6 Equivalent Circuit Model for the BioFET

In order to determine the influence of noise processes on the BioFET, it is essential that a linearized small-signal model be derived. The BioFET consists of many different regions, each with its own approximation of small signal equivalent circuit, and each with its own noise processes that characterize its operation. These regions are as follows:

1. The electrode-electrolyte interface
2. The bulk electrolyte
3. The electrolyte-insulator interface
4. The insulator-semiconductor interface

The equivalent circuit for an electrode-electrolyte circuit depends on the nature of this interface. In particular, the type of redox reactions that can occur, their reaction rates, density of reaction sites, ionic strength and work function differences affect the small signal impedance of this interface. Many different equivalent circuit models are used in the literature [48-51]. In all cases, however, the interface is characterized by a possible charge transfer resistance (R_{ct}), a double layer resistance (R_{dl}) and capacitance (C_{dl}), and a capacitance associated with the Stern layer (C_s). The placement of these elements is dependent on the interface and the type of redox reactions that occur. Figure 4.9 shows a

possible small-signal equivalent circuit for an electrode-electrolyte interface. The differential double layer capacitance can be estimated from the Gouy-Chapman model. Thus, the capacitance per unit area is given by:

$$C_{DL} = \left| \frac{d\sigma_{e-e}}{d\psi_{e-e}} \right| = \varepsilon_w \kappa_w \cosh\left(\frac{zq\phi(x)}{2kT} \right). \qquad 4.30$$

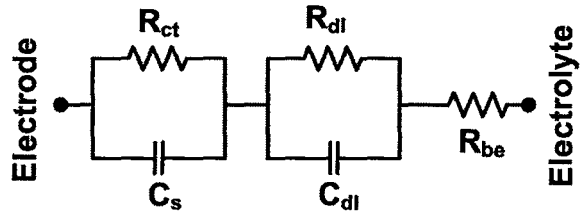

Figure 4.9 Equivalent circuit of a Faradaic electrode-electrolyte interface

This capacitance has a minimum value equal to that of an ideal capacitor with insulator thickness equal to the Debye length. However, that capacitance value is only at the potential of zero charge, and generally the capacitance will be much higher than that, owing to the nonlinear hyperbolic cosine term in equation 4.30. It is important to realize that the ideal Gouy-Chapman theory is seldom satisfied for general electrode-electrolyte interfaces, because specific adsorption causes different capacitance profiles at potentials far away from the pzc. However, equation 4.30 provides a good approximation of the AC capacitance over a range of applied bias potentials.

The Stern capacitance C_s is usually taken to be a constant [48]. This constant is interface dependent but the general accepted value is around 10-20 $\mu F/cm^2$ [37], [48]. Of course, the actual value of the Stern capacitance will depend on the interface and properties of the ions and solvent molecules, since the solvation shell and ionic radius determine how close the ions can be to the interface, and thus the Stern capacitance.

The double layer resistance R_{dl} is introduced because the ions in the double layer are mobile and can move under the influence of an applied potential, despite the fact that these ions are confined to the double layer region. This resistance is important when conducting AC measurements, as the resistance in the double layer can vary greatly from that in the bulk electrolyte. On one side, the excessive ionic density is expected to reduce

the resistance of the double layer. On the other hand, the closely packed structure severely hinders the mobility of the ions, increasing the resistance. The net result is that the resistance of the double layer can be very complicated and can be represented by a differential resistance element that spans the entire double layer length:

$$\begin{aligned} dR_{DL}(x) &= \frac{1}{\mu(x)\rho_{DL}(x)} \\ R_{DL} &= \int_0^L \frac{dx}{\mu(x)\rho_{DL}(x)} \end{aligned}, \qquad 4.31$$

where μ is the mobility of ions within the double layer ($cm^2/V.s$), and ρ_{DL} is the local volumetric charge density (cm^{-3}).

The charge transfer resistance is only available for Faradaic electrodes, where redox operations take place. The differential resistance value depends on the nature of the I-V relationship due to the redox reactions. For many electrode-electrolyte interfaces, the I-V relationship follows a Tafel relationship [31], which is defined by the following equation:

$$J = J_0 e^{-\alpha\beta(V-V_{eq})}, \qquad 4.32$$

where J is the current density (A/cm^2), α is a constant that depends on the redox reaction constant, V_{eq} is the potential of the interface at equilibrium (V), and β is the inverse thermal voltage (V^{-1}).

The bulk electrolyte can be seen as a continuum of charge carriers (ions). In a simple model, this can be seen as a constant resistance (R_{be}) that depends on the bulk concentration of the ions participating in current conduction. However, the simple model of conductivity for metals cannot be used here except for infinitely dilute solutions. The reason is that moving ions tend to interact with one another and affect the overall bulk mobility. An approximation of the dependence of the mobilities on the ionic concentration is given by Kohlrausch's law [3]:

$$\Lambda = \Lambda_\infty - A\sqrt{n_0}, \qquad 4.33$$

where Λ and Λ_∞ are the molar conductivities at the concentration n_0, and at an infinitely dilute solution, respectively, and A is a constant that depends on the valence of the conducting ions.

An additional frequency dependent term is often represented by the Warburg impedance [48]. However, as this dependence does not follow that of a reactive circuit element, it is not possible to model this impedance by an inductance or capacitance. In any case, the effect of this impedance is generally negligible at low frequencies [37], [48]. The electrolyte-insulator interface also has a DNA-modified double layer and would contribute to a variable capacitance. In addition, the adsorption of protons also represents a capacitance that contributes to the total electrolyte charge, and hence adds in parallel to the double layer capacitance. Just as in the metal-electrode interface, this interface also has a double layer resistance and a Stern capacitance. However, there will be no charge transfer resistance as no redox reactions can take place between the insulator and the electrolyte.

The final part in the equivalent circuit diagram is the FET structure, which, in saturation, can be replaced by the usual FET model of two transconductance elements, and an output resistance that models channel length modulation. Of course, higher frequency models would include a gate-drain capacitance and channel resistance as well. However, for biosensors, what is important is the low frequency, low voltage, and low power operation of the BioFET, and these nonidealities can be ignored. Figure 4.10 shows a complete equivalent circuit diagram of a saturated BioFET, including all of these effects. Such a circuit is useful in determining the noise contribution of the many different noise sources in the circuit.

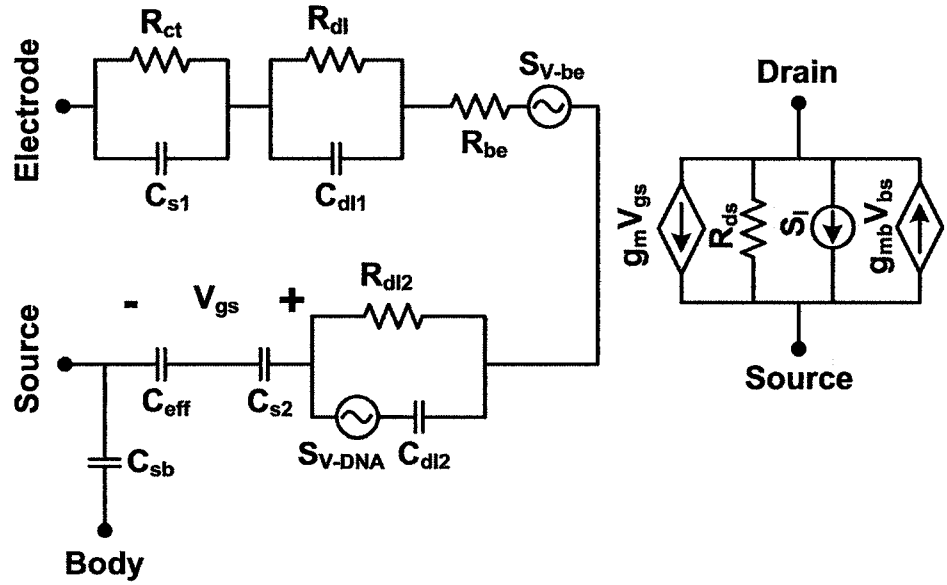

Figure 4.10 Complete small signal equivalent circuit diagram for the BioFET

4.7 Noise Analysis

So far, the sensitivity of the BioFET was investigated in light of the different possible phenomena that affect the change in the electrical current due to DNA hybridization. However, this is not the only limitation in the sensitivity. Random fluctuations can add uncertainty in the sensed signal. If the magnitude of these fluctuations is comparable to the change due to DNA hybridization, then the signal might get buried in the random fluctuations. In this section, the different device noise phenomena in the BioFET will be investigated, and quantitative analysis of the signal-to-noise ratio (SNR) of the BioFET will be given.

In physical systems, random noise is dealt with in a statistical framework. Generally, the analysis assumes that the random noise is a wide-sense stationary (WSS) process, implying a zero mean, and an autocorrelation function that only depends on the temporal spacing between two samples [52]. When the noise process satisfies these criteria, we can speak of a power spectral density for the noise process. As the signal to be sensed is inherently low-frequency (practically DC), we are mainly interested in the low-frequency spectrum of the noise spectral density. Components of higher frequency

can be easily dealt with by low-pass filtering, which is equivalent to signal averaging in the time domain.

The main sources of noise in the BioFET are the semiconductor's thermal and flicker noise, in addition to the bulk electrolyte noise, and the noise due to the redox reactions within the electrode-electrolyte interface [48]. The source of the semiconductor's thermal noise is the random motion of current conducting carriers throughout the channel. The amount of current noise due to thermal fluctuations is a function of the total number of charge carriers in the channel. A model that predicts this fluctuation is given by the following equation [36]:

$$S_I(f) = 4kT\frac{\mu}{L^2}(\mp Q_I), \qquad 4.34$$

where S_I is the drain current noise spectral density (A^2/Hz), and Q_I is the total inversion charge in the semiconductor channel (C). Although equation 4.34 is quite simple in formulation, evaluation of the total inversion charge is not a simple task, since the variation of the inversion charge is not linear along the length of the channel. An overestimate of the thermal noise can be calculated by assuming that the inversion charge at the entire channel is equal to that at the source. However, this will provide poor results in deep saturation and will only be valid under extremely low drain-source biases.

Flicker (or $1/f$) noise is common in many different electronic devices. It dominates the total low-frequency noise power for electronic systems, particularly for analog circuits [53], [54]. Its origins remain somewhat of a controversy between different schools of thought. The two theories are the number fluctuation theory (ΔN) and the mobility fluctuation theory ($\Delta\mu$) [54], [55]. Both theories predict a noise spectrum that varies inversely with the frequency, hence the name $1/f$ noise [56]. However, they differ in their interpretation of the origins of the noise. The number fluctuation theory (also known as the McWhorter theory) postulates that flicker noise is primarily a surface effect, caused by quantum tunneling of charge carriers into nearby traps within the insulator material. By assuming a capture time constant that varies inversely with the distance from the insulator-semiconductor interface, and a trap density that varies exponentially with depth

and energy, it is possible to arrive at the expected $1/f$ spectrum [57]. The variation in noise spectral densities due to hot carrier degradation and irradiation demonstrate that surface traps do indeed contribute to the flicker noise [55]. On the other hand, the mobility fluctuation theory attributes the noise behavior to fluctuations in the carriers' mobilities rather than their numbers. Analysis of this theory [57] leads to a spectrum that varies inversely with the frequency as well. This model, however, explains the bias dependence of the noise spectral density, which is observed experimentally.

To accommodate both theories into a single framework, a correlated number-mobility theory (ΔN-$\Delta\mu$) for flicker noise is sometimes used. The main reasoning behind this correlation is the argument that trapped carriers can act as Coulombic scattering centers for the mobile carriers. Thus, a change in the number of carriers due to capture will also induce a change in the mobility of the uncaptured carriers [56-59]. A model for the correlated number-mobility theory is given by:

$$S_I(f) = \frac{q^2 kT\lambda N_t}{WLC_{eff}^2 f}\left(g_m + \alpha\mu_{eff}C_{eff}I_D\right)^2, \qquad 4.35$$

where λ is the tunneling depth of the carriers onto the insulator's surface (cm), α is the scattering coefficient (V.s/C), and N_t is the effective trapping density per unit energy ($cm^{-3}J^{-1}$).

The third source of device noise is the noise coming from the random ionic motion within the bulk electrolyte. This noise can be significant compared to the thermal noise of the FET channel, since electrolytes generally have high resistivities. If the conductivity of the bulk electrolyte is known (from equation 4.33), then the total noise spectral density is given by the following Johnson-Nyquist white noise formula:

$$S_I(f) = \frac{4kT}{R}, \qquad 4.36$$

where R is the total resistance of the bulk electrolyte (Ω).

The electrode-electrolyte interface, which has to be Faradaic for the BioFET [48], can contribute to the noise in the system. The spectral density of this interface varies, depending on the relative speed of the redox process with respect to that of the

surrounding circuit [48]. However, this spectral density is always proportional to the average amount of current that flows. In a BioFET, since there is no DC current flowing through the structure, this interface is not expected to contribute any noise to the drain current.

A final source of noise in BioFETs is that resulting from the random motion of immobilized oligonucleotides [39]. This random motion of charged macromolecules is expected to couple to the mobile charges in the semiconductor channel, causing random fluctuations that appear as noise in the output current. Although a model for this motion has not been developed, some general characteristics of this noise can be predicted. Firstly, it is expected that the motion of the DNA molecules is confined to the lateral dimension, along the length and width axes of the FET channel. This is due to the DNA immobilization on the insulator surface, which would inhibit their vertical diffusion. This would mean that the effect of the DNA particles moving is to change the charge concentration profile in the channel. If the noise spectral density of the DNA molecules is white, so will be the noise of the semiconductor channel carriers. Moreover, it is expected that under high enough electrode potentials, the mobility of the DNA molecules will be lowered, since their mobility will be hindered with the thicker double layer in which they are immersed. Finally, high electrolytic concentrations can reduce the amount of noise coupled to the FET, by virtue of the screening charge, which efficiently screens out the charges at the loose DNA strand ends. This would shield the channel carriers of the underlying FET from the modulation effects due to the motion of that section of the DNA.

4.8 Optimum SNR

Given the sources of noise of the BioFET, as well as the model equations for the BioFET signal, we have all the information needed to numerically calculate the SNR of the biosensor. The signal to noise ratio is defined by:

$$SNR = 10\log\left(\frac{(\delta I_D)^2}{\sum_n S_{I,n}}\right), \tag{4.37}$$

where δI_D is the BioFET hybridization current change, and $S_{I,n}$ is the n-th contribution of noise processes to the drain current. Figure 4.11 shows the simulated SNR value of a BioFET with a size of (25×1μm) as a function of the gate bias. It can be seen that the SNR value drops below 0dB for low enough DNA concentrations. In addition, it is clear that there is a bias point at which the SNR is maximized for the BioFET. This point corresponds to values around moderate inversion. Higher bias values will hinder the sensitivity because of the mobility degradation. Given that hybridization only changes the threshold voltage, as given by equation 4.28, the maximum BioFET sensitivity would be achieved at the point of highest transconductance. However, the point of maximum SNR can deviate from this, as the noise scales with the transconductance of the device. We can investigate the optimum noise location by assuming strong inversion and using the analytic model of a saturated MOSFET, given by:

$$I_D = \frac{K}{2\left(1+\theta\left(V_{GS}-V_T\right)\right)}\left(V_{GS}-V_T\right)^2\left(1+\lambda V_{DS}\right), \tag{4.38}$$

where θ is the bulk mobility degradation factor (V^{-1}), V_T is the threshold voltage (V), and λ is the channel length modulation factor (V^{-1}). The SNR of the BioFET will be given by:

$$SNR = 10\log\left(\frac{(\delta V_T)^2}{S_{VFB}\left(1+\alpha\mu_{eff}C_{eff}\frac{I_D}{g_m}\right)^2}\right), \tag{4.39}$$

where:

$$S_{VFB} = \frac{q^2 kT\lambda N_t}{WLC_{eff}^2 f}. \tag{4.40}$$

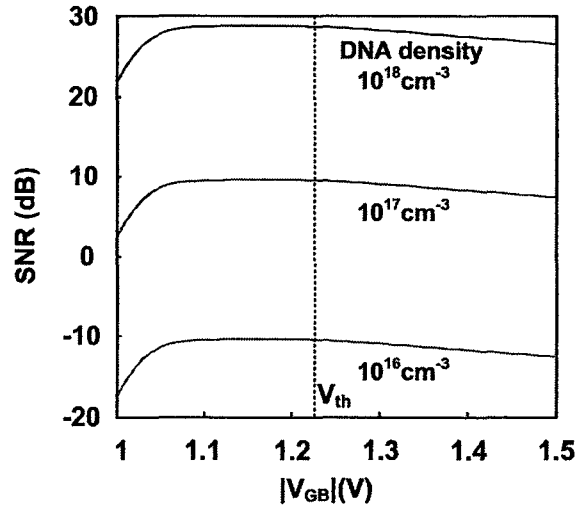

Figure 4.11 The effect of bias point on the SNR of the BioFET

The quantity inside the brackets of equation 4.39 should be maximized with respect to the gate bias. Differentiating this quantity and equating the result to zero yields:

$$\frac{d}{dx}\left(\frac{\mu_{eff} I_D}{g_m}\right)=0, \qquad 4.41$$

and since the transconductance is given by:

$$g_m=\frac{\delta I_D}{\delta V_{GS}}, \qquad 4.42$$

we can make the appropriate substitutions for equation 4.41, eventually arriving at the following:

$$\frac{d}{dV_{GS}}\left(\frac{\mu_0(V_{GS}-V_T)}{(2+\theta(V_{GS}-V_T))}\right)=0. \qquad 4.43$$

Equation 4.43 has no solution for finite values of V_{GS}. Thus, the value for maximum SNR must be below threshold. Determining the exact value analytically requires using a closed form solution for the subthreshold equation, and will not be addressed here. However, it will suffice to state that the optimum biasing point for maximum SNR is expected to be in the subthreshold regime.

The point of maximum SNR is expected to vary with any variation in the threshold voltage of the device. From equation 4.28, we can see that essentially all the

different parameters of the BioFET affect the value of the threshold voltage, and therefore the point of maximum SNR will drift as well. Figure 4.12 and 4.13 show normalized simulation results of the SNR curve with varying electrolyte concentration and body bias, respectively, confirming these expectations.

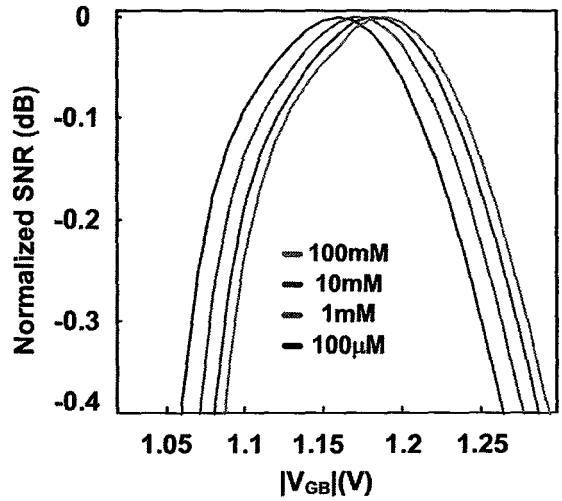

Figure 4.12 Effect of ionic density on maximum SNR point

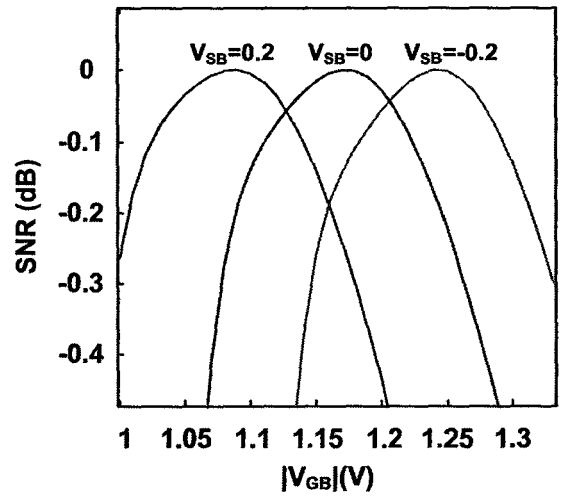

Figure 4.13 The effect of body biasing on maximum SNR point

4.9 Conclusion

The approximations made in this chapter enabled us to arrive at an analytic expression for the effect of the hybridized DNA molecules on the threshold voltage of the BioFET. Such

a model can be incorporated into circuit simulators such that the response of the BioFET can be coupled with different interface circuits to arrive at a sensitive DNA sensing cell, from which electronic microarrays can be constructed. Noise analysis was performed on the BioFET, including the bulk electrolyte noise and that of the semiconductor's channel. It was seen that an optimum biasing point in moderate inversion will allow for maximum SNR value to be achieved. This is particularly important when sensing extremely low density of DNA molecules. The next chapter is concerned with the analysis of different interface circuits that can be used for constructing sensitive DNA microarray cells, as well as the design procedure for a fully integrated DNA microarray chip in 0.8μm CMOS technology.

Chapter 5

DESIGN OF DNA SENSOR CIRCUITS

5.1 Introduction

The BioFET presents an excellent candidate for direct electrical sensing of DNA hybridization. However, its main advantage over other label-free techniques is that it is readily compatible with CMOS processing. This allows for the implementation of the sensors, as well as all the needed interface circuitry, on the same chip. The BioFET can be incorporated into many different kinds of sensor circuits and readout interfaces. As such, one can interface the BioFET to different amplifier circuits and enhance many different aspects of the BioFET's characteristics, including the sensitivity, linearity, noise immunity, temperature sensitivity, and output resistance.

In this chapter, several different circuit configurations for sensing DNA hybridization with the BioFET will be given. This will include utilization of the potentiometric, amperometric and C-V properties of the BioFET. The sensitivity of these circuits to DNA hybridization will be determined, and possibility of integration into microarrays will be investigated. The final part of this chapter will describe in detail the design of a DNA microarray chip in standard CMOS 0.8μm technology.

5.2 Methods of Sensing

From the previous chapter, it was seen that DNA hybridization causes a shift in the threshold voltage of the BioFET. This shift is equivalent to a change in the voltage of the reference electrode. For constant biasing, the change in the threshold voltage causes a

change in the amount of drain current, via the transconductance of the BioFET. In addition, the threshold change in the BioFET causes a shift in the C-V characteristics. These three characteristics of the BioFET sensor allow us to determine three different sensor circuit families:

1. Potentiometric sensors: These sensors aim at sensing the change in the threshold voltage by maintaining a constant current for the drain of the BioFET, while measuring the shift in the gate-source voltage (V_{GS}) directly via a high input impedance readout circuit, such as an operational amplifier. These sensors can offer better linearity in measurements, as the output can be fed to linear amplifiers for sensitivity enhancement. Another characteristic of this type of sensor is that the sensitivity is only limited by the limits of validity of the one dimensional solution, and not by the device sizing.
2. Amperometric sensors: In this regime, the change in the current of the BioFET due to DNA hybridization is sensed while V_{GS} is kept constant. If the BioFET is in the linear region of operation, the sensor works as a resistance sensor, monitoring the change in the channel resistance as the DNA is immobilized. In saturation, amperometric sensors would be equivalent to common-source amplifiers, offering a high degree of sensitivity to hybridization. Higher aspect ratios of the BioFET will, in general, cause higher sensitivities due to the higher transconductance values. However, the output resistance can also be lowered by this, and a compromise must be made to maintain a high sensitivity value.
3. Capacitance sensors: The change in the small signal capacitance due to a shift in the threshold voltage can affect the operation of different AC circuits, particularly amplifiers and oscillators. DNA hybridization can, therefore, change the oscillation frequency of an oscillator or the gain of an amplifier. The sensitivity of the capacitance due to the DNA hybridization scales as the area of the BioFET, which might be somewhat of a disadvantage in terms of miniaturization.

Many different interface circuits have been proposed for the ISFET [60], [61], [62], which are equally applicable to the BioFET. These include both potentiometric and

amperometric sensors. However, these circuits are generally concerned with the interfacing to the BioFET, and not with the actual sensitivity of the device. The following sections will address some general techniques that can be used to enhance the sensitivity of a BioFET sensing circuit. The more sensitive a circuit is, the more possible it is to reduce the density of DNA probes, thereby allowing the sensor to detect very dilute concentrations of the DNA molecules, perhaps even at the concentrations that are available in raw samples.

One issue of concern is whether to use a p-type or n-type BioFET. In terms of sensitivity, it is expected that the n-type BioFETs will provide better sensitivity for a particular device size, due to the high mobility of the charge carriers (electrons) in the channel, leading to higher transconductance values. On the other hand, p-type sensors are known to have better noise performance. In addition, providing negative bias to the reference electrode of p-type BioFETs can reduce the amount of positive adsorbed electrolyte ions from the electrolyte-insulator interface [63]. This would cause the inhibition of secondary charge-screening effects and allow for enhanced sensitivity. Many of the circuits can be substituted with an equivalent BioFET of the complementary type. The circuit analysis will not change, but the sensitivity and noise performance might vary based on the effects of these different phenomena.

5.2.1 Common-source Configurations

The simplest technique for a BioFET sensor is to use a saturated BioFET with a saturated active load. This is shown schematically in Figure 5.1. This way, the intrinsic amplification capability of the BioFET is utilized. The output voltage change due to hybridization is given by:

$$\frac{\Delta V_{out}}{\Delta V_{T,DNA}} = g_m \left(r_1 // r_2 \right), \qquad 5.1$$

where $\Delta V_{T,DNA}$ is the change in the threshold voltage of the BioFET due to DNA hybridization (V), g_m is the transconductance of the saturated BioFET (Ω^{-1}), and r_1 and r_2 are the output resistances of the BioFET and load transistor, respectively (Ω). Equation

5.1 gives the standard amplification expected from a single stage common-source amplifier, showing that the amplification, and therefore, sensitivity, of the circuit depends on the transconductance and the output resistances of both the load and BioFET. It would, therefore, be desirable to operate the circuit at a point with maximum gain, which is close to the threshold voltage of MOS transistors. It is important to realize that the point of maximum transconductance is not necessarily the same point of maximum gain for the common source amplifier. This is because the output resistances are also bias-dependent. A simplified calculation, similar to that done in the previous chapter, will show that the point of optimum gain would occur somewhere below the threshold, meaning that subthreshold biasing conditions are preferred for higher sensitivity.

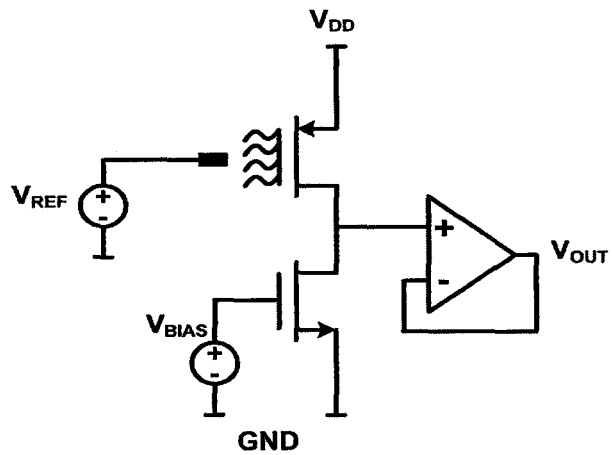

Figure 5.1 Common-source BioFET amplifier

One of the main disadvantages of the circuit of Figure 5.1 is that the high impedance output node can couple noise easily, and this will be read at the output, distorting the original intended signal. In addition, the constant bias required for the load transistor is critical in determining the operation of the circuit and must not drift with temperature or other factors. This can be accomplished using voltage references, which require a lot of components and take considerable amount of space in the chip. However, one method of rectifying this problem is by providing the bias for the load from within the circuit in a closed loop fashion. Figure 5.2a shows an implementation of this idea [64]. The small-signal equivalent circuit is given in Figure 5.2b, and the gain is given by:

$$\frac{\Delta V_{out}}{\Delta V_{T,DNA}} = \frac{g_{m1}A(r_1 // r_2)}{1+g_{m2}A(r_1 // r_2)} \approx \frac{g_{m1}}{g_{m2}}, \qquad 5.2$$

where A is the open-loop gain of the operational amplifier. Equation 5.2 shows that the gain no longer depends on the output load resistances but rather on the transconductance of the load, whose inverse is generally smaller than that of the load resistances. This will cause the gain of the device to be lowered. However, the biasing of the load will be set such that $V_{o1}=V_{bias}$. This is an example of a case where sensitivity is sacrificed for other performance parameters, in this case being ease of implementation.

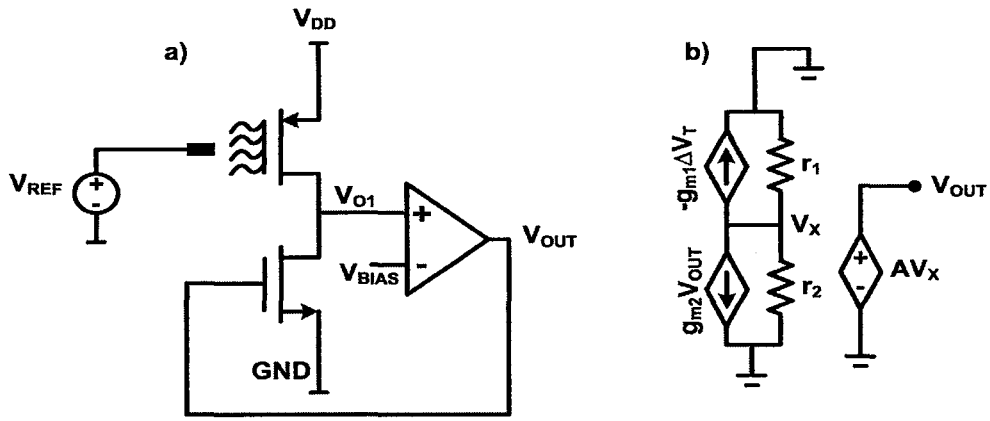

Figure 5.2 a) Common source with feedback sensor circuit, and b) small-signal equivalent circuit

Variations to the circuit of Figure 5.2 are shown in Figures 5.3a, and 5.3b. In these figures, the sensitivity of the circuit is enhanced by increasing the output resistance of the load transistor by stacking, and by weakening the feedback signal, respectively. These two designs provide controllability over the sensitivity/stability tradeoff of the circuit. Figure 5.3a is not very suitable for low voltage operations, due to the stacking of the transistors, while Figure 5.3b can consume a lot of design space, due to the resistors involved. However, for discrete applications, these topologies can be useful in investigating the effects of different circuit configurations and tradeoffs in the performance of the circuits. The small signal equivalent diagrams of the circuits in Figure 5.3 are given in Figure 5.4. The sensitivity for the circuit of Figure 5.3a is given by:

$$\frac{\Delta V_{out}}{\Delta V_{T,DNA}} = \frac{g_{m1}A(r_1 // r_2)}{1+g_{m2}A(r_1 // r_2)(R_2/(R_1+R_2))} \approx \frac{g_{m1}}{g_{m2}}\left(\frac{R_1+R_2}{R_2}\right), \qquad 5.3$$

and the sensitivity of the circuit in Figure 5.3b is given by:

$$\frac{\Delta V_{out}}{\Delta V_{T,DNA}} = g_{m1}A(R_X // R_Y // R_Z) \approx \frac{g_{m1}}{g_{m2}}\left(1+(r_{n2}/r_{n1})+(g_{m2}+g_{m2b})r_{n2}\right), \qquad 5.4$$

where:

$$\begin{aligned} R_X &= r_p \\ R_Y &= r_{n1}+r_{n2}+(g_{m2}+g_{m2b})r_{n1}r_{n2} \\ R_Z &= \frac{1+(r_{n2}/r_{n1})+(g_{m2}+g_{m2b})r_{n2}}{g_{m2}A} \end{aligned} \qquad 5.5$$

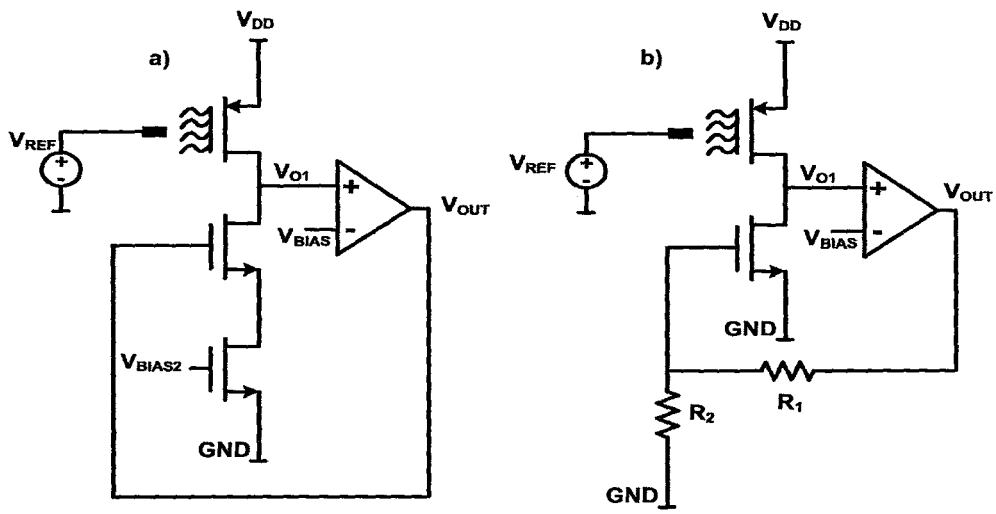

Figure 5.3 a) Common source with feedback and stacked load, and b) weak feedback circuit

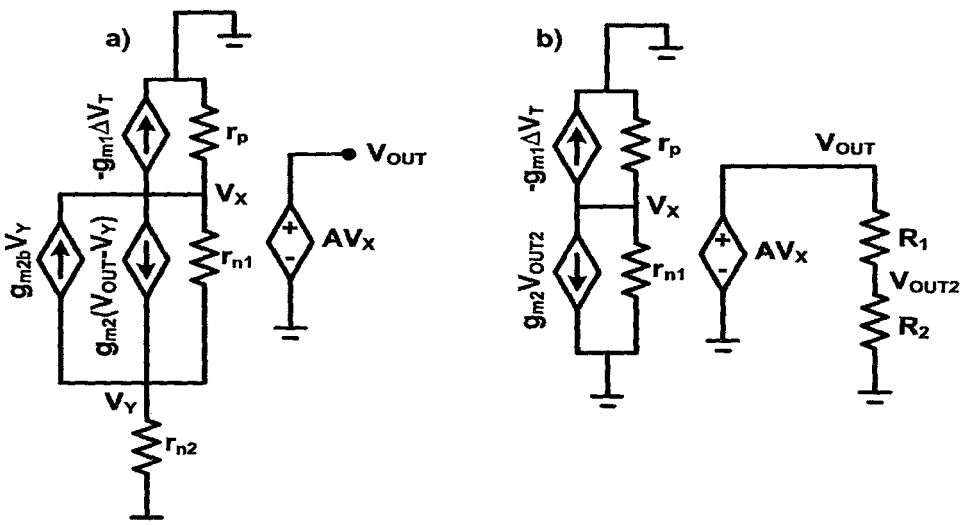

Figure 5.4 Small-signal equivalent circuits of Figure 5.3

Figure 5.5 shows another sensor circuit that uses two complementary BioFET devices, configured as a CMOS inverter. The effect of DNA hybridization in this sensor would be similar to that of a push-pull configuration. This would offer higher sensitivity compared to a single BioFET configuration when both devices are saturated. Essentially, the circuit has to operate at the point that corresponds to the "forbidden" region of operation for a digital CMOS inverter. Under this condition, the sensitivity of the circuit is given by:

$$\frac{\Delta V_{out}}{\Delta V_{T,DNA}} = (g_{m1} + g_{m2})(r_1 // r_2). \qquad 5.6$$

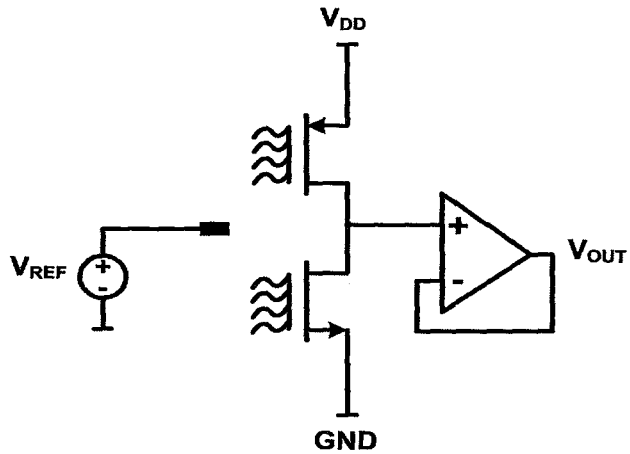

Figure 5.5 Complementary BioFET sensor

As with the single common source BioFET configurations, maintaining a constant bias is critical, since the output of the sensor circuit is at high impedance, and will drift easily with slight fluctuations in the bias of the reference electrode. A feedback system can be used to rectify this problem. The circuit is given in Figure 5.6a. The small-signal equivalent circuit is given by figure 5.6b, and a simple analysis shows that:

$$\frac{\Delta V_{out}}{\Delta V_{T,DNA}} = \frac{(g_{m1} + g_{m2})A(r_1 // r_2)}{1 + (g_{m1} + g_{m2})A(r_1 // r_2)} \approx 1. \qquad 5.7$$

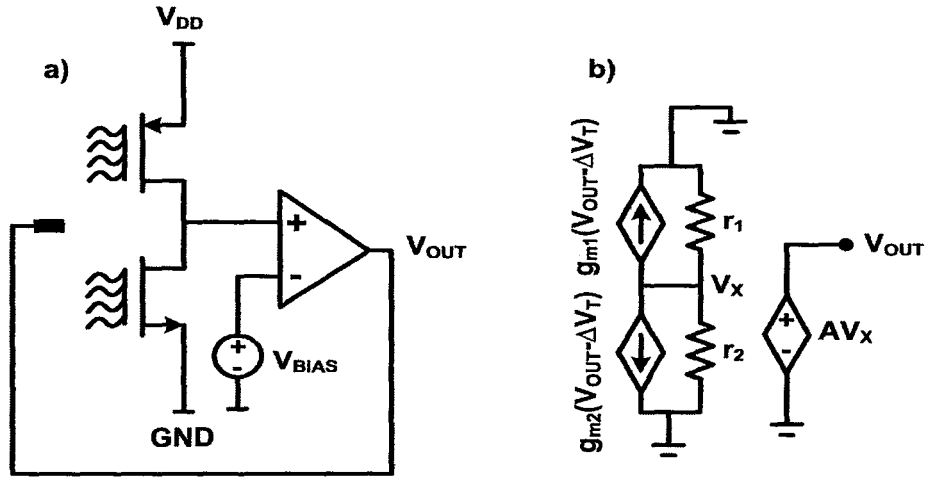

Figure 5.6 a) Complementary biosensor with feedback, and b) small-signal equivalent circuit

Equation 5.7 shows that, although the circuit of Figure 5.6 might be very stable due to the negative feedback, it does not provide high sensitivity. However, if we provide a weaker feedback using a voltage divider, then the gain will be given by:

$$\frac{\Delta V_{out}}{\Delta V_{T,DNA}} = \frac{(g_{m1}+g_{m2})A(r_1 // r_2)}{1+(g_{m1}+g_{m2})A(r_1 // r_2)(R_2/(R_1+R_2))} \approx \frac{R_1+R_2}{R_2}. \qquad 5.8$$

Thus, unlike the previous cases, the sensitivity of the circuit is now independent of the transconductances of the BioFETs, which means that now we can use BioFETs of minimum possible sizing, as long as the 1-D model still applies.

5.2.2 Operational Amplifier Integration

In conventional microarray cells, the brightness of the light is an indication of the degree of hybridization in a particular cell. It is important for this data to be distortion-free. This requires the response of the cell to be as linear as possible. In the BioFET, the relationship between the hybridized DNA density and the response is highly nonlinear. The main source of nonlinearity comes from the quadratic relationship of the saturation-mode FET equations. Feedback can be used to provide higher linearity ranges, but the trade-off is a reduction in the gain. However, if the BioFET were to be part of a high gain circuit, such as a differential amplifier, or an operational amplifier, then the gain can be traded off for a bigger dynamic range using resistive negative feedback. This leads to a possible

realization of a BioFET sensor by replacing the internal differential MOSFET transistors with BioFETs. This is shown schematically in Figure 5.7, in which a two-stage CMOS operational amplifier is used as a DNA hybridization sensor. The advantage of this design is that temperature effects on the operation of the MOSFET transistors are rejected by the differential pair. In addition, the high gain of the circuit allows negative feedback to be introduced without losing a lot of sensitivity. The effect of DNA hybridization can be modeled as an offset voltage that is introduced to an ideal operational amplifier. This is shown in Figure 5.8. The analysis of this circuit is simple, with the sensitivity given by:

$$\frac{\Delta V_{out}}{\Delta V_{T,DNA}} = \left(1 + \frac{R_2}{R_1}\right). \qquad 5.9$$

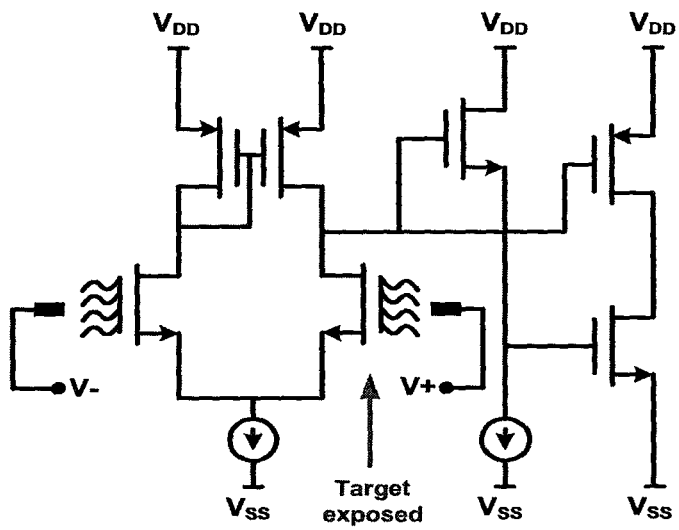

Figure 5.7 BioFET operational amplifier

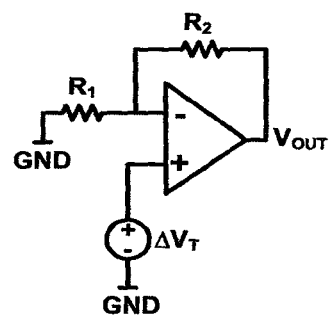

Figure 5.8 BioFET op-amp in noninverting configuration

Although high sensitivities can be achieved from this circuit, there are a few problems that this circuit may cause. Firstly, the internal offset voltage of the operational amplifier will be amplified as well, leading to an offset in the output voltage that is not due to hybridization. If this offset voltage is not known, it cannot be subtracted from the output signal. There are many techniques for offset cancellation. However, many of them rely on precharging capacitors with the offset voltage and then subtracting the offset at measurement time. Such techniques are not useful with DNA detection because of the large time constants for the signals. Other techniques for offset cancellation use cancellation resistors placed at the differential stage. Although these techniques are suitable for discrete implementations, they are not practical for microarrays with thousands of amplifiers.

One more issue that arises with the direct use of operational amplifiers is that both input transistors must be replaced by BioFETs. This will allow for the reduction of temperature effects on the response of the electrolytic phase (for example, proton adsorption). In addition, replacing the transistor with a BioFET will change its threshold voltage. This change must be balanced by equal change in the mirror transistor; otherwise, significant offset voltage will appear even in absence of DNA hybridization. Both transistors must be DNA functionalized. However, only one of them should be subject to target DNA. This requires two separate electrolytic compartments and reference electrodes, which makes the design of DNA microarrays much more complex.

5.2.3 Positive Feedback

In the examples above, the maximum possible sensitivity for a single stage BioFET circuit is limited by the transconductance of the BioFET, and its saturated output impedance. However, if a positive feedback were incorporated into the operation of the circuit, but in a way that does not lead to a saturated output, then the sensitivity of the circuit can be enhanced. Figure 5.9 shows a block diagram of a system with positive feedback. The transfer function of this system is given by:

$$\frac{V_{out}}{V_{IN}} = \frac{A}{1 - A\beta}. \tag{5.10}$$

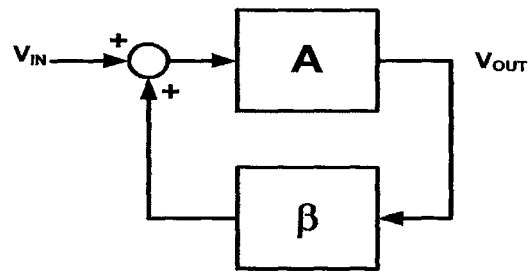

Figure 5.9 Block diagram of a positive feedback system

Thus, if the product $A\beta$ is positive and less than unity, the sensitivity of the circuit can be enhanced. A simple circuit that illustrates the use of positive feedback is given in Figure 5.10a. In this circuit, the positive feedback is implemented via a connection to the body of the BioFET, utilizing the body effect. Transistor M_{N1} must operate in deep linear region. This would enhance the linearity of the response, and guard against forward-biasing the body-source junction of the BioFET. The small-signal analysis of this sensor circuit is given with the aid of Figure 5.10b. The gain is given by:

$$\frac{\Delta V_{out}}{\Delta V_{T,DNA}} = \frac{g_m(r_1 // r_2)}{1 - g_{md}g_b(r_{ds} // r_3)(r_1 // r_2)}, \tag{5.11}$$

with the condition for stable and sensitive operation given by:

$$0 < g_{md}g_b(r_{ds} // r_3)(r_1 // r_2) < 1. \tag{5.12}$$

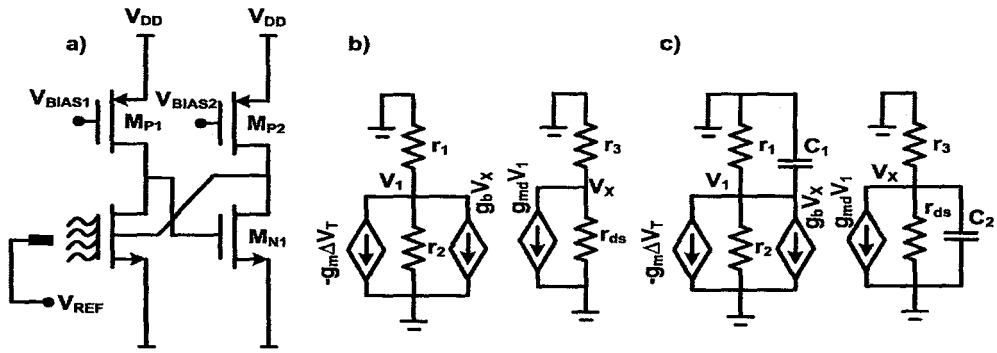

Figure 5.10 a) Positive feedback biosensor, b) small-signal equivalent circuit, and c) medium frequency equivalent circuit

Due to the existence of a positive feedback in this circuit, we need to investigate the possibility of oscillation. To do this, we consider the frequency-dependent equivalent circuit of Figure 5.10c. The capacitances consist of the lumped equivalent capacitance at the specific node, including parasitic capacitances from all connected devices. The Barkhausen condition for oscillation of this circuit is given by:

$$\frac{g_{md}g_b(r_{ds}//r_3)(r_1//r_2)}{[1+sC_1(r_1//r_2)][1+sC_2(r_{ds}//r_3)]}=1. \qquad 5.13$$

The phase criteria of equation 5.13 cannot be satisfied at any nonzero frequency. We therefore conclude that this circuit will not oscillate.

Another technique that derives from the concept of positive feedback is realized through negative resistances. Figure 5.11 shows a diagram of the I_D-V_{DS} curve for a BioFET, as well as that for a nonlinear load with a range of negative resistance. If the slope of the saturated part of the BioFET is parallel to the slope of the negative resistance, we will have a circuit that produces practically infinite gain over some region of operation. An example of a circuit which can provide a load curve as shown in Figure 5.11 is a cross-coupled saturated MOS transistor pair. Given the proper sizing and operating conditions, we can achieve very high sensitivities with very few devices. A global negative feedback can be used to trade some of this gain for better stability.

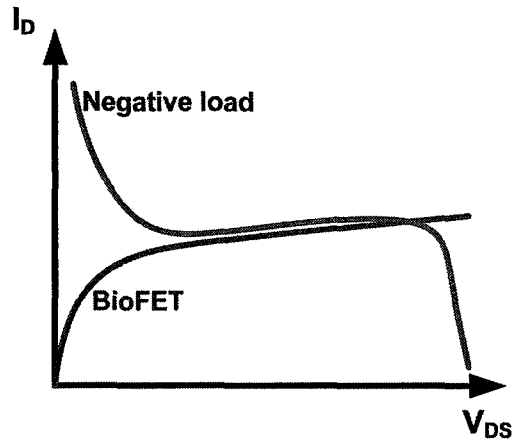

Figure 5.11 Plot of the I_D-V_{DS} relationship for a FET transistor and a negative resistance load

Figure 5.12a shows a schematic diagram of a cross-coupled negative resistance based DNA sensor circuit. Biasing of the negative resistance pair is provided by the BioFET

and transistor M_{N1}. If all the devices are saturated, circuit analysis of the small-signal model of Figure 5.12b yields:

$$\frac{\Delta V_{out}}{\Delta V_{T,DNA}} = \frac{g_{m4}(r_2 // r_4)}{1 - g_{m1}g_{m2}(r_1 // r_3)(r_2 // r_4)}, \qquad 5.14$$

which is very similar to the format of equation 5.11. In this case, however, care should be taken that Q-point of the output must lie in the negative part of the load curve and must be stable at that point. If the curves intersect in more than one point, as shown in Figure 5.13, then it is not possible to determine at which point the output will be. We might have to introduce a parallel resistance to the BioFET to force its curve to intersect with only one point of the load curve, such that the operation of the circuit is stable. Finally, negative feedback can be introduced at the reference electrode, or at the gate of the biasing transistor M_{N1}, for enhanced stability of biasing voltages.

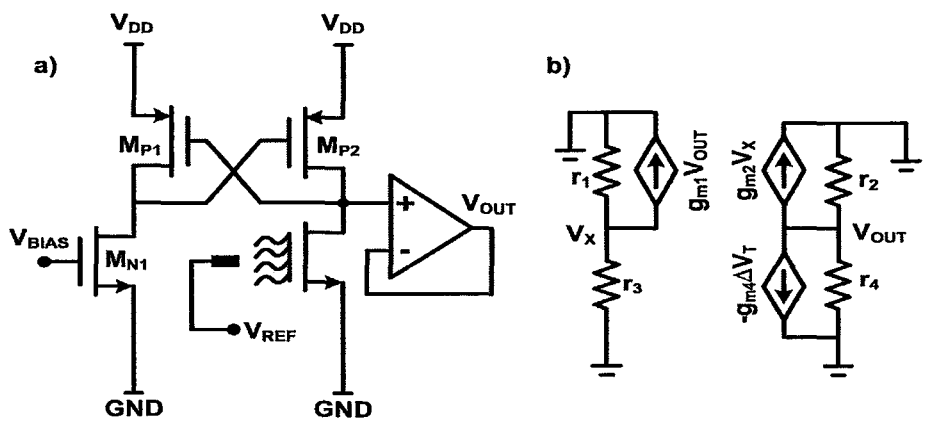

Figure 5.12 a) BioFET sensor circuit with negative resistance load, and b) small-signal equivalent circuit

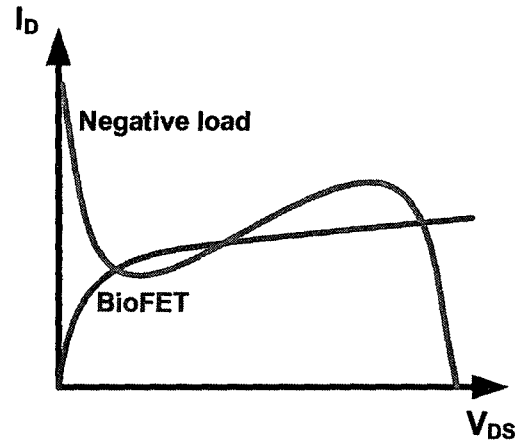

Figure 5.13 Example of unstable configuration for the circuit of Figure 5.12

5.2.4 Impedance Based Techniques

As hybridization of the DNA causes a shift in the threshold voltage of the BioFET, it is expected that the gate-source capacitance will be affected as well. This effect will be very clear around weak and moderate inversion regions, and less effective in strong inversion, where the capacitance approaches that of the gate insulator. The small-signal capacitance can vary different properties of AC circuits, such as the cutoff frequency of filters, or the frequency of oscillation for oscillators. The change in the oscillation frequency is appealing for DNA hybridization, as the signal to be sensed is very low in frequency (practically DC). Thus, extremely small changes in frequency, due to changes in the capacitance, can be monitored over a long period of time using digital counters. The number of pulses recorded in a fixed period of time will be an indication of the amount of DNA hybridization. This technique requires a lot of auxiliary circuits, including counters, signal conditioning circuits, and precision timer circuits. However, the sensitivity of this type of sensor can be very high, because the signal information is transferred to information in time, which can be sensed efficiently, given a long enough sampling period.

An example of an oscillator that can be used is the ring oscillator. Shown in Figure 5.14, the ring oscillator consists of an odd number of digital inverters, connected

in series. The propagation delay in these logic gates, which comes about due to the parasitic capacitances and resistances of the circuit, cause the circuit to behave in a bistable manner, oscillating between the rail voltages. Such large signal behavior will not be very useful for detecting changes in the small-signal capacitances. However, if we operate the ring oscillator as a small-signal oscillator, and we read the output using a thresholding operational amplifier, we will be able to sense the changes in the small-signal capacitance, and hence the amount of DNA hybridization.

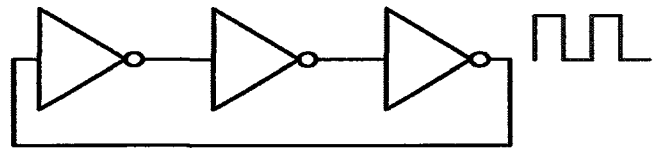

Figure 5.14 Ring oscillator circuit

The sensor circuit is given in Figure 5.15a. One stage of the ring oscillator is loaded with the BioFET. The bias of the body of the BioFET is allowed to change such that the point of maximum capacitance change can be set. The output of the ring oscillator is connected to an operational amplifier, which compares the voltage from the ring oscillator to the stable Q-point of the ring oscillator, which is set by an inverter with the input and output terminals shorted together. In essence, the operational amplifier converts any small-signal oscillation in the ring oscillator to a digital output.

The supply voltage must be chosen such that the ring oscillator will not oscillate in a rail-to-rail large-signal mode, but rather as small-signal oscillations about the stable Q-point. For this, the Barkhausen criteria must be satisfied, with the loop gain being equal to unity, and zero phase shift around the loop. If the loop gain is larger than unity, then the ring oscillator will oscillate in a rail-to-rail mode. Assuming saturated transistors, and assuming that the capacitance of the BioFET is much larger than the capacitances of the other transistors at node A, we can derive the equation for the loop gain with the aid of Figure 5.15b. The expression is given by:

$$\frac{-\left(g_{mp}+g_{mn}\right)^3 (r_1 // r_2)^3}{(1+sC_1(r_1 // r_2))^2 (1+sC_b(r_1 // r_2))} = 1. \qquad 5.16$$

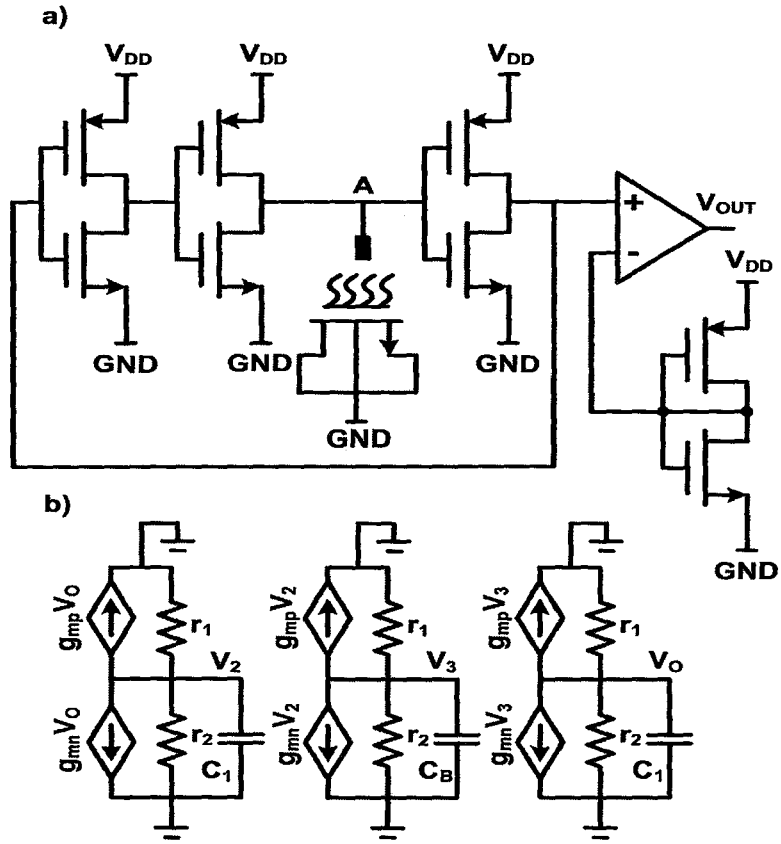

Figure 5.15 a) Ring oscillator based biosensor, and b) Small signal equivalent circuit

The frequency of oscillation is given by ω_0, such that:

$$2\tan^{-1}\left(1+\omega_0 C_1(r_1 // r_2)\right)+\tan^{-1}\left(1+\omega_0 C_b(r_1 // r_2)\right)=\pi . \qquad 5.17$$

Despite the high sensitivity of this circuit, it suffers from high nonlinearity. Figure 5.16 shows a sample plot of the frequency as a function of the capacitance where C_b=10C_1. A quasi-inverse relationship links the two quantities. If the quantity on the left hand side of equation 5.17 is negligible, then the relationship will be a perfect inverse law, which demonstrates high nonlinearity. Thus, it will be important to compensate for this nonlinearity in software.

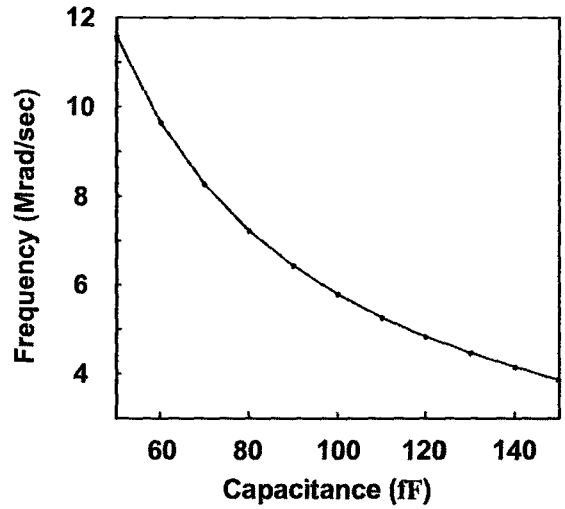

Figure 5.16 Dependence of oscillation frequency on the capacitance of the BioFET

A variation to the circuit of Figure 5.15 is to replace one of the transistors in an inverter stage with a BioFET. The circuit that implements this idea is shown in Figure 5.17. This placement of the BioFET would place an added constraint on the design of the circuit. The quiescent voltage of the ring oscillator now must be around the BioFET's threshold voltage (moderate inversion), such that the maximum capacitive sensitivity is achieved. Now, hybridization will not only change the input capacitance at this stage, but will also affect the channel resistance at the subsequent stage. If the NMOS is replaced by a BioFET, then hybridization will decrease the capacitance, but will increase the resistance of the channel. On the other hand, if the BioFET replaces the PMOS, then hybridization will increase the capacitance but reduce the channel resistance. Therefore, the net effect is that hybridization will speed up one stage, but will slow down the subsequent stage. If these rates are not equal, then a net change in the frequency of oscillation can be sensed.

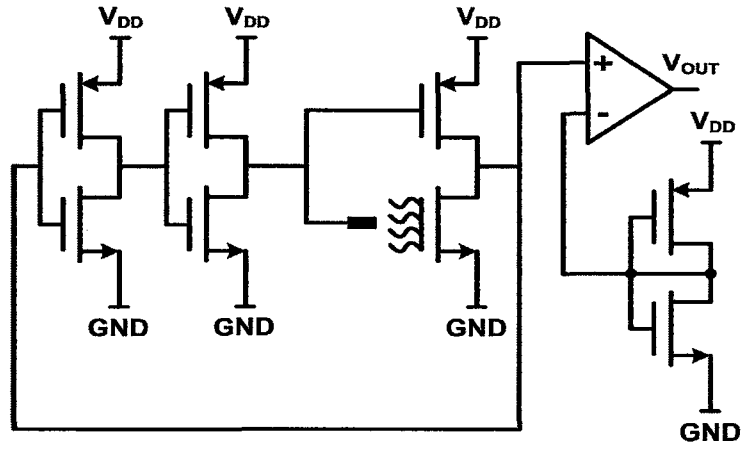

Figure 5.17 Ring oscillator with a BioFET replacing an NMOS

5.2.5 Floating Node Method

A technique that also depends on the capacitance of the BioFET utilizes the charge-sharing of two capacitors at a floating node. This is shown schematically in Figure 5.18. The BioFET is biased from the body with a fixed potential, and a fixed capacitor is connected between the reference electrode and the ground, through a switch. If this capacitance is precharged with a very small voltage V_1 while disconnecting the BioFET, a certain amount of charge will appear across the capacitance. After the precharging process, the capacitor is connected to the BioFET, and the voltage source V_1 is disconnected. This allows the reference electrode to be floating. The initial stored charge in the capacitor will now be shared with the BioFET. The steady-state voltage of the reference electrode will be given by:

$$V_{OUT} = (V_1 + V_B)\frac{C_1}{C_1 + C_B}. \qquad 5.18$$

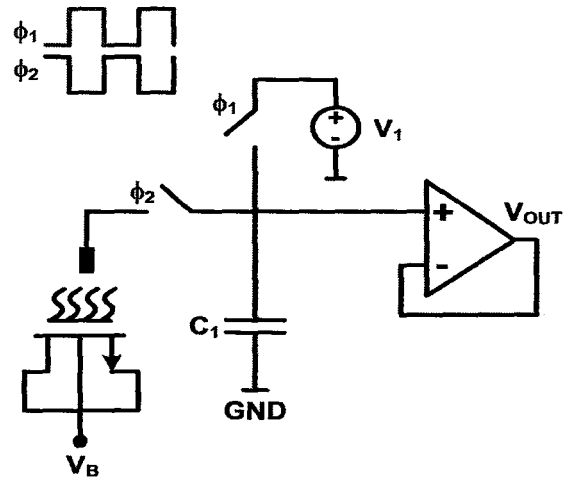

Figure 5.18 Floating node BioFET sensor

This voltage can be sampled using an operational amplifier with extremely low input capacitance. From equation 5.18, it is evident that the response of this circuit will also be nonlinear. In addition, capacitance leakage will cause the floating node voltage to degrade with time. Thus, it would be required to repeat the precharging and sampling process many times to get accurate readings out of this circuit.

5.3 Design of a DNA Microarray Chip in CMOS 0.8μm Technology

In this section, the analysis and design of a microarray chip in standard CMOS 0.8μm technology is presented. At the Institute of Microstructural Sciences, National Research Council (NRC), Ottawa, the quantity, sizing, and geometry of the structures were of prime importance, as this chip would have to be subject to post-processing steps that require adherence to geometry that is compatible with the available equipment. The number of arrays, sizes and spacing of the transistors, and circuits are affected by these requirements.

5.3.1 Fabrication Facility and Technology

The chip was to be designed using DALSA's 0.8μm 3 metal layer, 2 poly CMOS process. Processing of the submitted design was arranged by the Canadian Microelectronics

Corporation (CMC). DALSA's 0.8μm process comes in three flavors: CMOSP8C, CMOSP8E, and CMOSP8G. These three processes are similar, but their main difference is the range of voltages that they support. The CMOSP8C is designed for low-voltage mixed signal applications (3-5V). The CMOSP8E process target medium voltage ranges (5-20V), which include MEMS actuation devices. The CMOSP8G process includes high voltage support (300V), in addition to its normal 5V support. This process is useful for microfluidic device control, and high voltage integrated circuit (HVIC) control and power systems [65].

The DALSA process does not allow twin wells. Therefore, depending on the type of starting material, the body contacts of either the NMOS or PMOS devices would be electrically connected. For the process run that included this design, the starting material was N^- substrate. This would mean that all PMOS devices would share a common body connection. However, in order to verify the operation of the BioFET, and to maintain full controllability over all possible bias voltages, it was necessary to have both NMOS and PMOS devices with separate body connections [63]. As directed by CMC [66], the CMOSP8G process could help accomplish this task. Specifically, certain high voltage definition layers can be used to electrically separate different regions of the N-substrate. Thus, all the PMOS devices which share a body connection could be isolated from the global substrate. The NMOS transistors can be separated by placing each one in a separate P-well. Therefore, the flavor of choice for this design was the CMOSP8G process.

5.3.2 Software Design Kits

All circuit simulations were conducted using Spectre simulation software supplied by Cadence Design Systems, Inc. All layouts were built using Virtuoso custom design platform. The models for the transistors and the design layers were included in the design kit (DK08G) and technology file for the DALSA process, and provided by CMC. The transistor models were based on the BSIMv3.3 architecture. The only components to be simulated were the operational amplifiers. The BioFET transistors were simulated once

with a gate contact to verify normal transistor operation and proper construction, but the gate contact was subsequently removed to facilitate direct exposure of the polysilicon, which would be etched during post-processing.

5.3.3 Architecture

Several different microarrays were required in this project. For each microarray cell, the BioFET transistor was expected to occupy a square area of 50μm×50μm. This size is needed to accommodate the array spotter requirements. The spotter resolution limitations also required that the spacing between the cells be set at 200μm, edge to edge. Such spacing would allow a lot of unused space between the cells that would be sufficient to incorporate any auxiliary circuits. Therefore, all operational amplifiers and differential circuits were placed within these spaces.

Several different microarrays were implemented in the design. Each of these microarrays was required to be electrically isolated from all others. The arrays constructed were the following:

1. A 7×7 array of 50μm×50μm P-type BioFETs, with separate drain connections but shared source and body connections.
2. A 7×7 array of 50μm×50μm N-type BioFETs, with separate drain connections but shared source and body connections.
3. A 7×7 array of 50μm×50μm P-type BioFETs, with separate drain connections but shared source and body connections. Each BioFET is connected in a common-source fashion to a high-impedance active load. The output is read using an operational amplifier configured as a unity gain buffer.
4. A 7×7 array of 50μm×1μm×21 P-type multi-fingered BioFETs, with separate drain connections but shared source and body connections. Each BioFET is connected in a common-source fashion to a high-impedance active load. The output is read using an operational amplifier configured as a unity gain buffer.
5. A 14×7 array, consisting of 7×7 pairs of BioFETs. Each BioFET is connected in common source mode, and the outputs of each pair are passed to differential

amplifiers. The output of the differential amplifier is read by a unity gain buffer. Only one of the two BioFETs will undergo hybridization. This array is designed to reject any signal fluctuations that are common to both BioFET devices, such as temperature and pH variations.

Figure 5.19 shows schematic diagrams of the circuits that were implemented in these arrays. In addition, a large square area of 2.5mm×2.5mm was required for monitoring the etch process during post-processing. This region consists of bare polysilicon deposited on top of the substrate, with the insulator in between. A connection was provided to the periphery of this area to drain away any charges that might leak into the substrate during the etch process. Etch monitoring is important to ensure that the insulator underneath the polysilicon is not damaged during the etching process.

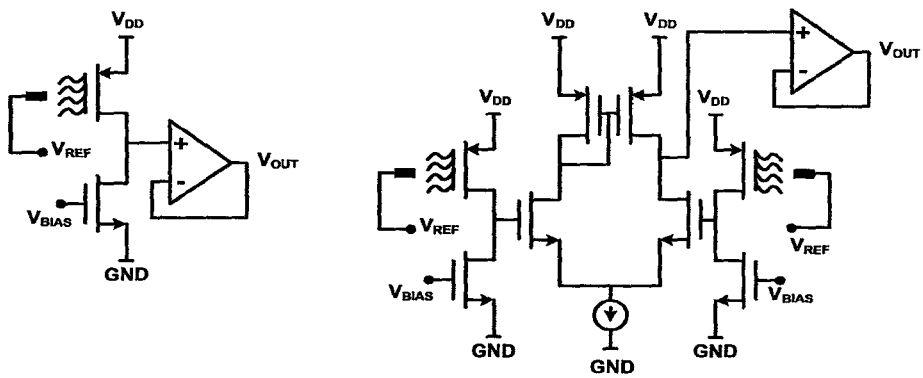

Figure 5.19 Circuits implemented on the microarray chip

The layout of the final chip is given in Figure 5.20. The chip has a size of 10mm×10mm, and is surrounded by 260 pads, in addition to two pads that are placed closer to the center of the chip. These two pads are introduced to serve as reference electrodes when the electrolyte is applied to the surface of the chip. The number of pads was not sufficient for all different arrays and some of them had to be shared by two different arrays. Specifically, the drain connections of each of the BioFETs in arrays 1 and 2 share a single pad.

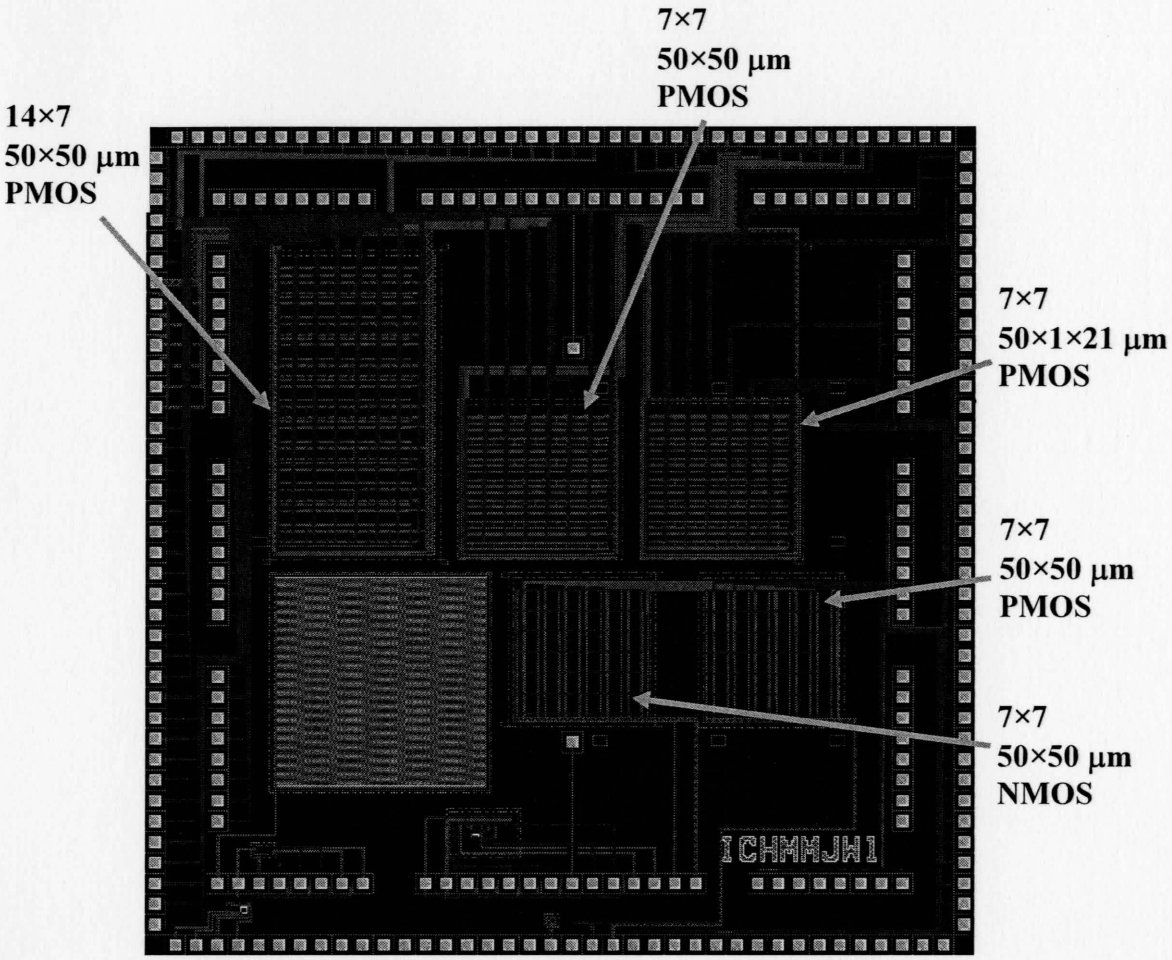

Figure 5.20 Layout of designed microarray chip

To facilitate post processing, several alignment marks were placed on the chip. These consisted of squares of the top metal layer, located in different areas around the chip. These marks provide landmarks that are used for aligning the etch mask with the chip during post-processing. Finally, it is important that there be clearance spacing between the outermost pads and the sliced edge of the chip. A clearance of 0.75mm was required to guard against edge bead formation during the deposition of polydimethylsiloxane (PDMS) onto the chip during post-processing. As this extra space was guaranteed by CMC, there was no need to take this into account when designing the layout.

5.3.4 Operational Amplifier Design

The main circuit component that required proper design in this chip was the operational amplifier. Many different topologies for CMOS operational amplifiers exist [67], [68]. The topology chosen was that of a folded cascode op-amp. This would allow for higher gains to be achieved from a single stage. The body effect in the cascode transistor will enhance the gain performance of the amplifier, contrary to the case of cascaded amplifiers. Finally, compensation capacitors in a cascade transistor need not be as large as that for a regular two stage op-amp. This is because the capacitance can be placed across two stages, which are the output node and the cascode stage, as opposed to one stage in the cascaded two stage amplifier case. The main disadvantage of using this topology is that it allows for some common-mode gain, even with perfectly matched differential transistors and current sources.

Figure 5.21 shows the schematic diagram of the operational amplifier. Transistors M_1 and M_2 form the input differential pair, with M_3 and M_4 as active loads. Transistors M_5 and M_6 form the cascode pair, and a feedback connection to the gates of the active load provide the differential to single-ended conversion. The single ended output is applied to an output common source stage, which provides the final output pin of the amplifier. Using a common source output stage instead of a common-drain mode is justified because the operational amplifier will operate in unity feedback mode. Thus, its output resistance will be roughly divided by the open-loop gain, which will be quite high. The reason for using an amplifying stage at the output is that we want to have a high output dynamic range, which will be limited only by the onset of linear operation of the output transistors. If this last stage were a common-drain stage, then the factor that would determine the dynamic range would be the overdrive voltage of the output transistor, which would be determined by the gate bias. If high dynamic range is required, then the gate bias of the output PMOS would have to be quite high, necessitating a higher gate bias for the cascode transistors to keep them saturated. However, it was desired to have a

cascode bias of zero volts so that we do not need to come up with extra circuitry for bias voltage generation.

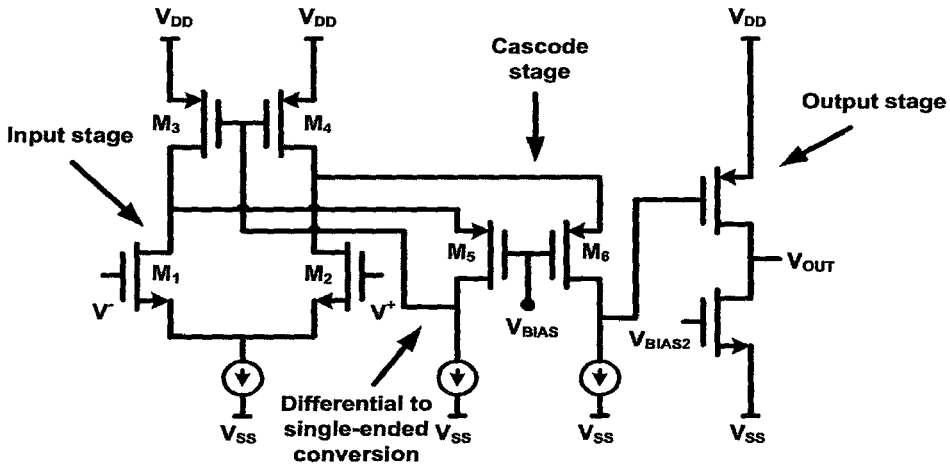

Figure 5.21 Folded cascode operational amplifier

The current driving requirement for the operational amplifier was chosen at 100μA. Given the large number of op-amps in the chip, higher output drive capabilities might heat up the chip and cause undesirable effects to the BioFET sensors. To find the required gate bias voltage of the output PMOS transistor, we use the value of 100μA as the quiescent drain current, and set the output voltage to zero. This will minimize the offset voltage of the op-amp. Recognizing the presence of large-signal variations at the output, the calculated bias was adjusted to keep the output transistor in saturation under the harshest signal swings (chosen here as 1 volt). From hereon, the analysis continues backwards, with the cascode transistors, active loads, and finally the input differential pair. In each step, we impose conditions that guarantee that the device stays saturated, determine appropriate voltage values, and calculate the sizes based on the currents that flow in these branches. The total current consumption in the internal stages of the op-amp was also chosen as 100μA, divided equally among the different conduction paths. Based on these current values and the DC voltages on the nodes that would guarantee saturation, the sizing of the different devices can be deduced [69].

The current sources in Figure 5.21 were implemented using a stacked transistor pair. This would have the effect of increasing the output resistance and would make the

circuit behave more like an ideal current source. The biasing of these transistors was chosen so as to maintain the saturation region of operation. The biasing was kept as low as possible so that the current source has a higher range of operation. This would further enhance the dynamic range of the device.

Figures 5.22a and 5.22b show the simulated frequency response and the voltage transfer characteristics of the designed op-amp, respectively. The dynamic range spans around 4 volts, and the low frequency gain is simulated at 83dB. The bandwidth for the uncompensated op-amp is shown to be around 35kHz. However, to guarantee stability of the op-amp with unity feedback, a Miller compensation capacitor was added at the terminals shown in Figure 5.23. The cascode configuration allows us to place the capacitor over a large inverting gain, consisting of the output stage and the cascode stage. This results in a smaller capacitance value and higher stability. The compensated op-amp has a bandwidth of 8kHz, a gain margin of 7.633dB, and a phase margin of 35°. Figure 5.24 shows a compact layout of the op-amp, in which it is clear that the compensating capacitor occupies a considerable area of the design. Table 5.1 shows the performance parameters of the simulated operational amplifier, compared with typical values of general purpose CMOS op-amps [67-69].

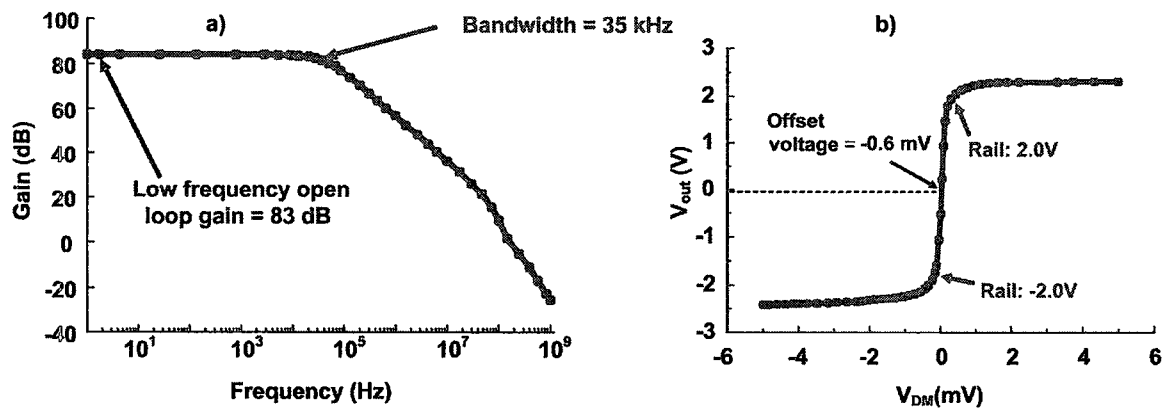

Figure 5.22 a) Frequency response of the operational amplifier, and b) Voltage transfer characteristics

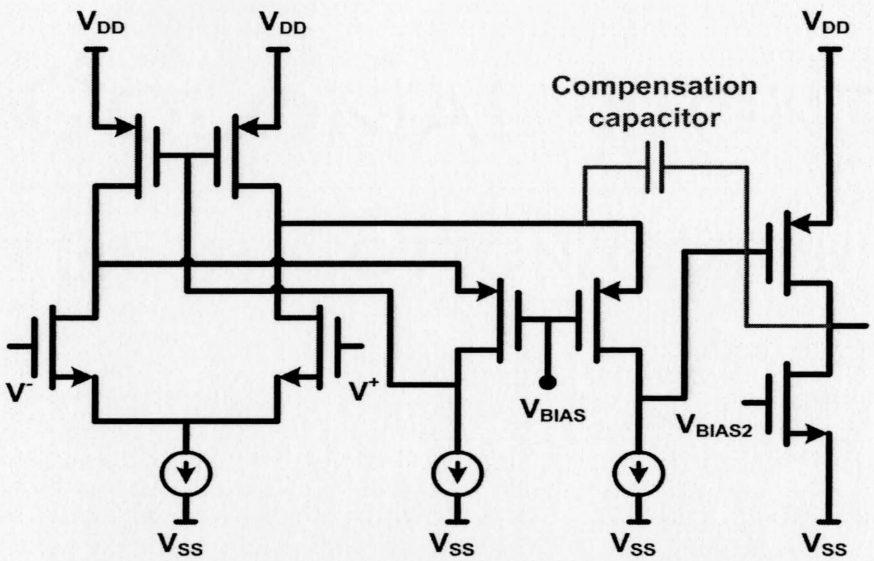

Figure 5.23 Placement of the compensating capacitor

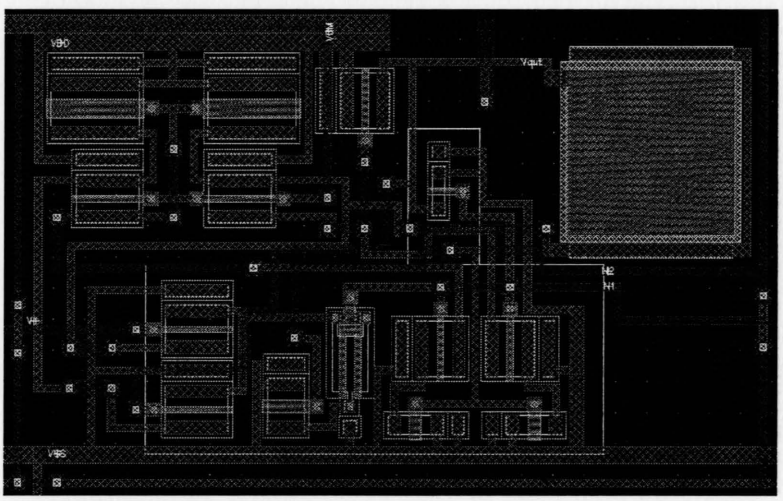

Figure 5.24 Layout of the designed operational amplifier

Table 5.1 Performance parameters of the designed operational amplifier

Parameter	Simulation	Typical
Open-loop gain	83dB	74dB
Common-mode rejection ratio (CMRR)	124dB	80dB
Open-loop bandwidth	35kHz (5kHz with compensation)	100Hz-100kHz
Output resistance	7.8kΩ	300Ω-10kΩ
Slew rate	12.5V/μs (9.5V/μs with 10pF load)	2-20V/μs
Offset voltage	-0.58mV	0.1-1mV
Gain margin	7.63dB	-
Phase margin	35.3°	>60°
Power consumption	1mW	0.5-10mW
Power supply rejection ratio (PSRR)	74dB	80dB

5.4 Conclusion

In this chapter, several circuit designs that can aid in enhancing the sensitivity of the BioFET were discussed. The main design criteria of these circuits are DNA sensitivity, linearity, temperature sensitivity, and power consumption. Different feedback mechanisms were analyzed in order to arrive at circuits that offer better performance. In addition, techniques that exploit the variation in the capacitance of the BioFET were presented. As a general trend, it can be seen that higher sensitivities are generally accompanied by severe nonlinearities.

The design of a DNA microarray chip in CMOS 0.8μm was presented. The chip uses the standard CMOS process, but requires post-processing to make the BioFET structures. Specifically, the polysilicon has to be removed, a hydrophobic coating has to be applied to the processed chip, and probes have to be immobilized on the insulator surface. The BioFET microarray chip illustrates the possibility of fabricating cost-effective biosensors, with all signal processing circuitry integrated on the same chip.

Chapter 6

SUMMARY, CONCLUSIONS, AND FUTURE WORK

6.1 Thesis Summary and Main Contributions

The work presented in this thesis comprises a comprehensive study of the physics involved in sensing DNA hybridization by means of its intrinsic charge using FET devices. Successful characterization of such a device will ultimately lead to highly sensitive DNA microsensors that operate with very low power, and can be incorporated into handheld devices for direct detection of pathogens from environmental samples.
The main accomplishment of this work is combining the physical and chemical modeling of the electrolyte/DNA system with the theory of semiconductors to establish a physical model that relates the change in current due to DNA hybridization to the density of DNA probes [3], [37], [70], [71], [72]. This measure gives quantitative characterization of the sensitivity of the BioFET and can be used to compare BioFET-based sensing to other mainstream methods, such as optical DNA microarrays. The ultimate aim is to be able to use these BioFETs to identify pathogens without the need for DNA amplification.

Another major accomplishment of this work is the global simplification and linearization of the entire physical model of the BioFET [39]. This linearization gives good approximations to the response of the BioFET to DNA hybridization. Moreover, the simplification shows that the response to DNA hybridization can be quantified as a shift in the threshold potential, the amount of which can be given in closed form, as a function of the ionic strength, DNA strand length, DNA probe density, degree of hybridization, adsorption affinity of the insulator surface, and permittivity of the electrolyte and membrane areas. Such a simplified derivation allows the approximate model to be

integrated directly into circuit simulators, as additional components to the already existing MOSFET model. The additions would be compensating voltage sources for the work function differences, as well as for DNA hybridization shifts in the threshold voltage.

This thesis has presented, for the first time, practical guidelines for designing electronic biosensors with emphasis on the noise performance of such systems [39]. Although the noise performance might not be crucial for high density DNA sensing, when working with small geometries, and very sparsely located DNA probes, the signal due to hybridization can be quite weak, and can be easily buried under the random fluctuations of the electrolyte's ionic motion or the random motion of charge carriers in the channel of the FET. This work used the model for the BioFET's sensitivity and the noise theory of MOSFET devices to arrive at an assessment of the SNR performance of such devices. It was seen that the best SNR performance was achieved under low power, low voltage operation mode. This optimum biasing condition lends itself greatly to the design of low-power portable biosensor systems.

The final contribution of this work was to identify and investigate several different circuit techniques that can be utilized to enhance the sensitivity of the BioFET sensor, and which are suitable for implementation in DNA microarrays. The use of feedback systems, both positive and negative, was addressed. Using non-conventional techniques, such as floating nodes and clocked circuits, was presented. The ultimate goal of a circuit interface system to the BioFET is to produce linear, temperature-insensitive, and environment-insensitive, biosensors that are highly sensitive to DNA charges.

6.2 Prospects for Future Work

The model used in this work is simplified so that it is easily understood and translated into understanding of the operation of the sensor. However, the sensitivity of biosensors is only one of many issues that have to be considered when designing state-of-the-art microsystems for DNA detection.

As was presented in this thesis, many different parameters affect the sensitivity of the BioFET. These include, but are not limited to, the electrolyte strength, probe density,

pH of the solution, temperature, bias point and adsorption affinity. The effect of varying each one of these different parameters on the sensitivity was given. However, one can jointly take into account all of these effects, and employ optimization techniques to arrive at an optimum *set* of parameters, which will guarantee the best sensitivity attainable from a BioFET. Of course, a brute force method would be to optimize the sensitivity with respect to a single variable, and then cycle this optimization process to all other variables. One would continue to cycle until an optimum set of variables has been reached. However, this technique can only find a local point of maximum sensitivity, which depends on the initial set of parameters chosen. Other sophisticated numerical techniques for optimization have to be employed to arrive at a global set of parameters that maximize the sensitivity.

The physical model presented in this thesis was based on a 1-D model that treats the DNA charges as a smeared out continuum of negative charges. In reality, however, the charges are highly localized, and this approximation is justified only for highly dense probes. With a 2-D model, the internal structure of the DNA charges will be exposed, and more accurate measures of sensitivity can be attained. The work of [70] attempts to accomplish this task by solving the 2-D electrostatic problem in the electrolyte, while treating the underlying semiconductor as 1-D, so that the FET equations still apply. However, in the real BioFET, the 2-D effects will manifest in the channel, altering its conductivity in a different manner. In order to quantify the response of extremely small BioFETs, with extremely thin concentrations of probe DNA molecules, these effects have to be considered. Generally, analytic solutions will not be attainable to describe the response of the BioFET under these considerations. However, commercial PB solvers and semiconductor modeling software may be integrated to accomplish this task. Otherwise, custom 2-D numerical solver programs can be written that will use numerical techniques, such as the finite difference method, to characterize these devices.

One of the main tasks required to realize fast and sensitive biosensors is that the targets should diffuse towards the probes as fast as possible. With the effects of gravity ignored, the temporal evolution of the diffusion of DNA macromolecules within the bulk

electrolyte is only dependent on the temperature and diffusivity of the particles which, in turn, depend on the solution and molecule properties. Modeling of this diffusion can be accomplished via Fick's laws of diffusion. In the bulk of the electrolyte, no forces will retard the diffusion of the DNA molecules. However, as the DNA molecules get closer to entering the potential barrier of the probe layer (shown in Figure 6.1), a drift force will tend to prevent diffusion of the molecules into the probe region. Thus, higher probe density has two effects: Firstly, it causes more electrostatic repulsion that inhibits proper diffusion of the DNA, and secondly, it reduces the diffusivity of the targets so that even in the absence of electrostatic repulsion, diffusivity of targets towards the probes is limited.

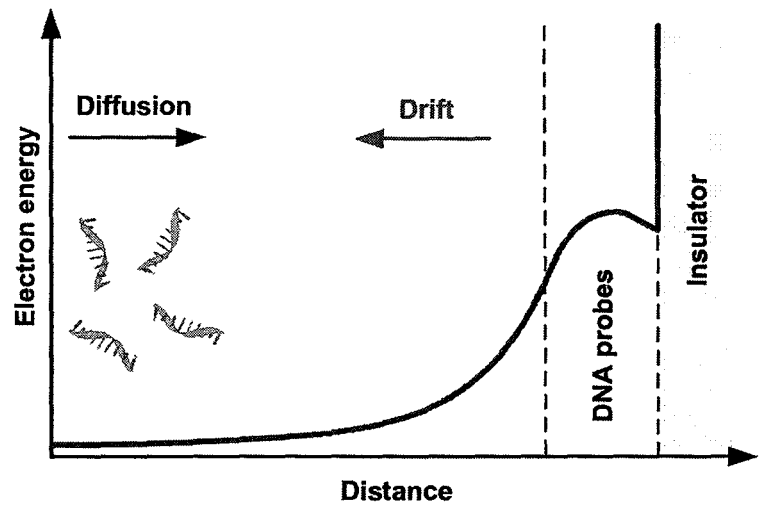

Figure 6.1 Repelling drift force due to probe charges limits the diffusion of targets

In all the work presented in this thesis, it was assumed that full DNA hybridization will be attained in the steady state. However, this is not necessarily true. The actual hybridization yield will be a function of the constants of reaction between the two strands. The constants are governed by a lot of parameters, including the solution ionic concentration, strand lengths (longer strands can take much longer time to fully inter-orient and hybridize), and mobility of targets. Thus, even though particular values can be chosen for the environment such that the sensitivity is maximized, these parameters might cause the hybridization yield to be very low, reducing the sensitivity again. It is, therefore, important to include the kinetics of association-dissociation of DNA molecules into the picture when discussing the performance of BioFETs. Figure 6.2

shows a sample figure for a published work on the dynamic dependence of the hybridization yield on the probe density [71].

A particular model that can be used to characterize the kinetics of operation of the BioFET is the diffusion-reaction model. This model is used extensively to model chemical reactions in confined environments, and in characterization of microfabrication and etching processes [72]. If this model is integrated with the electrostatic model presented in this thesis, then we can arrive at a universal model that would capture the effects of DNA target diffusion, affinity of hybridization and denaturation, and concentration on the speed and sensitivity of the biosensor. A simplified discrete version of this model was previously used to characterize the speed of response in biosensors [73].

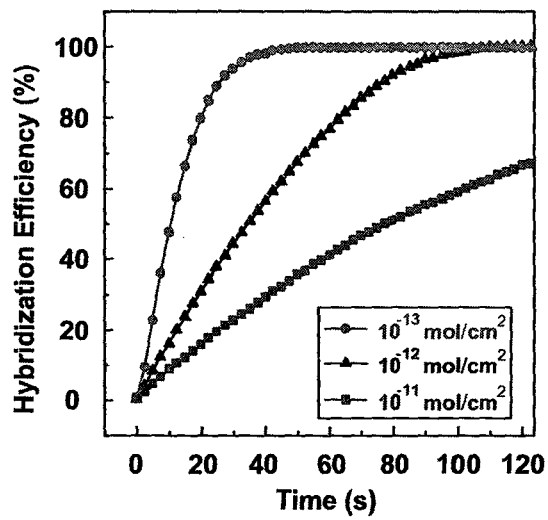

Figure 6.2 Time evolutions of the hybridization efficiency for different probe densities [71]

In terms of measurement setup and methodology, several different techniques can be incorporated. One interesting technique to be investigated is to sense the DNA hybridization by monitoring the change in the device noise characteristics. Low-frequency noise is very sensitive to the amount of current flow and can therefore allow very good sensitivity to be gained from the BioFET. However, it would be quite difficult to integrate such systems into small handheld devices as a lot of circuitry and signal processing systems are required to get the noise spectral density.

In terms of operation, different techniques can be investigated for their effect on the performance of the BioFET. One of these techniques has been identified as continuous pulsing of the BioFET structure. Continuously cycling the FET from accumulation to inversion has been demonstrated to reduce the low-frequency noise of MOSFETs [74]. However, in the case of BioFETs, continuous pulsing may serve yet another purpose. As the DNA targets are electrically charged, they will drift under the influence of the electric field. Thus, pulsing can help these DNA molecules get closer to the probes and can aid in faster hybridization. The procedure of pulsing is shown in Figure 6.3. Thus, using pulsing, we might be able to increase the speed of the biosensor, as well as its signal-to-noise ratio.

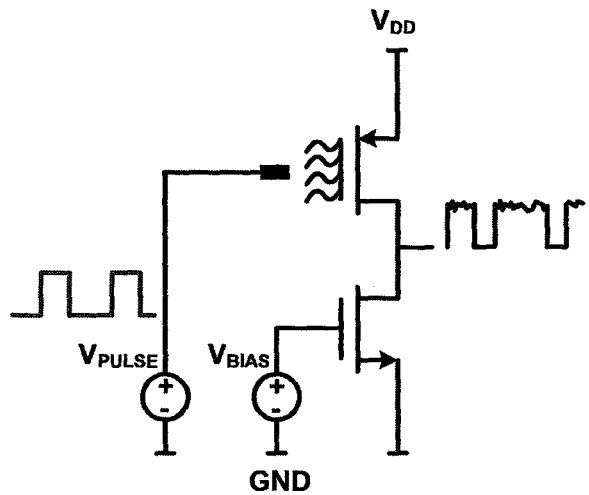

Figure 6.3 Pulsing the BioFET for reduced noise and increased hybridization speed

Modeling the motion of DNA molecules under an applied electric field is quite complicated. This is mainly because the electric field along the electrolyte varies as a function of time. At steady state, the MOS capacitor is fully charged and no current flows. Thus, the electric field in the bulk of the electrolyte will vanish. However, if we somehow maintain the electric field in the bulk electrolyte, the DNA molecules might be able to move under this field and get closer to the probes. The capability of charging the BioFET depends on the ionic conductivity of the solution, as well as the characteristics of the electrode-electrolyte interface. It is clear that very dilute ionic densities will allow a longer manifestation of the electric field within the bulk electrolyte, due to the long time

constants needed for the BioFET to charge. This would allow the DNA molecules to react to the electric field more rapidly. In addition, the counterion screening around the DNA would not be able to fully shield the DNA charge, allowing it to be affected more by the electric field lines.

Modeling of the DNA motion under applied bias is further complicated by the fact that the DNA molecules cannot, in general, be treated as point particles. This means that not all of the energy given to the DNA molecule will manifest as translational kinetic energy that would subsequently lead to electric current in the form of DNA charge migration (electrophoresis). Instead, some of the energy might go into rotational or vibrational motion of the molecule and will not contribute to any current across the BioFET structure. Such complications can sometimes be abstracted away as dependences of DNA mobility on the applied potential. However, this leads to severe nonlinearities and complications in the modeling equations. Much work can be done in modeling DNA motion under applied bias. Such modeling will prove crucial when discussing the effects of pulsing on the speed of hybridization.

The BioFET structure itself might be altered so as to increase the sensitivity, and other novel device geometries might be able to provide much better performance in terms of sensitivity. Two sample devices have been identified here as the junction field-effect transistor (JFET) structure, and the BioFET without the insulator.

In a JFET, the amount of current that flows through the device is modulated by the amount of reverse bias applied to the gate terminals, which causes a depletion region that "chokes" the channel and controls the amount of current flow. A cross section of the JFET is shown schematically in Figure 6.4. The JFET has the advantage that the drain current flows in the bulk of the semiconductor, thereby reducing the low frequency noise contribution of the device. If the DNA molecules were hybridized onto the JFET, the change in the depletion region due to this hybridization will be sensed as a reduction in current flow. However, for this change to be significant, the initial channel of the JFET must be extremely narrow. Current CMOS processes are not suitable for creating

integrated JFET transistors. However, such a device, if realized, can produce higher sensitivity and SNR values.

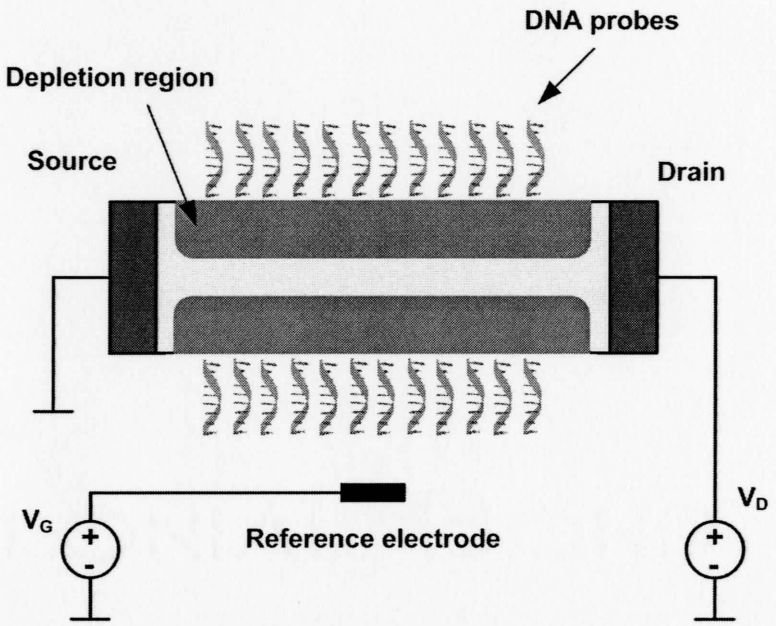

Figure 6.4 JFET based DNA biosensor

A BioFET without an insulating surface can significantly increase the sensitivity of the device. In essence, the structure will be that of an electrolyte/semiconductor interface. Direct coupling has the advantage of a very high capacitance, indicating a large degree of inversion due to hybridization. However, if the electrolyte/semiconductor interface is Faradaic, then a lot of power will be consumed as current will leak between the electrolyte and the semiconductor. This will render such a circuit impractical for portable devices. On the other hand, if the interface is biased such that it acts in an ideally-polarized manner, then we can retain the low power operation capability, while enhancing the sensitivity. In addition, the effects of proton adsorption might be eliminated in the process, since the adsorption sites have been removed along with the dielectric.

On the level of final products, future work can target the integration of CMOS biosensors with state-of-the art MEMS and microfluidic devices on the same chip. This chip can have several subsystems for the acquisition, processing, and detection of pathogens within sample analytes. In essence, micro-reaction chambers can be constructed that will conduct the familiar processes of cell lysing, gel electrophoresis,

PCR, purification, filtration and detection, all in microscale. MEMS-based micropumps can be used to guide the transport of the analyte through these various steps. Microscale-based processing can significantly reduce the time required for the detection process. This can be very useful for early detection of pathogens based on their gene signatures. The ultimate goal of this research would be to arrive at a realization of a complete lab-on-chip device that achieves ultra-high sensitivity, down to the resolutions that will eliminate the need for amplification and analyte enhancement, and has all the microelectronics, readout sensors, digital signal processors, microfluidic components and channels, integrated on the same chip.

References

[1] M. J. Heller, "DNA microarray technology: devices, systems and applications," *Annual Review of Biomedical Engineering*, vol. 4, pp. 129-153, 2002.

[2] E. Neher, "Molecular biology meets microelectronics," *Nature Biotechnology*, vol. 19, p. 114, February 2001.

[3] M. Waleed Shinwari, M. Jamal Deen and D. Landheer, "Study of the electrolyte-insulator-semiconductor field-effect transistor with applications in biosensor design," *Microelectronics Reliability*, In press, 33 pages, October 2006.

[4] M. Gabig and G. Wegrzyn, "An introduction to DNA chips: principles, technology, applications and analysis," *Acta Biochimica Polonica*, vol. 48, no. 3, pp. 615-622, 2001.

[5] R. C. McGlennen, "Miniaturization technologies for molecular diagnostics," *Clinical Chemistry*, vol. 47, no. 3, pp. 393-402, 2001.

[6] S. Smith, *et al.* "Miniaturised drug delivery system with wireless power transfer and communication," *The Institution of Engineering and Technology Seminar on MEMS Sensors and Actuators, 2006*, pp. 155-162, 2006.

[7] C. Korfhage, *et al.* "Critical factors for successful microarray and real-time PCR analyses", *QIAGEN News*, no. 5, pp. 17-21, November 2002.

[8] D. W. Ussery, "DNA denaturation," *The Encyclopedia of Genetics*, vol. 1, pp. 550-553, New York: Academic Press, 2001.

[9] D. M. Wilson, S. Hoyt, J. Janata, K. Booksh and L. Obando, "Chemical sensors for portable, handheld instruments," *IEEE Sensors Journal*, vol. 1, no. 4, pp. 256-274, December 2001.

[10] Y. Long, C. Li, H. Kraatz and J. S. Lee, "AC impedance spectroscopy of native DNA and M-DNA," *Biophysical Journal*, vol. 84, pp. 3218-3225, May 2003.

[11] R. Thewes, *et al.* "Integrated circuits for the biology-to-silicon interface," *Proceedings of the 30th European Solid-State Circuits Conference ESSCIRC 2004*, pp. 19-28, 2004.

[12] R. Bashir, "BioMEMS: state-of-the-art in detection, opportunities and prospects," *Advanced Drug Delivery Review*, vol. 56, no. 11, pp. 1565-1586, 2004.

[13] M. Zhang, C. L. Sabharwal, W. Tao, T. Tarn, N. Xi and G. Li, "Interactive DNA sequence and structure design for DNA nanoapplications," *IEEE Transactions on Nanobioscience*, vol. 3, no. 4, pp. 286-292, 2004.

[14] D. Proudnikov and A. Mirzabekov, "Chemical methods of DNA and RNA fluorescent labeling," *Nucleic Acids Research*, vol. 24, no. 22, pp. 4535-4542, 1996.

[15] F. Betrucci, *et al.* "Sensitivity issues in DNA array-based expression measurements and performance of nylon microarrays for small samples," *Human Molecular Genetics*, vol. 8, no. 9, pp. 1715-1722, 1999.

[16] A. Offenhäusser and W. Knoll, "Cell-transistor hybrid systems and their potential applications," *Trends in Biotechnology*, vol. 19, no. 2, pp. 62-66, February 2001.

[17] A. Bruno Frazier, R. O. Warrington and C. Friedrich, "The miniaturization technologies: past, present, and future," *IEEE Transactions on Industrial Electronics*, vol. 42, no. 5, pp. 423-430, October 1995.

[18] T. Vo-Dinh, *et al.* "Advanced biochip: principle and applications in medical diagnostics and pathogen detection," *Proceedings of the 2003 International Symposium on Circuits and Systems ISCAS'2003*, vol. 3, pp. 622-625, 2003.

[19] D. Ivnitsky, I. Abdel-Hamid, P. Atanasov and E. Wilkins, "Biosensors for detection of pathogenic bacteria," *Biosensors and Bioelectronics*, vol. 14, pp. 599-624, 1999.

[20] B. Swaminathan and P. Feng, "Rapid detection of food-borne pathogenic bacteria," *Annual Review of Microbiology*, vol. 48, pp. 401-426, 1994.

[21] J. Wang, "From DNA biosensors to gene chips," *Nucleic Acids Research*, vol. 28, no. 16, pp. 3011-3016, 2000.

[22] E. M. Southern, "Detection of specific sequences among DNA fragments separated by gel electrophoresis," *Journal of Molecular Biology*, vol. 98, no. 4, pp. 503-517, 1975.

[23] S. Hleli, A. Abdelghani and A. Tlili, "Impedance spectroscopy technique for DNA hybridization," *Sensors*, vol. 3, pp. 472-479, 2003.

[24] W. Cai, J. R. Peck, D. W. van der Weide and R. J. Hamers, "Direct electrical detection of hybridization at DNA-modified silicon surfaces," *Biosensors and Bioelectronics*, vol. 19, pp. 1013-1019, 2004.

[25] Y. Okahata, Y. Matsunobu, K. Ijiro, M. Mukae, A. Murakami and K. Makino, "Hybridization of nucleic acids immobilized on a quartz crystal microbalance," *Journal of American Chemical Society*, vol. 114, pp. 8299-8300, 1992.

[26] E. Souteyrand, *et al.* "Direct detection of the hybridization of synthetic homo-oligomer DNA sequences by field effect," *Journal of Physical Chemistry B*, vol. 101, pp. 2980-2985, 1997.

[27] F. Uslu, S. Ingebrandt, D. Mayer, S. Böcker-Meffert, M. Odenthal and A. Offenhäusser, "Labelfree fully electronic nucleic acid detection system based on a field-effect transistor device," *Biosensors and Bioelectronics*, vol. 19, pp. 1723-1731, 2004.

[28] T. Sakata, M. Kamahori and Y. Miyahara, "DNA analysis chip based on field-effect transistors," *Japanese Journal of Applied Physics*, vol. 44, no. 4B, pp. 2854-2859, 2005.

[29] **www1.imperial.ac.uk/medicine/news/p13121/**

[30] I. N. Levine, *Physical Chemistry.* New York: McGraw-Hill, 1995.

[31] F. Walsh, *A First Course in Electrochemical Engineering.* Alresford: Alresford Press Ltd., 1993.

[32] D. Pletcher, *A First Course in Electrode Processes.* Alresford: Alresford Press Ltd., 1991.

[33] P. Delahay, *Double Layer and Electrode Kinetics.* New York: Interscience Publishers, 1965.

[34] A. K. Vijh, *Electrochemistry of Metals and Semiconductors.* New York: Marcel Dekker, Inc., 1973.

[35] W. Schmickler, *Interfacial Electrochemistry.* New York: Oxford University Press, 1996.

[36] Y. P. Tsivids, *Operation and Modeling of the MOS Transistor.* New York: McGraw-Hill, 1987.

[37] D. Landheer, G. Aers, W. R. McKinnon, M. J. Deen and J. C. Ranuárez, "Model for the field effect from layers of biological macromolecules on the gates of metal-oxide-semiconductor transistors," *Journal of Applied Physics*, vol. 98, no. 4, 044701 (15 pages), August 2005.

[38] D. E. Yates, S. Levine and T. W. Healy, "Site-binding model of the electrical double layer at the oxide-wafer interface," *Journal of the Chemical Society, Faraday Transactions*, vol. 70, pp. 1807-1818, 1974.

[39] M. J. Deen, M. W. Shinwari, J. C. Ranuárez, and D. Landheer, "Noise considerations in field-effect biosensors," *Journal of Applied Physics*, vol. 100, 074703 (8 pages), October 2006.

[40] P. Bergveld, "Development of an ion-sensitive solid-state device for neurophysiological measurements," *IEEE Transactions on Biomedical Engineering*, vol. BME-17, pp. 70-71, 1970.

[41] L. Bousse, "The chemical sensitivity of electrolyte/insulator/semiconductor structures – fundamentals of ISFET operation," Dissertation, Twente University, 1982.

[42] K. Kano, *Semiconductor Devices.* New Jersey: Prentice Hall, 1998.

[43] F. Varsano, E. Masetti, J. F. Guillemoles, F. Decker and D. Cahen, "Ion potential diagrams as guidelines for stability and performance of electrochromic devices," *Ionics*, vol. 3, pp. 420-426, 1997.

[44] K. Rajeshwar, "Fundamentals of semiconductor electrochemistry and photoelectrochemistry," *Encyclopedia of Electrochemistry*, chapter 1, pp. 3-53, Weinheim: Wiley-VCH, 2001.

[45] C. T. Liu, "Circuit requirement and integration challenges of thin gate dielectrics for ultra small MOSFETs," *International Electron Device Meeting IEDM'98 Technical Digest*, pp. 747-750, 1998.

[46] J. C. Ranuárez, M. J. Deen, and C. Chen, "A review of gate tunneling current in MOS devices," *Microelectronics and Reliability*, vol. 46, no. 12, 1939-1956, March 2006.

[47] A. W. Peterson, R. J. Heaton and R. M. Georgiadis, "The effect of surface probe density on DNA hybridization," *Nucleic Acids Research*, vol. 29, no. 24, pp. 5163-5168, 2001.

[48] A. Hassibi, R. Navid, R. W. Dutton and T. H. Lee, "Comprehensive study of noise processes in electrode electrolyte interfaces," *Journal of Applied Physics*, vol. 96, no. 2, pp. 1074-1082, July 2004.

[49] J. Jamnik and J. Maier, "Generalised equivalent circuits for mass and charge transport: chemical capacitance and its implications," *Physical Chemistry Chemical Physics*, vol. 3, pp. 1668-1678, March 2001.

[50] A. Bardos, R. N. Zare, and K. Markides, "Inductive behavior of electrolytes in AC conductance measurements," *Chemical Physics Letters*, no. 402, pp. 274-278, 2004.

[51] Y. Fu, R. Luan, L. Xu, Y. Chai, X. Zhong and D. Tang, "Indicator free DNA hybridization detection via EIS based on self-assembled gold nanoparticles and bilayer two-dimensional 3-mercaptopropyltrimethoxysilane onto a gild substrate," *Biochemical Engineering Journal*, vol. 23, no. 1, pp. 37-44, 2005.

[52] A. Leon-Garcia, *Probability and Random Processes for Electrical Engineering*. New York: Addison-Wesley Publishing Company, 1994.

[53] M. J. Deen, B. Iñiquez, O. Marinov and F. Lime, "Electrical studies of semiconductor-dielectric interfaces," *Journal of Materials Science Materials in Electronics*, vol. 17, no. 9, pp. 663-683, 2006.

[54] M. J. Deen and F. Pascal, "Electrical characterization of semiconductor materials and devices-review," *Journal of Materials Science Materials in Electronics*, vol. 17, no. 8, pp. 549-575, 2006.

[55] L. K. J. Vandamme, X. Li, and D. Rigaud, "1/f noise in MOS devices, mobility or number fluctuations?," *IEEE Transactions on Electron Devices*, vol. 41, no. 11, pp.1936-1945, November 1994.

[56] T. D. Au and K. Khoo, "Improved flicker noise model for submicron MOSFET devices," http://kabuki.eecs.berkeley.edu/~danelle/ee231/ee231.pdf.

[57] M. J. Deen and O. Marinov, "Noise in advanced electronic devices and circuits," *18th Int. Conf. on Noise in Physical Systems and 1/f Fluctuations (ICNF 2005)*, Salamanca, Spain, 19-23 September 2005, AIP Conf. Proceedings, vol. 780, pp. 3-12, 2005.

[58] M. Valenza, A. Hoffmann, D. Sodini, A. Laigle, F. Martinez and D. Rigaud, "Overview of the impact of downscaling technology on 1/f noise in p-MOSFET to 90nm," *IEE Proceedings Circuits, Devices and Systems*, vol. 151, no. 2, pp. 102-110, April 2004.

[59] M. Marin, M.J. Deen, M. de Murcia, P. Llinares, and J.C. Vildeuil, "Effects of body biasing on the new low frequency noise of MOSFETs from a 130 nm CMOS technology," *IEE Proceedings Circuits, Devices and Systems*, vol. 151, no. 2, pp. 95-101, April 2004.

[60] A. Morgenshtein, "Design and methodology of ISFET (ion sensitive field effect transistor) microsystems for bio-telemetry," Master Thesis, The Technion, Israel Institute of Technology, Department of Biomedical Engineering, Haifa, April 2003.

[61] B. Premanode, W.P. Chan, and C. Toumazou, "Ultra-low power precision ISFET readout using global current feedback," *Electronics Letters*, vol. 42, no. 22, October 2006.

[62] B. Palán, F.V. Santos, J.M. Karam, B. Courtois, and M. Husák, "New ISFET sensor interface circuit for biomedical applications," *Sensors and Actuators B*, vol. 57, pp. 63-68, 1999.

[63] Personal Communication with Dr. D. Landheer, Institute for Microstrustural Sciences (IMS), National Research Council (NRC), Ottawa.

[64] A. Morgenshtein, L. Sodakov-Boreysha, U. Dinnar, C. G. Jakobson, and Y. Nemirovsky, "CMOS readout circuitry for ISFET Microsystems," *Sensors and Actuators B*, vol. 97, pp. 122-131, 2004.

[65] *User Guide: Multi-Project Wafer for Prototyping at DALSA Semiconductor*. DALSA Semiconductor, May 2006.

[66] Personal Communication with Mr. H. Ho, Canadian Microelectronics Corporation (CMC), Kingston.

[67] R. Gregorian, *Introduction to CMOS OP-AMPS and Comparators*, John-Wiley and sons, 1999.

[68] R. Gregorian, and G. C. Temes, *Analog MOS Integrated Circuits for Signal Processing*, John-Wiley and sons, 1986.

[69] P. R. Gray and R. G. Meyer, "MOS operational amplifier design: a tutorial overview," *IEEE Journal of Solid-State Circuits*, vol. SC-17, no. 6, pp. 969-982, 1982.

[70] M. J. Deen, M. W. Shinwari, D. Landheer, and G. Lopinski, "High sensitivity detection of biological species via the field-effect," *Proceedings of the IEEE International Caribbean Conference on Devices, Circuits and Systems,* Playa del Carmen, Quintana Roo, Mexico, pp. 381-385 (26-28 April 2006).

[71] D. Landheer, W.R. McKinnon, G. Aers, W. Jiang, M. J. Deen, and M. W. Shinwari, "Calculation of the response of field-effect transistors to charged biological molecules," *IEEE Sensors Journal*, 9 pages, In press (accepted February 2007).

[72] M. J. Deen and M. W. Shinwari, "Modeling the electrical characteristics of FET-type sensors for biomedical applications," *Workshop on Compact Modeling*, Santa Clara, CA, 4 pages (20-24 May 2007).

[73] W.R. McKinnon and D. Landheer, "Sensitivity of a field-effect transistor in detecting DNA hybridization, calculated from the cylindrical Poisson-Boltzmann equation," *Journal of Applied Physics*, vol. 100, 054703, 2006.

[74] D. Erickson, D. Li, and U. J. Krull, "Modeling of DNA hybridization kinetics for spatially resolved biochips," *Analytical Biochemistry*, vol. 317, pp. 186-200, 2003.

[75] Ravi Selvaganapathy, *Lecture Notes for ME752, Advanced Microfabrication and Microfluidics*, McMaster University, spring semester, 2007.

[76] A. Hassibi, T. H. Lee, R. Navid, R. W. Dutton, and S. Zahedi, "Effects of scaling on the SNR and speed of biosensors," *Proceedings of the 26th Annual International Conference of the IEEE EMBS*, vol. 1, pp. 2549-2552, September 1-5, 2004.

[77] I. Bloom and Y. Nemirovsky, "1/f noise reduction of metal-oxide-semiconductor transistors by cycling from inversion to accumulation," *Applied Physics Letters*, vol. 58, no. 15, pp. 1664-1666, 1991.